IMAGING DENTAL ULTRASONIC CAVITATION AND ITS EFFECTS

Nina Vyas

A thesis submitted to the University of Birmingham for the degree of

Doctor of Philosophy

Physical Sciences of Imaging in the Biomedical Sciences

Schools of Dentistry and Computer Science

College of Engineering and Physical Sciences

University of Birmingham

January 2017

ABSTRACT

Current methods of dental biofilm removal are predominantly mechanical and are not effective in removing it from irregular surfaces in the mouth. Cavitation occurs around dental ultrasonic scalers and may be a more efficient and less damaging technique. Previous work has failed to quantify the cavitation bubble dynamics around ultrasonic scalers and its effects. The aim was to develop imaging and analysis protocols to analyse the cavitation and to investigate its ability to disrupt biofilms and deliver sub-micron particles into dentine. High speed imaging was used to characterise cavitation. Its effect on biofilm removal and dentinal tubule occlusion was studied using electron microscopy and x-ray micro computed tomography. We are able to demonstrate that cavitation occurs at the free end of scaler tips and increases with power and vibration amplitude. Biofilm can effectively be removed from dental implant surfaces using this cavitation. It can also be used to transport sub-micron particles further into dentinal tubules. The results show that ultrasonic scalers could be optimised for non-contact use and improved removal of plaque from the teeth. The protocols established in this study can be applied to future studies for quantitative investigation of biofilm growth and removal and analysis of cavitation dynamics.

This thesis is dedicated to my parents,

Mr Manu Vyas and Dr Smita Vyas

ACKNOWLEDGEMENTS

I would like to express my sincere gratitude to all of my supervisors for their help in this PhD. My main supervisor Professor Damien Walmsley has been very supportive and kind and I would like to thank him for his dedicated guidance, inspiration and enthusiasm. It made my PhD study an enjoyable experience. I thank my other supervisors, Dr Rachel Sammons, for her patient help in teaching me microbiology and electron microscopy, and Dr Hamid Dehghani for his excellent support in image analysis.

I am fortunate to have had the opportunity to collaborate with academics from a wide range of departments. I thank Professor Owen Addison for his advice during my project on biofilm removal from implants and Dr David Leppinen, Dr Qianxi Wang and the late Professor John Blake for their assistance in the theoretical aspects of cavitation. I acknowledge Professor Liam Grover and his group for their help with hydrogels and Professor Zoe Pikramenou, Dr Will Palin and Hayley Floyd for their support with the sub-micron particle work. My thanks also go to Dr Emilia Pecheva for helping me when I first started and teaching me how to grow biofilm, and to Dr Michael Sandholzer and Dr Jonathan Robinson for their advice with microCT.

This work would not have been possible without the help of the technical staff in the School of Dentistry. I am much obliged to Gay Smith, Jianguo Liu, Sue Finney, Michelle Holder and the other technicians for all their guidance in the lab.

Heartfelt thanks go to my fellow PhD students who have been very friendly and supportive. Ali, Carla, Cleo, Farha, Firas, Hannah, Helen, Ilaria, Isabel, Naveed, Nurul, Pip, Rachel, Roya, Sean and Siti: it has been a great pleasure to know you and thanks for your company. I would also like to thank everyone in the PSIBS centre for their help.

I wish to acknowledge the financial support I received from the EPSRC as part of the PSIBS Doctoral Training centre, and the loan of the high speed cameras from the EPSRC Engineering Instrument Pool. I thank Professor Michael Hannon, Dr Hamid Dehghani and Dr Josephine Bunch for admitting me to the PSIBS program and enabling me to do a PhD.

Finally I would like to thank my friends and family for their assistance. Whether it was for proofreading my thesis or giving me a kind word of encouragement when I was writing up, it really helped so thank you! I am profoundly grateful to my parents in particular for their infinite loving encouragement and support.

CONTENTS

LIST OF TABLES

LIST OF FIGURES

LIST OF ABBREVIATIONS AND ACRONYMS

CDC: Centre for Disease Control

CLSM: Confocal Laser Scanning Microscopy

EDX: Energy Dispersive X-ray Spectroscopy

FIB SEM: Focussed Ion Bean Scanning Electron Microscopy

HTA: Human Tissue Act

ICC: Intra-class Correlation Coefficient

MicroCT: Micro Computed Tomography

MRM: Magnetic Resonance Microscopy

NP: Nanoparticles

OCT: Optical Coherence Tomography

RO: Reverse Osmosis

ROC: Receiver Operating Characteristics

SMP: Sub-micron Particles

SEM: Scanning Electron Microscopy

SLA: Sand blasted, Large Grit, Acid Etched

SLOT: Scanning Laser Optical Tomography

SLV: Scanning Laser Vibrometry

1. INTRODUCTION

1.1 Summary

Ultrasound is acoustic energy above 20 kHz and is used in Medicine and Dentistry for a range of diagnostic and therapeutic applications (Kremkau, 2001). Low intensity, high frequency ultrasound is used for imaging of tissues (<100 mW /cm^2) (Sensen & Hallgrimsson, 2008). In Medicine, ultrasonography uses ultrasound in the MHz frequency range for diagnostic imaging of body structures (Szabo, 2004). Therapeutic ultrasound uses lower frequencies (1-100 kHz) at much higher intensities (Mitragotri, 2005). The acoustic energy is absorbed by the tissues which it passes through, leading to heating. These elevated temperatures are the reason for the healing effect of ultrasound (Mitragotri, 2005). In a liquid, as the frequency of ultrasound is reduced and the intensity remains high, vapour bubbles are created due to the forces acting on the liquid in a phenomenon known as acoustic cavitation (Brennen, 2013). Cavitation can cause the violent collapse of microbubbles which is powered by the pressure changes from the ultrasound (Lauterborn et al, 2007). If such air bubbles occur in tissues then damage will take place. Such damage is beneficial in certain medical applications of ultrasound and include lithotripsy (kidney stone break-up), thrombolysis and drug delivery (Mitragotri, 2005).

In Dentistry, ultrasound is used at frequencies of 20 to 42 kHz and is generated by either magnetostriction or piezoelectricity which produces vibrations in a steel probe (Walmsley, 1988). These probes are used in instruments such as ultrasonic scalers, endodontic files, and for surgical bone cutting (Walmsley et al, 1992). Ultrasonic scalers are used to clinically remove dental plaque biofilm and mineralized deposits from teeth (Walmsley, 1988). However their vibrating metal tip causes damage to tooth enamel and they are not suitable for removing bacterial biofilm and other contaminated deposits from specialised structures such as dental implants or for cleaning small spaces around the teeth. Whilst the metal tip is not suited for such tasks the cavitation that is generated around the tip can undertake this removal. There is a growing body of literature that recognizes the importance of cavitation generated by ultrasonic scalers and its contribution to the cleaning process. Research has revealed the critical role played by cavitation in surface cleaning for industrial applications, but there is little understanding of how cavitation from ultrasonic scalers could be maximised for use in Dentistry, e.g. for biofilm removal and drug delivery.

The aim of this PhD is to quantify the cavitation around ultrasonic scalers and evaluate its effects using imaging techniques. The first part considers high speed imaging of cavitation clouds and individual bubbles, and how these vary with the design of the scaler tip, its power and proximity to a boundary. The second part deals with quantifying the effect of dental biofilm removal with cavitation, the use of cavitation for delivery of sub-micron particles into teeth to combat dental caries and hypersensitivity, and the use of micro computed tomography to image artificial biofilm removal in 3D. This work will give insights into how cavitation can be optimised for use in Dentistry.

In addition, the imaging and analysis protocols developed will be of use to other researchers in similar fields.

1.2 Dental and Biofilm Background

There are 32 permanent teeth in the human dentition, composed of incisors, canines, (known as anterior teeth) premolars and molars (known as posterior teeth). Their shape is related to their function (biting/tearing/grinding). Each tooth has a crown, which protrudes out of the gum (gingiva), and one or more roots, which are fixed in the alveolar bone. The crown is formed of dentine, surrounded by enamel. The root is composed of dentine and covered by a thin layer of cementum, into which the periodontal ligament binds for attachment of the tooth to the bone. The pulp canal runs through the centre of the tooth, providing a rich blood and nerve supply (Collins & Walsh, 1992). Enamel is formed of approximately 96% inorganic hydroxyapatite crystals, and dentine is formed of approximately 70% calcium hydroxyapatite, with the remainder being water and organic matrix (Powers & Wataha, 2014). Microscopic dentinal tubules run through dentine, radiating out from the inner pulp canal, with a diameter ranging from 0.5-4 µm (Ohl et al, 2010).

Dental implants are used to replace missing teeth and are placed in the bone via a surgical procedure. The dental implant is left in situ and the bone grows up to and around the material. The implant becomes fixed and immobile in the bone and may be used to support crowns, bridges and dentures. The process of the bone growing up to and around the implant is termed osseointegration although no bone ‘integrates’ with the implant. The most common materials used for implants are titanium alloys, either with 0.1-0.4% oxygen (aka commercially pure Ti or cpTi) or with 6% aluminium and 4% vanadium (Powers & Wataha, 2014). Titanium is used because of its

biocompatibility and ability to osseointegrate with the alveolar bone, which provides a non mobile fixture. Osseointegration occurs when the bone grows to within 10 nm of the implant surface, with only extracellular matrix remaining in the gap between the implant and bone (Powers & Wataha, 2014). A range of surface treatments can be applied to the implant to promote osseointegration. These aim to increase the surface area and/or change the surface chemistry. Common treatments include sand blasting, acid etching, plasma spraying and electrospraying. An artificial crown is cemented or screwed onto the implant after the surgical placement has taken place (Powers & Wataha, 2014).

Due to the moist and non-sterile environment of the oral cavity, bacteria can easily form a biofilm called dental plaque on all its surfaces, increasing the chance of dental disease around the tooth or dental implant (Bjarnsholt, 2013; Costerton et al, 1999). Regular biofilm removal is therefore required to prevent the disease from occurring.

1.2.1 Biofilm Definition and Growth Stages

A biofilm is a large mass of bacteria adhered to a surface and embedded inside an extra cellular polymeric matrix. Biofilms can grow on any non-sterile surface with a water supply (Costerton et al, 1978). There are defined stages in the formation of a biofilm, and bacteria first require a conditioning layer on the surface. On teeth, this conditioning layer is called the acquired enamel pellicle, which consists of salivary glycoproteins (Costerton et al, 1978). These provide nutrients and also act as binding sites allowing bacterial adherence. Bacteria from saliva can attach to teeth within 2 hours following cleaning. They firstly attach reversibly via Van der Waals forces, and then irreversibly by binding to receptors in the acquired pellicle (Marsh et al, 2009). The initial early colonisers help other bacterial species with poor adhesive ability to attach, and also alter

the environment (such as pH or oxygen concentration) to allow other species with different requirements to colonise (Marsh et al, 2009). As well as this co-aggregation, the existing bacteria replicate, enabling the biofilm to grow upward and outward. This is similar to the way bacterial colonies grow on an agar plate used for cultivating them in the laboratory.

The biofilm matures after up to 10 days. The different layers of bacteria in a biofilm have an interdependent relationship and a complex structure, where nutrients are passed to bacteria in the deeper layers (Zijnge et al, 2010). Some parts of the top of the biofilm (either individually or in a group) then detach to recolonise another area of the surface, helping the biofilm to spread laterally.

Undisturbed dental biofilm undergoes changes in the bacterial composition. Initially, *Streptococci* (e.g. *S. mutans, S. sanguinis, S. oralis*) are the main colonisers, but after approximately 14 days, the altered environment enables anaerobic rod and filament bacteria to dominate (Marsh et al, 2009). This mature dental biofilm can be found in locations which are difficult to clean via tooth brushing, such as between teeth (interproximally), below the gum line (subgingivally), and on other surface irregularities. This biofilm needs to be removed clinically (Monroe, 2007; Stoodley et al, 2002).

1.2.2 Dental Biofilm Mediated Diseases

Dental biofilm must be removed to prevent periodontal diseases, caries and calculus formation. The bacteria in subgingival biofilm cause periodontal diseases by secreting noxious substances such as waste products, enzymes which can digest epithelial tissue and lipopolysaccharides (LPS). LPS can stimulate the production of cytokines, which

causes inflammatory and immune responses. Inflammatory cells can transmit signals to cause bone destruction (Lang & Lindhe, 2015). Biofilm accumulation can first lead to gingivitis, where the gum (gingiva) is irritated and inflammation occurs. Gingivitis can be reversed if the biofilm is removed. If left untreated, this can progress to periodontitis, where the surrounding tissues are destroyed by the body's immune response (Collins & Walsh, 1992). This will eventually lead to loss of tooth attachment. Similar progression can lead to dental implant failure. Biofilm accumulation around implants can cause similar gingival inflammation known as peri-implant mucositis. If untreated, it progresses to peri-implantitis, where bone resorption causes a loss of osseointegration and subsequent implant failure (Rimondini et al, 1997; Rosen et al, 2013). Therefore the removal of plaque biofilm is essential in the treatment and prevention of periodontal and peri-implant diseases.

Caries is caused by pathogenic bacteria in the biofilm, mainly *S. mutans*. They can rapidly convert sugars into acid which demineralizes the enamel, creating a cavity/lesion (carious lesion) (Fejerskov & Kidd, 2009). Exposed dentinal tubules can be subject to dentinal caries (Love & Jenkinson, 2002). This can occur either through the advancement of enamel caries, from caries of the tooth root, or from attrition and erosion (Fejerskov & Kidd, 2009). Bacteria can penetrate into the dentinal tubules and eventually infect the pulp chamber at the centre of the root, leading to pulp necrosis. In this case endodontic treatment (root canal therapy) is required. Regular mechanical removal of biofilm is almost able to completely prevent caries (Fejerskov & Kidd, 2009).

1.2.3 Biofilm Mineralization

Specific bacteria in the plaque biofilm, mainly filamentous micro-organisms, are able to mineralise to form calculus, which is chemically attached to the tooth or dental implant (Monroe, 2007) (Jin & Yip, 2002). Once mineralisation occurs, tooth brushing cannot remove it (Sammons et al, 2010). The plaque can mineralise into calculus once the saliva becomes supersaturated with respect to calcium phosphate salts, enabling their precipitation (White, 1997). Calculus is composed of different phases of calcium phosphate as well as calcium carbonate. Supragingival (above the gum line) calculus most commonly forms near the salivary ducts, on the lingual surfaces of the mandibular anterior teeth (Collins & Walsh, 1992). It can also form on dental implants and dentures. Subgingival calculus occurs in periodontal pockets, and is not visible during oral examination (Roberts-Harry & Clerehugh, 2000). The rough surface of calculus enables more bacteria to grow on it and this enhances the chance of dental diseases, because the bacteria can stay close to the gingival margin. Pores in the calculus can also hold bacterial antigens which may stimulate bone resorption (Marsh et al, 2009). Calculus also makes good oral hygiene more difficult, leading to increased biofilm accumulation. Therefore it is not directly a cause of disease, but it should be removed to minimise the number of surfaces that bacteria can colonize in the mouth.

1.2.4 Periodontal Therapy

The two main ways to prevent dental disease are through mechanical debridement of biofilm or antimicrobial administration. However, antimicrobials are used sparingly to prevent antibiotic resistance, and because they are less effective in treating biofilms as bacteria in deeper layers are shielded (Marsh et al, 2009). Moreover, studies have found that antimicrobials are only effective at treating periodontal disease if used in

combination with mechanical debridement (Gustumhaugen et al, 2014). Although mechanical removal of dental plaque does not kill the pathogens, the disruption of the structure makes it harder for the bacteria to reform into a biofilm (Marsh et al, 2009).

Clinically, conventional periodontal debridement involves scaling, either manually with different types of instruments such as curettes or mechanically using ultrasonic scalers. Scalers and curettes have different shaped tips depending on their intended use (removal of supra/sub gingival calculus, cementum, biofilm) (Collins & Walsh, 1992). In manual scaling, the tip is scraped along the plaque or calculus to dislodge deposits. Ultrasonic scalers have a similar variety of tip shapes but the tip is vibrated at ultrasonic frequencies (20-42 kHz) so less force is required to remove deposits. The vibrations can be generated either using a magnetostrictive transducer (containing a ferromagnetic material which vibrates when a magnetic field is applied via an electromagnet) or a piezoelectric transducer (containing a piezoelectric material which vibrates when an electric current is applied) (Laird & Walmsley, 1991; Walmsley et al, 1992). Ultrasonic scaler tips have an elliptical motion, and are applied so the maximum displacement occurs parallel to the tooth surface to minimize damage. A stream of cooling water is therefore passed over the tip to disperse heat and prevent frictional damage (Figure 1.1). The cooling water also helps to flush away any dislodged debris and helps the operator to see any areas which have not been cleaned.

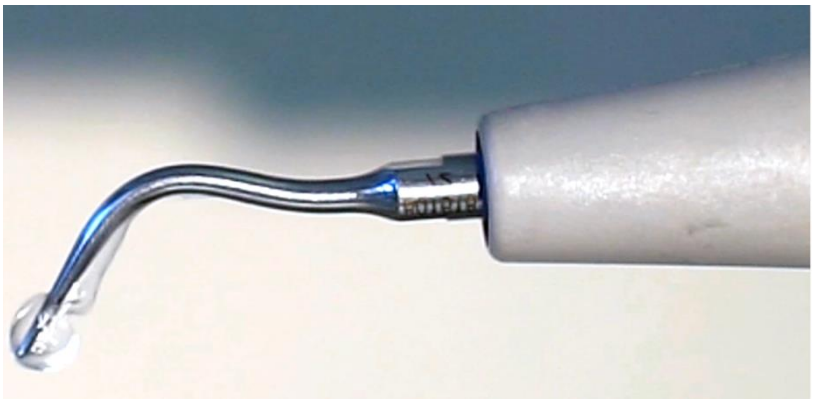

Figure 1.1 Photograph of an ultrasonic scaler in operation with cooling water flowing over the tip. Cavitation and microstreaming occurs in this water flow due to the ultrasonic vibrations.

As well as the mechanical vibrations from the tip of ultrasonic scalers, there are also forces in the cooling water flowing over the tip which could help to disrupt biofilm. Acoustic microstreaming is the oscillation of small fluid elements in the water stream and generates shear forces that could clear soft deposits (Khambay & Walmsley, 1999). Cavitation occurs in the cooling water flowing around the tip, and shock waves and micro jets generated from the cavitation may be aiding in the cleaning (Lea et al, 2005) (see section 1.3). The effects of cavitation from ultrasonic scalers on biofilm removal have not been closely examined (Walmsley et al, 2013).

Although ultrasonic scalers are more efficient than hand instruments at removing large supragingival deposits, they do not provide as much tactile sensitivity. They can also be painful for patients with dentine hypersensitivity or gingival inflammation. On the other hand, manual scaling instruments can be effective at removing smaller deposits remaining after ultrasonic scaling, but they also require more time and subgingival scaling and root planing is not completely effective because of the limited visibility. Both manual and ultrasonic scaling and root planing may expose some dentinal tubules, leading to increased risk of dentinal caries and hypersensitivity (Fejerskov & Kidd, 2009).

There is also currently no effective technique to remove deposits from dental implants. Carbon or plastic curettes and ultrasonic scaler tips are used to clean dental implants to prevent damage to the implant surface, but they are not effective at biofilm removal (Fox et al, 1990; Mann et al, 2012). In particular it is difficult to disrupt biofilm that has colonised the rough part of implants where the surface has been treated to promote osseointegration. If there is bone loss due to peri-implantitis, this part of the implant can become exposed to the oral environment. Biofilm attaches more tenaciously to

these areas because of the increased surface area, and cannot be completely removed with the currently available instruments (Alcoforado et al, 1991; Louropoulou et al, 2014).

Therefore improved methods need to be developed to remove biofilm and calculus more effectively from dental implants, root furcations and periodontal pockets. These methods should also be less painful to the patient and cause minimal damage to the surrounding tissues. More efficient removal of biofilm and calculus will lead to faster treatment of periodontal and peri-implant diseases, and to increased prevention of dental diseases, saving clinicians' time and healthcare costs.

1.2.5 Treatment of Exposed Dentinal Tubules

Dentine is the sensitive part of the tooth. If dentinal tubules become exposed to the oral environment, they can lead to dentinal caries and pain due to dentinal hypersensitivity (Fejerskov & Kidd, 2009) (Figure 1.2). Carious lesions are removed and replaced with dental restorative materials (Powers & Wataha, 2014). One problem during caries treatment is that bacteria which have invaded the dentinal tubules may not be completely removed during the restoration, or can leak through a restoration that is not completely sealed, causing recurrent caries (Fejerskov & Kidd, 2009; Love & Jenkinson, 2002). It is difficult to deliver antimicrobials into dentinal tubules due to their small diameter (0.5-4 μm). Post-operative complications such as dentinal hypersensitivity can also occur due to fluid circulation in the dentine pulp complex. The delivery of antimicrobials and occluding agents into dentinal tubules to treat hypersensitivity and caries is an increasingly important area in dental research (Samiei et al, 2016).

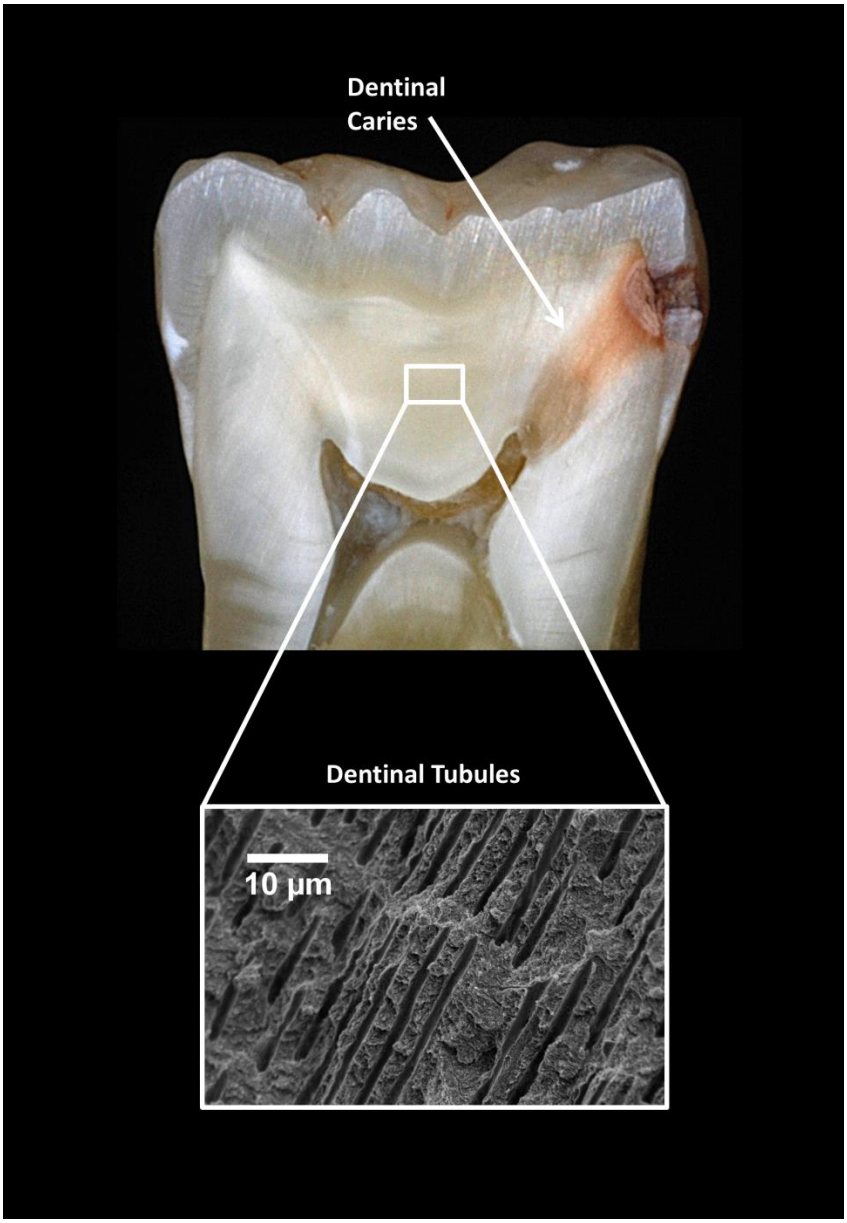

Figure 1.2 Photograph of a tooth with enamel caries leading to dentinal caries. The radial orientation of the tubules can be seen. Photograph courtesy of Mr Louis Mackenzie. Inset: Scanning electron microscopy image of dentinal tubules.

1.3 Cavitation

Cavitation is the generation and collapse of gas or vapour bubbles in a liquid, occurring when the local pressure falls below the saturated vapour pressure (SVP) (Young, 1999). The application of ultrasound can induce cavitation in a liquid. When the pressure falls below the SVP level, during the rarefaction phase of the propagating ultrasound wave, bubbles grow explosively from small pockets of gas (nuclei) present in the liquid (Brennen, 2013). The bubbles grow until the ultrasound wave reaches the compression phase, when the pressure increases. This forces bubble collapse or oscillation, depending on whether the cavitation is transient or stable (Plesset & Prosperetti, 1977). The majority of cavitation bubbles in a liquid are stable, i.e. they oscillate over many cycles. If the cavitation is transient, bubbles grow to many times their original size and rapidly collapse, releasing high amplitude shock waves and high velocity micro jets (Brennen, 2013). Cavitation was initially of interest to researchers due to its adverse effects in the marine technology industry. Cavitation erodes machinery such as propellers, turbines and pumps, reducing their efficiency (Philipp & Lauterborn, 1998). More recently, the usefulness of the phenomenon has been investigated for ultrasonic cleaning in industry and medical applications for drug delivery (Chahine et al, 2016; Chen et al, 2007; Felver et al, 2009; Pishchalnikov et al, 2003; Rivas et al, 2012; Walmsley et al, 2010; Walmsley et al, 2013; Wang & Cheng, 2013). However, the exact mechanisms involved in ultrasonic cleaning have yet to be elucidated (van Wijngaarden, 2016). It is thought that the forces from the micro jet impingement and shock waves are the main contributors (van Wijngaarden, 2016; Verhaagen & Rivas, 2016).

For a given excitation frequency and pressure amplitude, there is a certain radius which needs to be passed in order for cavitation to become transient, known as the ‘cavitation threshold’. Usually stable cavities will turn into transient cavities over time, when they stop oscillating around an equilibrium radius and start to grow via rectified diffusion. It is also possible for smaller bubbles to be transient without first being stable (Young, 1999).

If a cavitation bubble collapses near a boundary, such as a wall or another bubble, it will form a high velocity micro jet which cuts through the centre of the bubble and impacts the opposite surface with large local stresses. Micro jets form in this case because of the asymmetric shape of a bubble near a boundary. When the bubble grows to its maximum size, there is more pressure on the side opposite to the wall, causing that part of the bubble to start to collapse first. The liquid behind the collapsing bubble then accelerates, causing a jet to form(Brennen, 2013). The re-entrant jet penetrates the bubble at a higher velocity than the rest of the collapsing bubble, impacting the opposite surface and forming a high pressure wave. It is believed that the jet imposes a localised high shear force on the surrounding biofilm, lifting it off the surface (Verhaagen & Rivas, 2016). The combined effect of many microbubbles can break up and detach particles from a surface. Blake et al. showed that a bubble must be attached to the surface for the jet to strike in. If this is not the case, the bubble becomes toroidal and moves towards the surface while shrinking (Blake & Gibson, 1987).

Philipp and Lauterborn established the principle mechanism of erosion near a rigid surface (Philipp & Lauterborn, 1998). It was previously thought that the micro-jet produced during the bubble collapse has a significant contribution in erosion. However Philipp and Lauterborn showed this jet only has an effect when the bubble is very near

to or touching the surface. The primary cause of erosion is the formation of a vortex ring bubble. This is a torus shaped bubble which rotates poloidally. The collapse of a vortex ring bubble on a surface produces pressure pulses which are the main cause of erosion on a rigid boundary. They also noted that the most damage from cavitation occurs when a bubble contacts the surface.

Shock waves are another major contributor to surface cleaning and are generated during the collapse of a transient bubble. These waves can fragment the particles/biofilm on the surface to be cleaned(Verhaagen & Rivas, 2016). However they also have the potential to damage the surface being cleaned, so to prevent this, their intensity should be controlled (Verhaagen & Rivas, 2016).

Microstreamers are ribbons of cavitating microbubbles. They are affected by Bjerknes forces and can migrate towards a pressure node or towards a pressure antinode, depending on their size in relation to the bubble resonant radius (Leighton et al, 1990; Wu et al, 2013).

1.3.1 Cavitation Detection Methods

There are various experimental techniques to measure cavitational activity. Many methods detect secondary effects from cavitation, such as through measuring the erosion effects or sonoluminescence. Cavitation causes sonoluminescence, which is a pico-second flash of light emitted from a collapsing bubble or bubble cloud (Suslick & Flannigan, 2008). The high temperatures and pressures generate hydroxyl radicals. The light intensity can be increased with the addition of luminol, which reacts with the OH radicals to create sonochemiluminescence (SCL) (Tuziuti et al, 2002). This light emission can be recorded with a camera to image the areas where cavitation occurs

(Suslick & Flannigan, 2008). The main drawback of this method is that it is low resolution, and as it is an indirect method, the actual cavitating microbubbles cannot be observed. Acoustic methods can also measure cavitation because it causes the first subharmonic of the ultrasonic driving frequency to increase. Examples of these are the hydrophone and the CaviMeter (National Physical Laboratory). However acoustic measurements only give information about the onset of cavitation, they cannot detect the precise location of it (Verhaagen & Rivas, 2016). Optical methods such as high speed photography are more accurate for imaging cavitation because of their high spatial and temporal resolution (Asegehegn et al, 2011; Thoroddsen et al, 2008). High speed imaging enables the detection of the precise location of cavitation areas and individual bubbles. The images can be processed to calculate further details such as bubble growth and collapse velocity, maximum radius and area of bubble clouds. The limitation of high speed imaging is that the data obtained is 2D whereas the bubbles are oscillating in a 3D environment (Verhaagen & Rivas, 2016).

1.3.2 Cavitation around Ultrasonic Scalers

Cavitation around ultrasonic scalers was first confirmed using visualisation with luminol photography (Felver et al, 2009; Lea et al, 2005). Previous studies have shown that SCL occurred around the bend area of ultrasonic scaler tips, but not at the free end of the tip (Felver et al, 2009; Lea et al, 2005; Walmsley et al, 2010; Walmsley et al, 2013). The end is the most clinically relevant part because it comes into contact with the tooth surface the most. SCL has also been combined with scanning laser vibrometry (SLV) to measure the vibration amplitude of ultrasonic scaler tips at the points where cavitation occurs. Felver et al. used this technique to illustrate that vibrations under loaded conditions were damped, and cavitation also decreased under damped

conditions, suggesting that lower vibration amplitude causes less cavitation (2008). They also found that the probe shape is another factor which influences the amount of cavitation occurring, and suggested that modifying the shape of the tip could lead to more cavitation. Terephthalate Dosimetry studies by Price et al. also showed decreased cavitation production when the scaler was placed in contact with a glass slide (2014). Price et al. have hypothesized that a narrower tip shape would create less cavitation at the end of the tip because it displaces less water so it would not be able to create the negative pressures needed for cavitation inception. Therefore it is unclear which aspects of the vibrating tip (shape, vibration amplitude, frequency) influence the cavitation. Previous studies have not imaged the individual cavitation bubbles and clouds which occur around ultrasonic scalers. There is also uncertainty about whether cavitation occurs at the free end of the ultrasonic scaler. The shape and size of the cavitation patterns around ultrasonic scalers have not been closely examined. Although luminol photography has shown cavitation to occur at the bend area of the probe, its precise locations are unknown. One of the main obstacles is the lack of accurate methods to measure the bubbles and determine how they are affected by different factors such as probe shape, power and proximity to a surface. Ultrasonic scalers often operate inside a periodontal pocket which is a confined space. Little is known about how a confined space or a boundary affects the cavitation. High speed imaging could be used for investigating the above challenges as it provides increased resolution and real time, direct imaging of the cavitation. Image analysis of the high speed images can provide quantitative data on how the cavitation is influenced by the different factors.

1.3.3 Biofilm Removal Using Cavitation

The specific mechanisms involved in ultrasonic cleaning of biofilm have not yet been identified. This could be due to the difference in time scales between bubble formation and biofilm disruption; bubble growth and collapse happens over a few microseconds whereas biofilm removal may be occurring over a few milliseconds (Verhaagen & Rivas, 2016). Therefore cleaning could be the combined effect of thousands of cavitating bubbles over many oscillation cycles, making it difficult to image both situations at the same time (Verhaagen & Rivas, 2016). High speed imaging at different frame rates combined with image analysis can be used to investigate both the individual microbubbles and their combined effect. This approach can help to determine which cleaning mechanisms play the biggest part in biofilm removal.

The cell-killing effect of cavitation can be tested via various biological assays. Bacterial cell viability can be tested using live/dead staining combined with fluorescence microscopy. Cell death via sonoporation (rupturing of the cell membrane through cavitation) can be measured using calcein, which indicates the cell membrane permeability (Verhaagen & Rivas, 2016).

Walmsley et al. demonstrated that cavitation from ultrasonic scalers caused removal of tooth root constituents (1990). Price et al. evaluated the effect of cavitation from ultrasonic scalers by using macroscale photography to image removal of ink from glass slides (2014). The area of ink that was removed was correlated with where cavitation occurred. Therefore the cavitation from ultrasonic scalers does have a cleaning effect. There has been no detailed investigation of the impact of this cavitation on biofilm removal from tooth and dental implant surfaces.

Although there is limited data available on the effect of cavitation from ultrasonic scalers, previous studies have investigated the effect of cavitation from other instruments on removing biofilm. For example, the recently developed 'StarStream' instrument uses a jet of cavitating water to clean a range of surfaces. Howlin et al. have used the instrument to disrupt oral biofilms in vitro on tooth models and glass slides with micro scale irregularities (2015). Although the cavitating water jet was able to remove the biofilm, one limitation of the instrument is that it requires a water flow of 2 L/min, making it unfeasible for use in the mouth as it will be uncomfortable for the patient. Therefore the investigators noted that it would be useful to design a smaller instrument which uses the cavitation phenomenon but with smaller quantities of water.

Several studies have investigated the effect of cavitation from endodontic files, known as ultrasonically activated irrigation, for removing biofilm and debris from the root canal. Macedo et al. used high speed imaging to show the effect of cavitation in removing artificial biofilm from root canal models in vitro (2014a). They showed significantly more removal when cavitation occurred. However, further research with more realistic models would be useful, as the artificial biofilm and root canal would have different surface roughness and attachment properties. The irrigant penetration into real biofilm would also be different. Another endodontic instrument known as the 'GentleWave' uses cavitation clouds to disrupt biofilm. Molina et al. used histology of root canals to show that the instrument was more effective than conventional endodontic files at removing debris (2015). However they imaged the slices at x40 magnification, so any micro-scale debris remaining would not have been detected. Another weakness of the study is the method used to calculate the percentage of debris.

Manual segmentation was performed and an average was taken from three examiners. As well as being time consuming, this method is not reproducible.

1.4 Imaging Bubble Dynamics and its Effects

Micron-scale resolution is required to understand the ecosystem of biofilm and its localisation on different surfaces. This can be non-destructively and noninvasively achieved with 3D imaging. Micro computed tomography (microCT) uses x rays to capture projection images through a sample. Up to 2 μm resolution can be obtained. Attempts have been made to image biofilm using benchtop and synchrotron MicroCT systems (Davit et al, 2011). However, very little is known about how biofilm could be imaged for dental research using a benchtop microCT system.

Scanning laser optical tomography (SLOT) is a recent development of optical projection tomography, which is similar to microCT but uses light in the visible spectrum instead of x-rays (Meyer et al, 2013). This technique can measure optical absorption and fluorescence in 3D. SLOT has been used to image biofilm on dental implants with approximately 15 μm resolution and the authors have noted how it could be used as a potential model for testing biofilm formation and removal (Heidrich et al, 2011). However this technique is not as easily accessible to other researchers as microCT.

3D ultrasound has also been used to image biofilm growth on a surface. Shemesh et al. demonstrated this technique with *Streptococcus mutans* biofilm to calculate its thickness (2007). They were able to image biofilm at 10 μm resolution with no staining and calculated its thickness after 7 days. Although the scanning time was quicker than microCT, the thickness calculations obtained were based on assumptions of the speed of ultrasound through a biofilm, and therefore could be inaccurate. In addition, the growth

medium had to be removed and replaced with saline to image with the ultrasound probe, and the biofilm could be damaged during this. The authors also mentioned that this measurement method may not be possible if the surface was a thicker sample such as dentine.

Imaging disrupted biofilm can determine the effectiveness of different treatments. For example, optical coherence tomography (OCT) has been used to assess biofilm damage from hydrogen peroxide (Haisch & Niessner, 2007), and artificial biofilm removal from root canal models has been investigated using high speed imaging (Macedo et al, 2014a). However, higher resolution is required to image individual bacteria remaining on a surface. Electron microscopy has been used qualitatively for this purpose. For example, Lin et al. imaged biofilm in root canals using SEM after root canal procedures (Lin et al, 2013; Wang et al, 2013). They assessed the amount of bacteria in SEM images using intensity based thresholding. Two operators performed the segmentation and the average was taken. However as the grey levels in SEM images are similar between background and biofilm, intensity based thresholding is unlikely to yield accurate segmentation. There is a need to evaluate the accuracy of segmentation procedures for biofilm detection, for example by comparing to a ground truth (Yang et al, 2000).

In terms of imaging and analysis of cavitation, high speed imaging has been used to image the phenomenon around endodontic files. This has been combined with particle imaging velocimetry (PIV) for quantitative information on the flow field (Boutsioukis et al, 2010; Verhaagen et al, 2012). Regarding high speed imaging of cavitation in other research areas, some studies have used image analysis to extract quantitative information such as data on the shape and velocity of individual bubbles during the

growth and collapse phases. Bari et al. have performed 3D reconstructions of bubbles imaged during boiling. This enabled them to approximate the bubble radius of curvature and therefore understand the pressure field around the bubbles (Di Bari & Robinson, 2013). However they assumed the bubbles were axisymmetric when extracting the 3D bubble shape from the 2D high speed images. As cavitation bubbles are not symmetrical when they collapse near a boundary, this approach needs modification to be used in this case.

Many studies used thresholding to segment the bubbles from the background (Busciglio et al, 2008; Duhar & Colin, 2006). As mentioned, such approaches are not reproducible if the imaging conditions are varied. There has been little quantitative analysis of cavitation from high speed images in the area of medical and dental research. Image analysis methods developed for other areas of cavitation research could therefore be applied to this area, in addition to developing new methods which would be of use to other researchers in the field of cavitation imaging.

To summarise, much of the research up to now has been descriptive in nature. Image analysis was performed in some of the above mentioned studies to quantify biofilm area, but often the segmentation was done manually, or with thresholding. These methods are not reproducible and prone to operator error. Therefore there is a need to apply more accurate and reproducible image analysis methods to gain more information about biofilm disruption and cavitation dynamics. Nanoscale resolution, 3D visualisation and real time imaging are three key aspects of imaging modalities needed to study cavitation and its effects. Therefore in this study we used SEM, microCT and high speed imaging.

1.4.1 MicroCT

MicroCT is small scale x-ray imaging in 3D. X-rays between 20 kV- 100 kV pass through the specimen on a rotating stage and onto a high resolution detector (Stock, 2008). The specimen is rotated incrementally and a projection image is acquired after each rotation step. The projection data are then used for image reconstruction (Sensen & Hallgrimsson, 2008). X-rays are attenuated as they pass through the specimen, either through Compton scattering at high energy levels or the photoelectric effect at low energy levels. Materials with different atomic numbers will attenuate the x-rays to different levels, giving rise to contrast in the image (Stock, 2008). Contrast agents containing iodine or barium compounds can be added to materials which have a low attenuation coefficient.

1.4.2 High Speed Imaging

A high speed camera can capture in excess of 250 frames per second (fps). Attachment of a zoom lens can give micrometre resolution. Information can be obtained about the position, size and velocity of cavitation bubbles at any point in time.

There are different types of high speed imaging systems. For frame rates below 1 million fps, they consist of a single CCD/CMOS sensor (Versluis, 2013). Their resolution decreases as the frame rate increases because the number of output terminals on the high speed image sensors cannot be greater than 128. Therefore the data being transferred has to be reduced in resolution if the frame rate is higher. For frame rates above 1 million fps, image converter and rotary prism cameras are available, which rapidly shift between imaging sensors and positions where images are formed (Kondo et al). Other systems are also being developed, such as those with more CCD sensors, back-side illuminated CCD sensors or stacked image sensors (Versluis, 2013).

The limitations of high speed imaging are that it is not practical when the phenomena under observation are not localised in time, or not repetitive.

1.4.3 Scanning Electron Microscopy

Scanning electron microscopy offers high resolution and greater depth of focus compared to optical microscopy. A finely converged electron beam irradiates and scans the sample surface (Stadtländer, 2007). The sample is coated with a conducting film (e.g. gold) to stop surface charging and to increase the signal to noise ratio. The two main detectors for SEM imaging detect secondary electrons (SE) or back scattered electrons (BSE). BSE are incident electrons which have been elastically scattered from the nucleus of a sample atom, and therefore have high energy. Atoms with a higher atomic number will backscatter the electrons more, resulting in brighter parts in the image (Hayat, 1974). For SE mode, the incident electrons interact with atoms in the specimen, causing them to emit SE. These have a low energy, hence only secondary electrons from the top few nanometres of the sample can be detected. Hence topographic information from the sample surface can be obtained at very high resolution. Scanning the beam at a slower rate across the sample acquires more data, giving a higher signal to noise ratio (Kirk et al, 2009). Energy dispersive x-ray spectroscopy can be used for elemental analysis by detecting x-rays emitted from the sample (Stadtländer, 2007).

1.5 Research Aims

To summarise, there is a need for improved periodontal cleaning methods to prevent damage to teeth and dental implants and to improve efficiency of biofilm removal. Cavitation bubbles and acoustic microstreaming occurring around ultrasonic scalers have the potential to be used as a method of ‘non-touch’ cleaning. Current methods of

analysing cavitation around ultrasonic scalers suffer from limited resolution, and therefore it is difficult to identify which factors can optimise the cavitation. In addition, methods used to quantify biofilm disruption suffer from non-reproducible and inaccurate thresholding. Therefore this thesis addresses the dynamics of cavitation around ultrasonic scalers and its interaction with different types of biofilm and sub-micron particles, whilst also developing methods which can be applied in related studies. This will help both clinicians and manufacturers to optimise the instruments. The specific research questions are given in Figure 1.3.

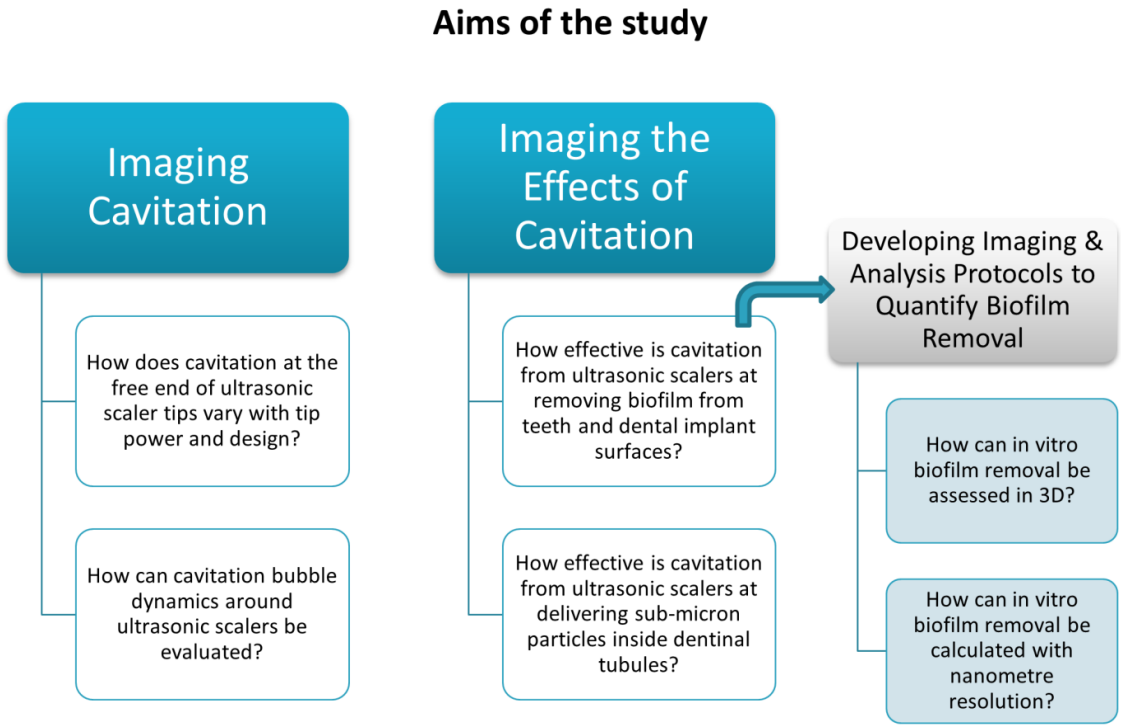

Figure 1.3 Schematic outlining the research questions to be answered in the study.

High speed imaging and image analysis will be used to image the cavitation around ultrasonic scalers. This will firstly be done for cloud cavitation to see how it is affected by different tip designs and powers, and then for individual cavitation bubbles to understand more about the bubble dynamics. This will give information on the exact locations of the cavitation around ultrasonic scaler tips, which can then be used to position the ultrasonic scaler in the following experiments for determining the effects of the cavitation. MicroCT will be used to assess 3D artificial biofilm removal from a tooth and SEM will be done to study biofilm removal from dental implant surfaces and sub-micron particle penetration into dentinal tubules.

2. CAVITATION CLOUDS AROUND ULTRASONIC SCALERS

2.1 Introduction

Cavitation occurs as separate individual bubbles or as clouds of densely packed bubbles. These clouds exhibit enhanced effects of erosion/surface cleaning due to the larger number of bubbles collapsing simultansously (Brennen et al, 1997). Their destructive effect on blades and propellers has been investigated experimentally and computationally and it has been shown that cavitating bubble clouds produce very large pressure pulses (Gnanaskandan & Mahesh, 2016; Reisman et al, 1998). However few studies have investigated the contribution of cloud cavitation to ultrasonic cleaning.

High speed imaging has been used to successfully characterize cavitation activities in fields such as mechanical and biomedical engineering and in dentistry for endodontics (Chen et al, 2007; Duhar & Colin, 2006; Jiang et al, 2010; Macedo et al; Maurus et al, 2004; Peeters et al, 2015). It can be used to image the cavitation directly and in real time, as opposed to the indirect observations obtained from SCL measurements. In addition, the resolution is higher than SCL, allowing image analysis to be done on individual bubbles and clusters and allowing more detailed observation of the cavitation

activity at the free end of the tip. Scanning laser vibrometry (SLV) has been used to make non-contact measurements of the oscillations of ultrasonic scaler tips (Felver et al, 2008; Mann et al, 2012; Walmsley et al, 2013). The cavitation patterns around ultrasonic scalers have not been studied in detail using high speed imaging and image processing. Previous work has only been able to show cavitation occurring at the bend of ultrasonic scaler tips rather than at the free end which contacts the tooth/implant surfaces during cleaning (Felver et al, 2009; Price et al, 2014). The tip shape and its vibration amplitude are thought to affect the amount of cavitation but it is not known how. Combining data from high speed observations and SLV will allow us to understand the link between scaler vibrations and occurrence of cavitation at the most clinically relevant part of ultrasonic scalers.

The aims of this study are to use high speed imaging, SLV and image analysis to investigate how cavitation at the free end of the tip varies with power and tip design, and to observe and provide quantitative data on cavitation clouds and other sono-physical phenomena occurring around ultrasonic scaler tips.

2.2 Materials and Methods

2.2.1 High Speed Imaging

An ultrasonic scaler (Satelec P5 Newtron, Acteon, France) was used for all experiments in conjunction with Satelec tips 10P, 1 and 2 (Figure 2.1). High speed camera imaging was done with the scaler operating at Power 10 (medium) or Power 20 (maximum). It should be noted that the power control dial of the ultrasonic scaler is not a reproducible measure of power and in order to reproduce these experiments the reader is referred to the Appendices chapter where the displacement amplitudes of the ultrasonic scaler tips are given at the different power settings. The power output of the ultrasonic scaler

cannot be measured accurately due to the tip shape, however Walmsley et al. have shown that the displacement amplitude of the tip is that main factor which has to be controlled (Walmsley et al, 1986; Williams & Walmsley, 1988).

The flow rate of the cooling water flowing out of the scaler tip at the lowest flow setting is 0.11±0.01 ml/s. As it was difficult to image clearly with the water flow from the scaler, the tips were submerged in water with the cooling flow turned off. A watertight container with transparent, flat sides was made for high speed imaging by attaching the sides of a 40 mm diameter petri dish, and cutting an opening at the top for inserting the ultrasonic scaler tip (Figure 2.2). Tips were submerged in 10 ml reverse osmosis (RO) water at 20.5 ^{0}C for imaging. The scaler tip under observation was clamped into place within the container, ensuring that no parts of the scaler body were touching the container.

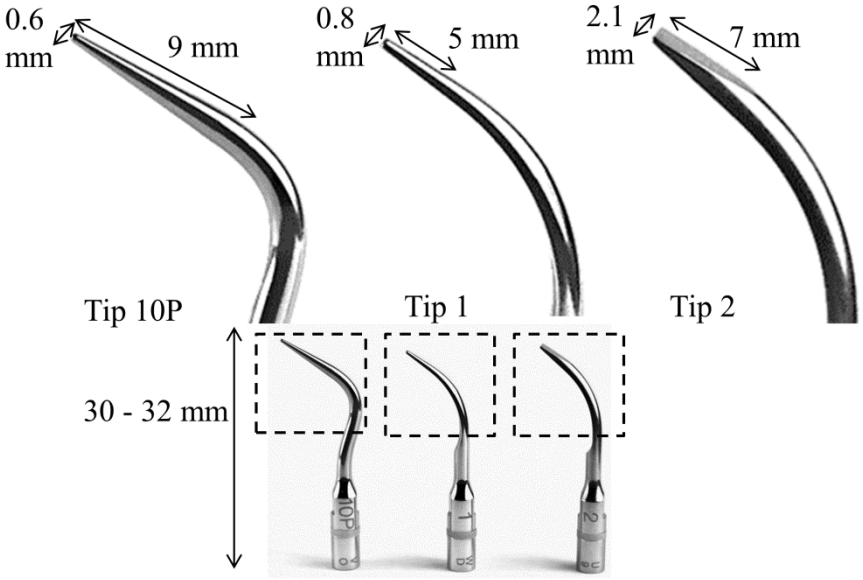

Figure 2.1 The three Satelec ultrasonic scaler tip designs imaged in this study. Tip 10P is the most pointed, tip 1 is pointed but tapers out towards the bend and tip 2 is flat with a wide cross-section.

Imaging was undertaken with a monochrome Photron Fastcam SA.1.1 (Photron, San Diego, CA, USA) attached to a zoom lens (Monozoom 7, Leica Microsystems UK Ltd) (Appendix Table 1). The size of each pixel was calculated from measurements of a 2 mm graticule with 10 µm markings. The scaler was illuminated for high speed imaging with a cold light source (KL 1500, Schott, Stafford, UK) placed either directly above the opening of the container or behind the container for imaging in bright field mode (Figure 2.2). The scaler was positioned using a flexible clamp (Ultra Flex Support, Cole-Parmer Instrument Company, IL, USA).

Tip 10P and tip 2 were modified and imaged using a high speed camera to further visualise the effect of tip shape on cavitation production (Figure 2.4). The outer edge of the free end of each tip was ground and polished manually (DAP-7, Struers, Ballerup, Denmark) using P500 and P4000 SiC paper until horizontal. These alterations were made to increase the pressure drag, which would create lower pressures and consequently increase the cavitation. They were imaged using an ultra high speed camera (HPV1, Shimadzu Corporation, Japan) at 1,000,000 fps. The camera was attached to a zoom lens (Monozoom 7, Leica Microsystems UK Ltd) (Table 1). Illumination was provided by two strobe lights which were synchronised with the camera using a flash light controller, delay generator and trigger switch. The scaler was positioned using a translation stage (PT3, Thorlabs, USA). The scaler tip was imaged in a custom-made glass imaging container with a total volume of 10 ml (Figure 2.3). The container was made by cutting glass microscope slides to 2.7 x 2.7 cm and attaching 5 squares to each other using glass adhesive (Loctite, USA) to create an open cube. The scaler tip was submerged in the container in 10 ml RO water at at 20.5°C.

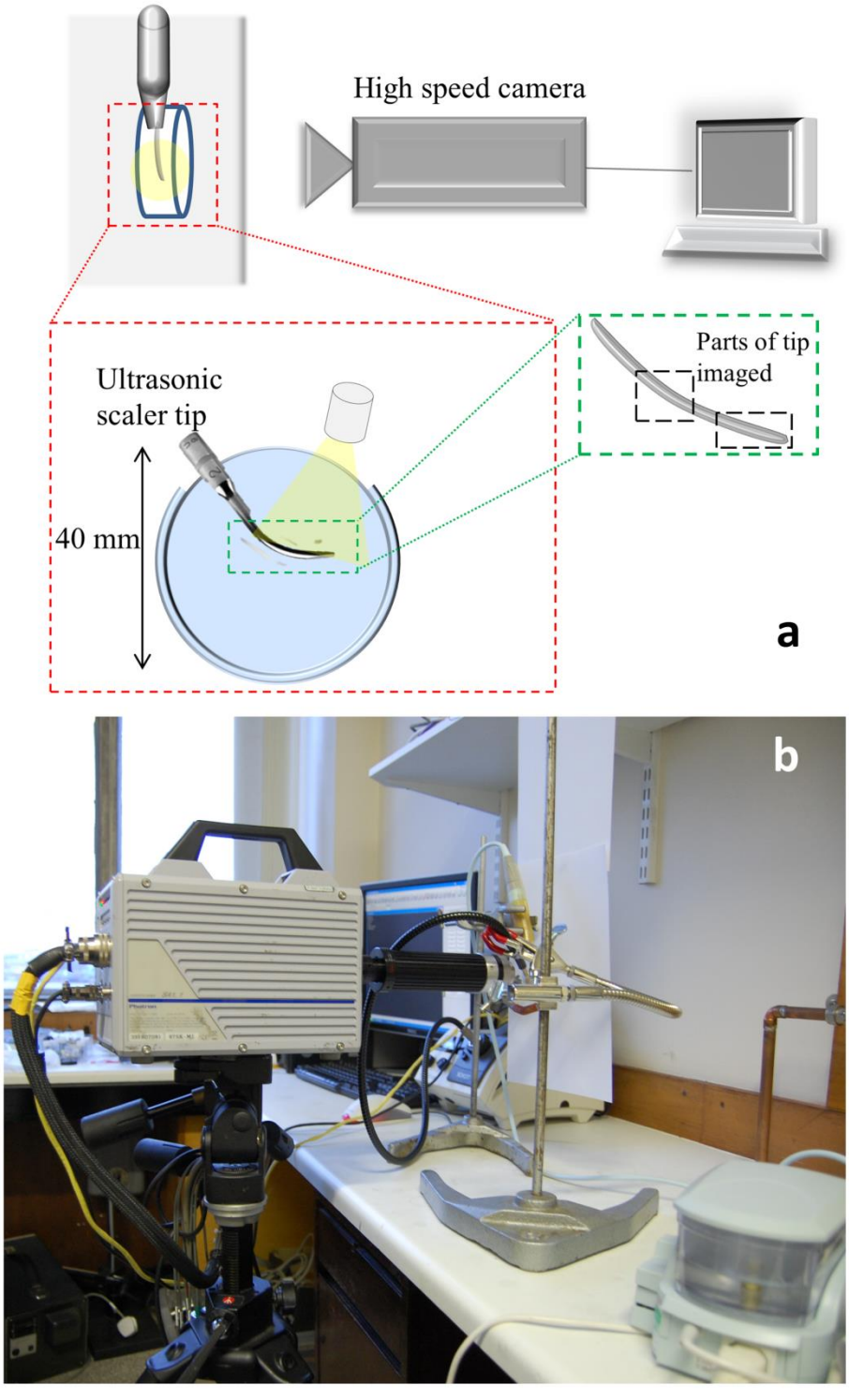

Figure 2.2 (a) Schematic of the experimental setup for high speed imaging showing the petri dish used for imaging and a view of the setup from above. (b)

Photograph of the experimental arrangement with the Photron SA1.1 camera.

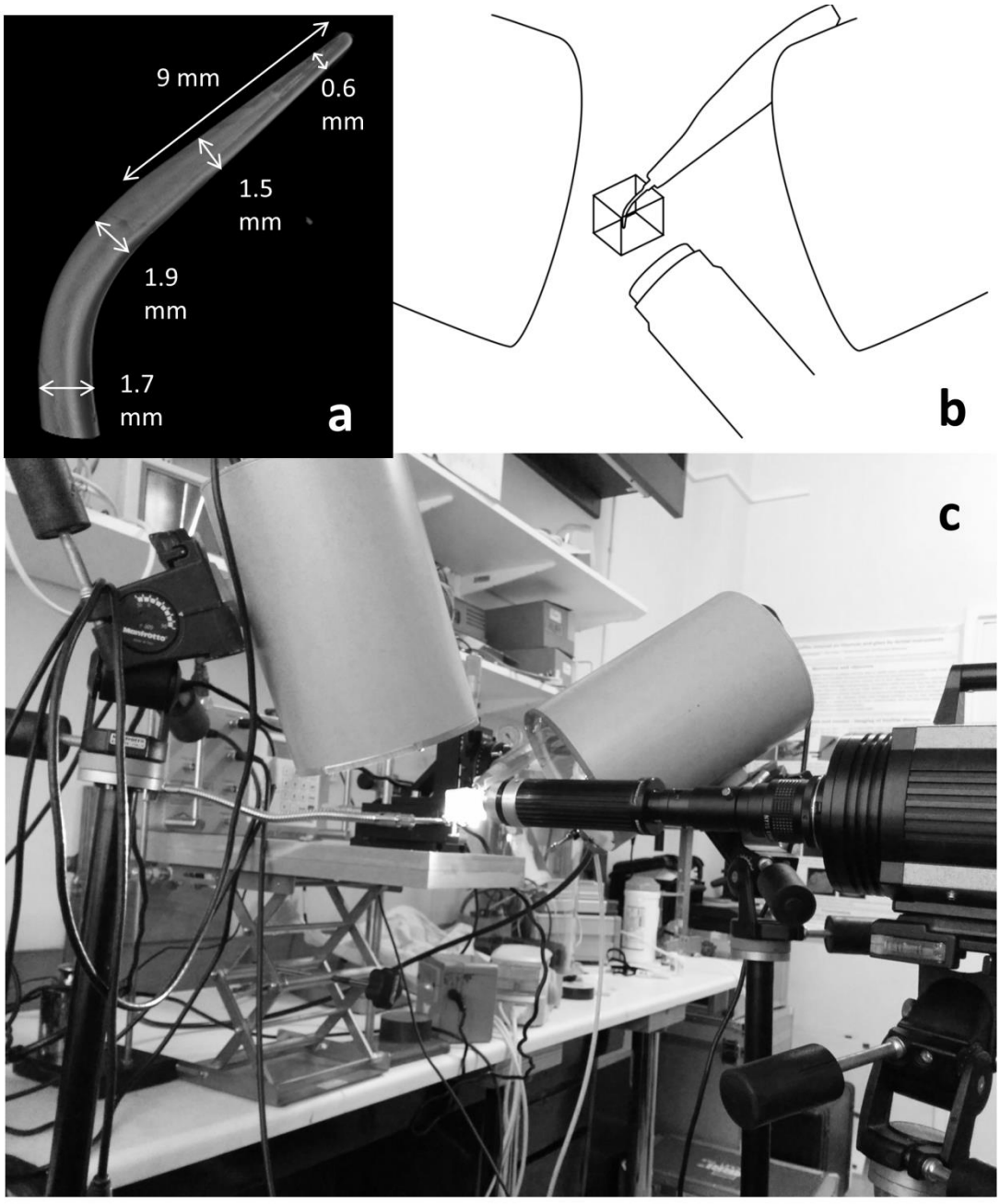

Figure 2.3 (a) Micro computed tomography 3D reconstruction of Tip 10P with dimensions (b) schematic of the experimental setup showing the ultrasonic scaler tip in its imaging container with the zoom lens and strobe lights (c) photograph of the experimental setup

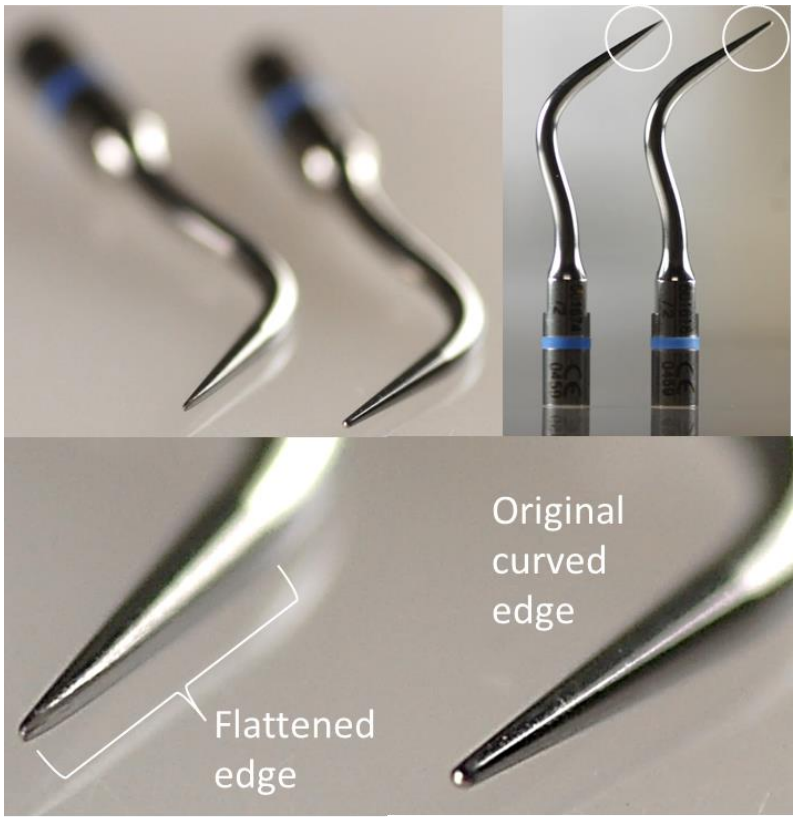

Figure 2.4 Photographs of the modified version of tip 10P alongside the original. The same method was used to modify tip 2.

2.2.2 Image Analysis

Image segmentation was done using a semi-automatic approach via the trainable Weka Segmentation Plugin in Fiji (ImageJ, U. S. National Institutes of Health, Bethesda, Maryland, USA) (Kaynig et al, 2010; Schindelin et al, 2012). Details of the segmentation process used by the plugin are given in Section 5.2.5.4. SigmaPlot 12.3 (Systat Software Inc, San Jose, CA, USA) was used for analysis and graphing of the data. The Mann-Whitney U test was used for testing for statistical significance. Analysis was done using three video repeats for each measurement, with each video containing 940 images (totalling 2820 images per setting). The following steps were performed to segment and measure bubble clouds in the image sequences:

1. Each image was cropped to the same size (4 mm x 1.5 mm) to keep only the bubble cloud at the inner end of the tip (Figure 2.5a). The trainable Weka segmentation plugin in Fiji was used to segment a whole image stack of 940 images. 200 images from each stack were used to create and train a classifier by manually choosing and classifying areas as background or as part of the bubble cloud on 3-4 of the images. The classifier was then applied to the whole stack to automatically segment the images. The plugin uses a Fast Random Forest classifier.

2. Objects smaller than 20 pixels were removed from the binary segmented images, to only keep bubbles that were part of (or had emerged from) the main bubble cloud.

3. The area of each segmented bubble cloud was measured in Fiji using the Analyze Particles plugin. The width and the height of the cloud were measured by extracting the bubble coordinates (Figure 2.5c). The largest x-coordinate was subtracted from the smallest to give the width of the cloud and vice versa in the y direction to give the height. This data was plotted in box and whisker plots.

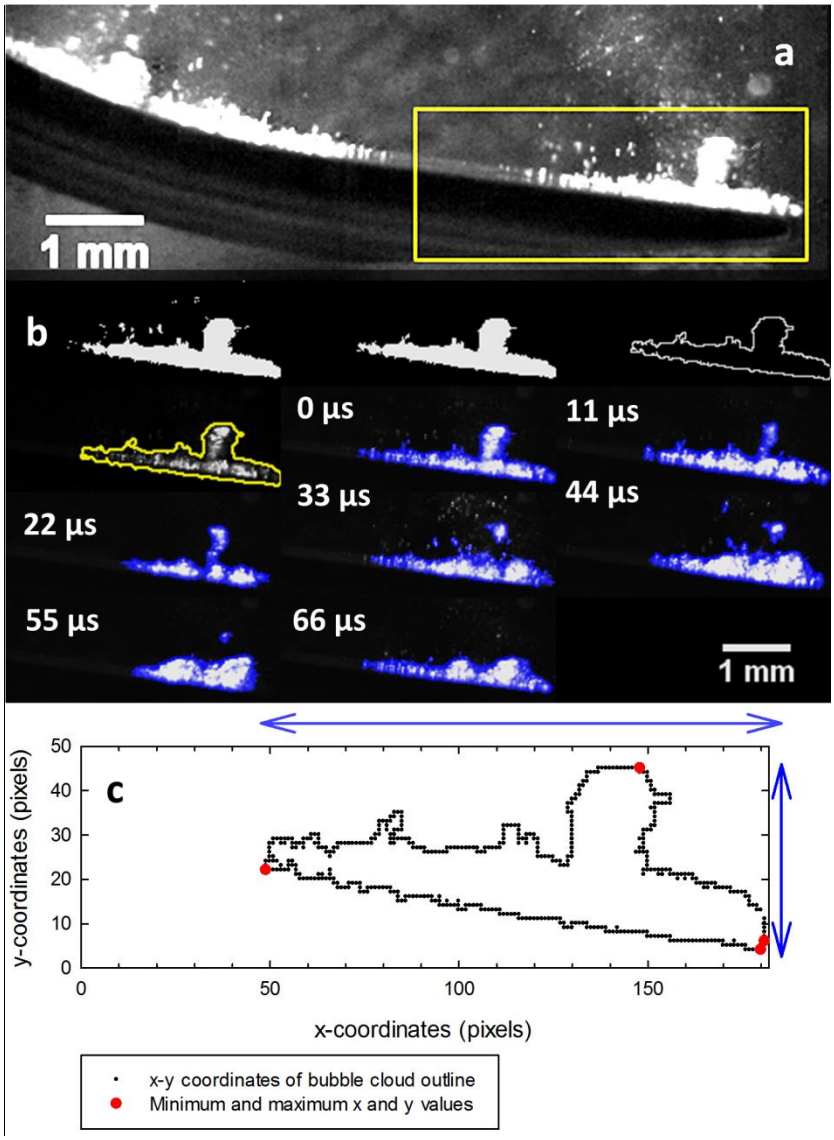

Figure 2.5 Segmentation and quantification process (illustrated with a frame from a video of tip 2 at power 20). (a) Raw image showing the region of interest selected for image analysis. The contrast has been increased for improved visualisation. (b) left to right: Thresholded segmented image of bubble cloud; image after removing any objects smaller than 20 pixels; binary outline of the segmented image; overlay of the segmented outline on top of the original bubble cloud to show the bubble cloud has been segmented accurately; sequential images showing the smaller bubble cloud lifting away from the main cloud. (Overlay of the original images and the thresholded images in blue) (c) graph illustrating how the width and the height of the bubble cloud was calculated from the minimum and maximum x and y coordinates.

2.2.3 Scanning Laser Vibrometry

SLV measurements were performed by Dr Emilia Pecheva. A high frequency scanning vibrometer system (PSV 300-F/S, Polytech GmbH, Waldbronn, Germany) was used in conjunction with an He–Ne laser (λ=632.8 nm, class 2). Measurements were taken at different locations on the tip as described in Pecheva et al. (2016)

2.3 Results

Cavitation around the outer bend of tip 1 was imaged at 15,000 fps (Figure 2.6). Smaller bubble clusters can be seen migrating towards a larger bubble cluster in the centre. Manual tracking follows two of these clusters (labelled 1 and 2) approaching from opposite sides until they meet at the larger bubble cluster at the centre. This also occurred at the bend of tip 2 and tip 10P. The ultrasonic scaler completed nearly 6 oscillations between the frames shown in the figure.

Although individual bubbles were observed, the majority of the cavitation was in the form of bubble clouds. Entire bubble clouds at the tip were imaged on the three tips at 90,000 fps (Figure 2.5). Bubble lift-off was observed at power 20 for all tips where small bubble clouds emerged from the main cloud and were propelled away from the scaler tip into the surrounding water. This can be seen in Figure 2.5 where a cluster has lifted above the main cloud and detaches in the subsequent frames.

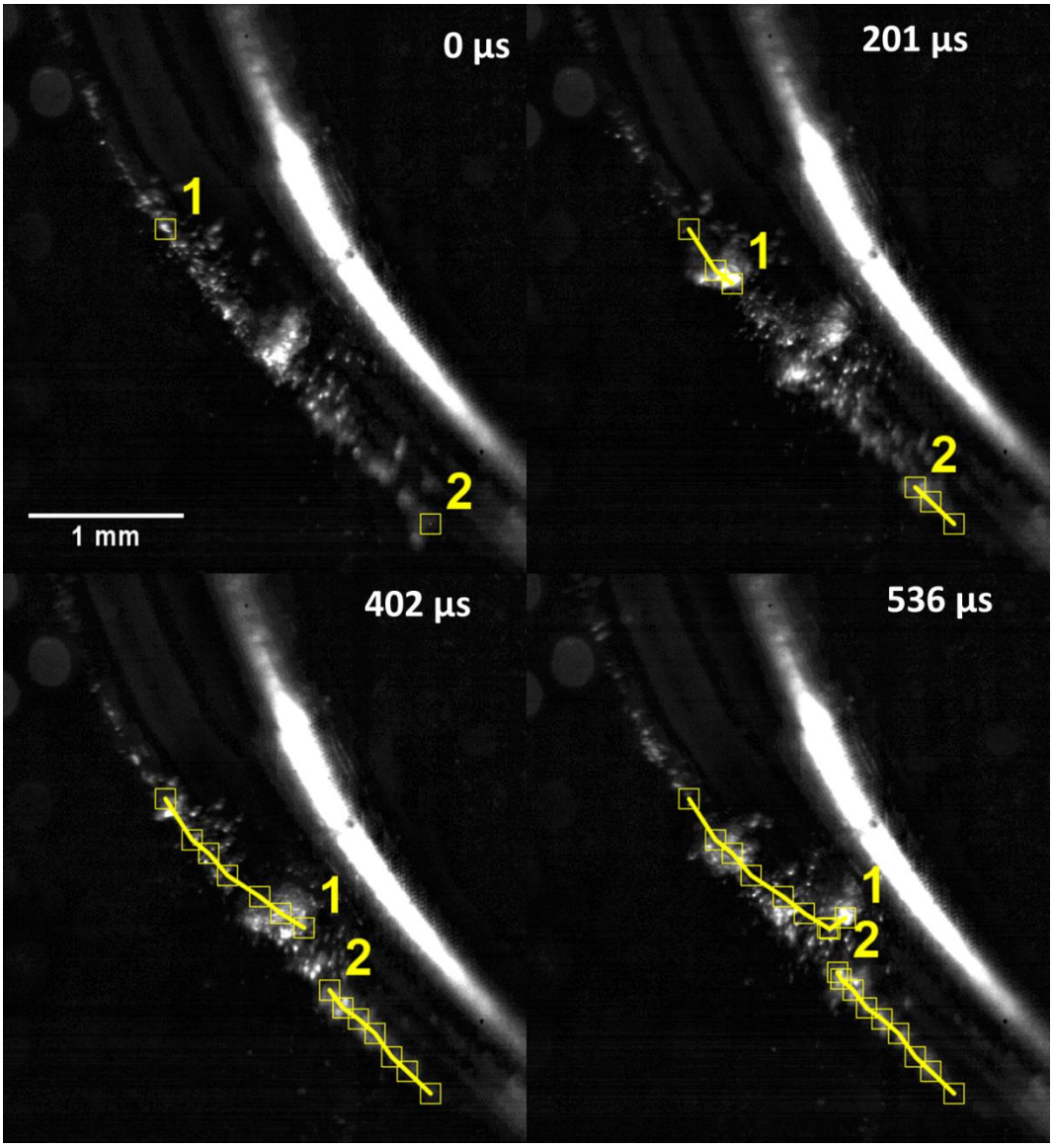

Figure 2.6 Still images from a high speed video of the bend of tip 1 at power 10 (refer to Figure 2.2 to see the part of the tip imaged). Two smaller bubble clusters have been tracked and labelled as they migrate towards a larger bubble cluster in the centre.

The box and whisker plots show only the outliers in the top 5th/95th percentiles for clarity (Figure 2.7). The area of the cloud of cavitation bubbles at the tip was larger at the highest power setting compared to the medium power setting. Tip 10P at power 20 showed the most variation in area. The Mann-Whitney U test was used to compare the median values of each measurement setting. The difference in the areas between the same tip at different powers was statistically significant ($p<0.001$) for all three tips, and the difference between different tips at the same power was also statistically significant ($p<0.001$). Tip 2 showed the smallest area of cavitation out of the three tips measured.

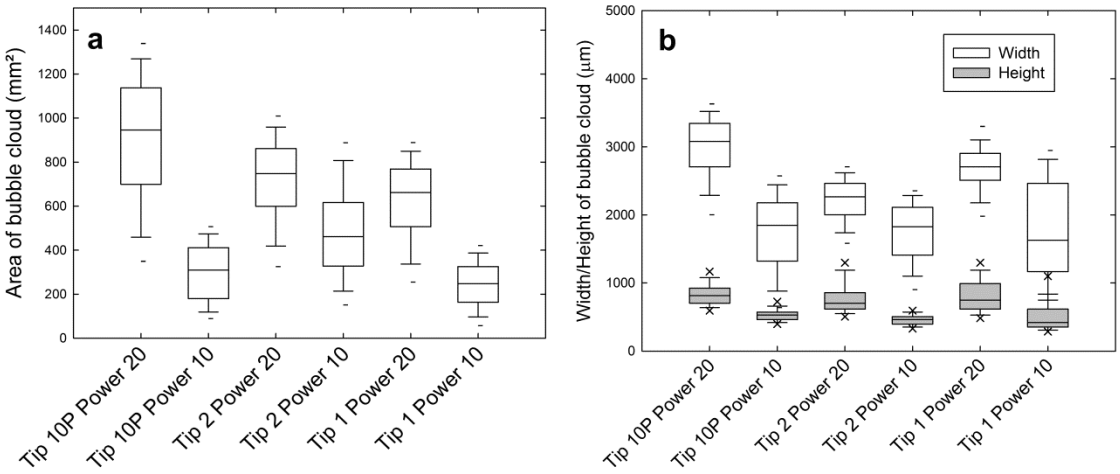

Figure 2.7 Box and whisker plots of (a) the area of the bubble clouds at the tip of three different ultrasonic scaler tips operating at medium and high power (b) the height and width of the bubble cloud. Analysis was done by measuring the cloud in individual frames. For each tip and power combination, three video repeats were used with each video containing 940 images (totalling 2820 images per setting).

The difference in the height and width of the bubble cloud at the tips was also statistically significant between the same tip at different powers ($p<0.001$). This was also valid for the difference between different tips at the same power for all except the following two combinations for which there was no statistically significant difference: tip 10P and tip 2, and tip 10P and tip 1 at power 10 ($p=0.331$ and $p=0.151$ respectively).

The tip displacement amplitude was greater at power 20 compared to power 10 (Figure 2.8). Tip 10P showed the largest displacement at the free end of the tip and tip 2 showed the smallest. However at the bend, tip 1 showed the largest displacement and tip 2 showed the smallest. In between these two antinodes there is a node (point of smallest displacement). Overlaying the high speed images with vibration data shows that cavitation happens at antinodes and does not happen at nodes (Figure 2.9).

The modification of tip 10P showed an increase in cavitation production, whereas the modification of tip 2 caused the cavitation to stop (Figure 2.10). Modified Tip 10P has a similar displacement amplitude to tip 10P whereas modified tip 2 had a smaller displacement amplitude than tip 2 (displacement amplitude for the modified tips was measured manually from the high speed images).

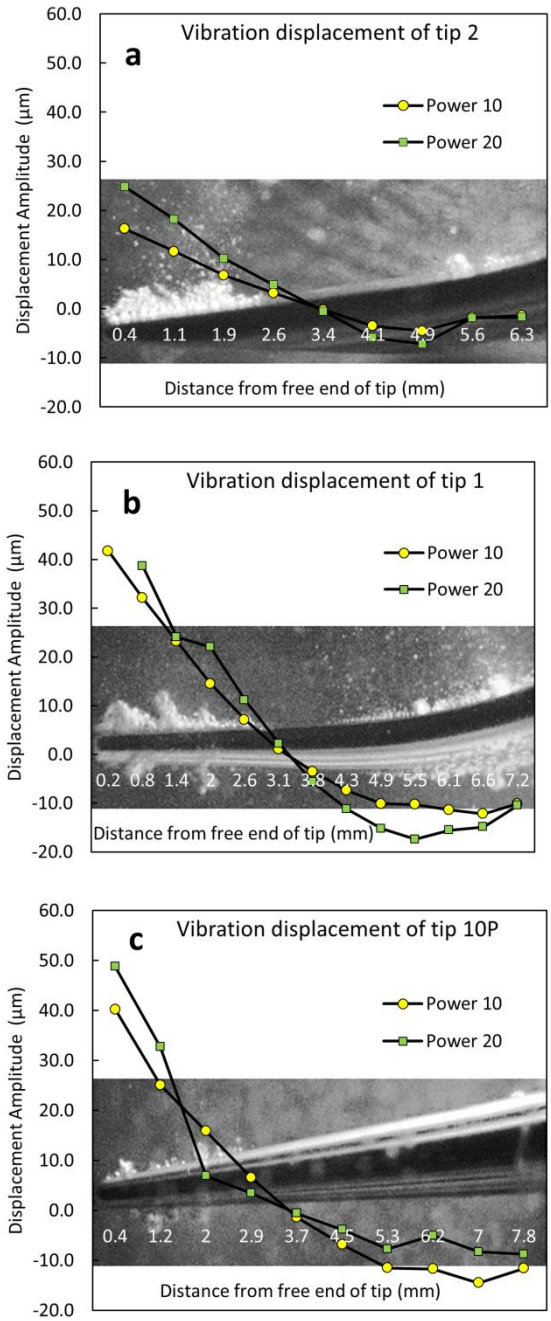

Figure 2.8 Displacement amplitudes of each of the three tips measured at medium power (power 10) and high power (power 20) using scanning laser vibrometry (SLV). The images overlaid on each graph are stills from high speed images of the corresponding tip taken at power 20 and are scaled in the x direction.

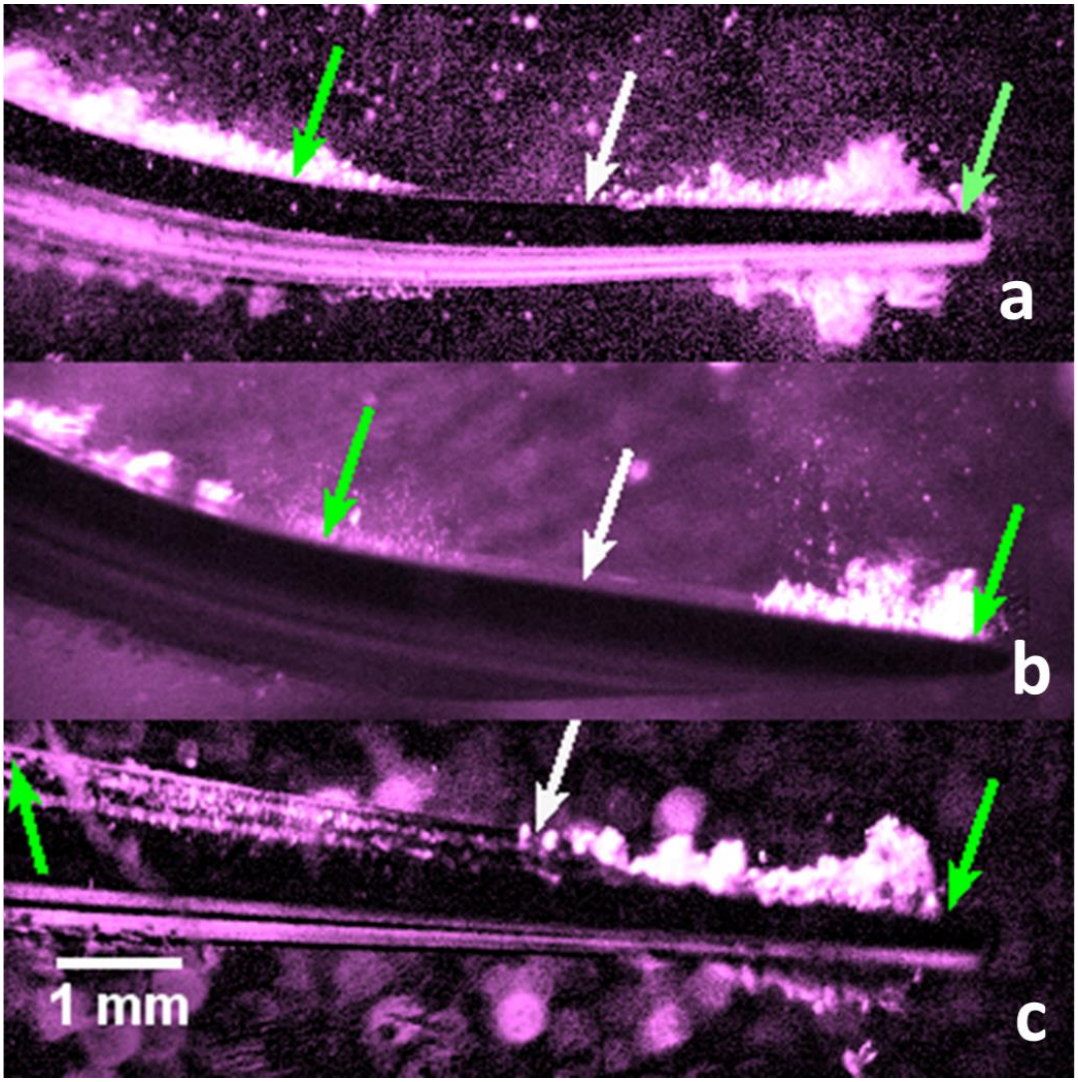

Figure 2.9 Contrast enhanced image stills from a high speed video of tip 1 (a), tip 2 (b) and tip 10P (c) at power 20, showing cavitation occurring around the free end and at the bend of the tips. Green arrows indicate points of largest tip vibration and white arrows indicate the point of least displacement.

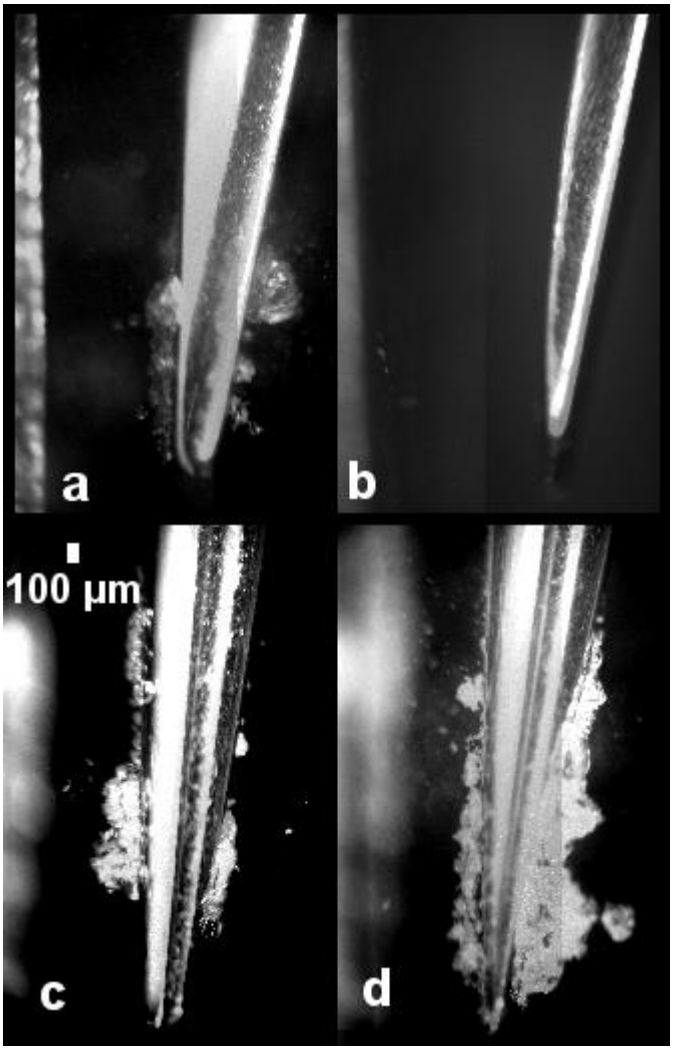

Figure 2.10 Contrast enhanced image stills from a high speed video of tip 2 (a), modified tip 2 (b), tip 10P (c) and modified tip 10P (d). All tips are placed 1 mm away from a wall and operated at power 15. More cavitation can be seen after tip 10P was modified whereas no cavitation can be seen after the modification to tip 2.

2.4 Discussion

Migration of bubbles towards a central bubble cluster was observed (Figure 2.6). This is a result of Bjerknes forces, which act on bubbles in a sound field and arise from the combination of the volume pulsations of the bubble and the acoustic pressure gradient (Leighton et al, 1990). At the bend of the tip in Figure 2.6, smaller bubbles join to form larger bubbles whilst moving along the tip. The larger bubbles come from both directions along the tip then join at a central point before dissolving. Equation 1 (Brennen, 2013) shows that the resonant bubble radius is 697 μm (resonance occurs at 29 kHz).

$$\omega_N = \sqrt{\frac{1}{\rho R_E^2}\left\{3k(p_\infty - p_v) + 2(3k-1)\frac{\sigma}{R_E}\right\}} \qquad [1]$$

ω_N is the natural frequency (ω_N=29 kHz), p_∞ is the pressure in the undisturbed liquid (p_∞ = 100 kPa), p_v is the partial pressure of vapour of the bubble (p_v = 3 kPa), k is the polytropic index (k=1.4), σ is the surface tension coefficient (σ= 0.07 Nm^{-1}), ρ is the density of the liquid (ρ= 1000 kgm^{-3}), and R_E is the bubble radius.

The radius of the large bubbles observed at the bend of the tip is ~190 ± 30 μm. As they are smaller than the resonance size, the primary Bjerknes force causes them to migrate up a pressure gradient (whilst bubbles larger than the resonance size would migrate down a pressure gradient) (Leighton et al, 1990). As the bubbles can be seen to be collecting at a point at the centre of the bend, it is speculated that there is a standing wave and that the bubbles are collecting at a pressure antinode. We also suggest that the smaller bubbles travelling in ribbon-like structures are acoustic streamers, as described by Doinikov et al. (2005) and Lauterborn et al. (2007).

To the best of our knowledge, we are the first to use high speed imaging combined with SLV to study cavitation around ultrasonic scalers. Previous studies using SCL to measure cavitation around ultrasonic scaler tips found minimal cavitation to be occurring at the end of the tip, and the low intensity of luminescence made it difficult to do further analysis to establish the extent of cavitation at the tip end (Lea et al, 2005). The high speed images in this study confirm that substantial cavitation does occur at the end of ultrasonic scaler tips.

Previous work and this work confirms that cavitation occurs at the antinodes, or points of highest displacement, of ultrasonic scaler tips, with no cavitation occurring at the nodes (Felver et al, 2009; Lea et al, 2005). In the literature, this was attributed to the higher amount of liquid being displaced by the scaler at the points where the amplitude of vibration is largest (Felver et al, 2009). In the linear wave theory it can be shown that an antinode (node) for displacement is always an antinode (node) for pressure and vice versa. Therefore, the lowest pressure occurs at an antinode for displacement, which causes cavitation over there. As such, the antinodes are at the start of the cavitation cloud, not the centre (Figure 2.9).

As expected, the cavitation increased at higher power, with the area, width and height of the bubble cloud at the tip being larger at power 20 compared to power 10 for all three tips (Figure 2.7). This correlates with previously reported SCL results which also showed increased cavitation around ultrasonic scaler tips at higher power settings (Walmsley et al, 2013). The variance in the measurements is due to some frames in the image sequence containing no cavitation clouds at particular points in the ultrasonic scaler's oscillation cycle. In this analysis the cavitation on the inner part of the tips was visualised. The cavitation on the outer part of the tips is likely to be slightly different

however it is unlikely to change the conclusions as the overall cloud shape and jetting was similar (for example in Figure 2.9a).

One limitation of this study is the fact that the scaler was submerged in a water tank, with the cooling water turned off, as this setup made high speed imaging easier. However, this is different to a clinical situation, where the scaler operates in air with cooling water flowing around the tip. Consequently the flow fields and possibly the cavitation patterns may be different clinically to what we have observed in this study. For that reason it would be useful to image the scaler with the cooling water turned on, or immersed in a water flow. The resolution of the imaging system with the 2x objective at 4x zoom was 5.6±0.1 µm. Therefore it could be possible that nano-sized bubbles were also generated but could not be detected. In addition, the water temperature in the container was found to increase by approximately 10 ^{0}C after operating the scaler tip for 3 consecutive minutes. Further research is required to determine how temperature affects the amount of cavitation.

The image analysis method used in this work could be applied in a wide range of other studies for analysing bubbles or bubble cloud areas from high speed video frames. To obtain more accurate measurements of the width and height of the bubble cloud, the images could be straightened before performing the calculations (Figure 2.5).

We found that tip 10P, the most pointed, produced the highest area, width and height of cavitation at the tip. Tip 2, which is flat at the end, produced less cavitation at the tip. This could be because tip 10P has the highest displacement amplitude and tip 2 has the least displacement amplitude; the latter has a larger cross-section area. As the

amplitude of pressure is proportional to the amplitude of the displacement (according to the linear wave theory), tip 10P is associated with the largest amplitude of pressure.

Similar effects were observed with the modified tips, with more cavitation and a larger tip displacement observed along the modified version of tip 10P compared with the altered version of tip 2. The displacement amplitude of modified tip 2 reduced considerably, which may be why no cavitation occurred around it. Previous researchers observed that at a similar amplitude of displacement, tips from a similar piezoelectric system (EMS, Nyon, Switzerland) with a wide cross-section caused more cavitation (Felver et al. 2009). They hypothesised that tips with a wide cross-section would be able to displace more water compared to pointed tips. The results of the present study partly agree with this as the levelled form of tip 10P caused more cavitation than the original convex version, but the same was not observed for tip 2. Therefore we suggest that both the vibration amplitude of the tip and its cross-section contribute to increasing cavitation. Further work is needed to understand how the cavitation around ultrasonic scaler tips is affected by tip shape, temperature, irrigant solution, cooling water flow and tip wear.

2.5 Conclusion

This study set out to better understand the cavitation patterns around different ultrasonic scaler tips at different powers. A key strength of the study was the ability to visualise the cavitation around ultrasonic scalers and also to quantitatively measure the difference in the amount of cavitation at different settings and for different tips. Cavitation does occur around the free end of ultrasonic scaler tips. The area of cavitation near the free end of the tips increases with power as well as with the amplitudes of displacement at the tips. The imaging and image analysis protocol developed in this study could be

applied to other studies to quantitatively measure cavitation activity from high speed images. However, these findings were limited by use of a water tank rather than imaging the cavitation in the actual cooling water flowing over the tip, therefore the actual cavitation occurring clinically might be different to what was observed here. Taken together, the results in this study suggest that it is likely that cavitation from ultrasonic scalers could disrupt biofilm in a non-contact mode. This chapter has investigated the overall cavitation clouds occurring around ultrasonic scalers. The next chapter will analyse the individual cavitation bubbles to further understand the bubble dynamics.

3. INDIVIDUAL CAVITATION BUBBLES AROUND ULTRASONIC SCALERS

3.1 Introduction

The dynamics of individual cavitation bubbles are of interest to many scientific disciplines including hydraulics (propellers, turbines and pumps), ultrasound cleaning and biomedical engineering. The aim is to understand the mechanisms underlying the surface cleaning, erosion and sonoporation effects. The characteristics of microbubbles around dental ultrasonic scalers are directly related to cavitation cleaning behaviour but the exact mechanisms are not fully understood (Verhaagen & Rivas, 2016). The aim of this work is to provide insights into how the cavitation can clean biofilms. This will enable manufacturers to develop instruments which use the cavitation cleaning effects optimally (Walmsley et al, 2008).

High speed imaging of bubbles combined with image analysis is a non-intrusive method of experimentally investigating cavitation, and can provide detailed information on bubble structure without interfering with their dynamic activity (Asegehegn et al, 2011; Duhar & Colin, 2006; Garbin et al, 2007; Maurus et al, 2004).

A considerable amount of literature has been published on the mathematical modelling of individual cavitation bubble behaviour to understand how they clean or erode surfaces (Blake & Gibson, 1987; Brennen, 2013; Doinikov, 2005; Gaitan et al, 1992; Lauterborn et al, 2007; Matsumoto & Yoshizawa, 2005; Plesset & Prosperetti, 1977; Tho et al, 2007; Tomita et al, 2002). Chahine et al. simulated bubbles near different boundaries (rigid, elastic and free surface) to measure the pressure driving the bubble and found that the distance between the bubble and the surface to be cleaned influenced the cleaning (2016). Theoretical calculations have also been combined with experimental validation using high speed imaging (Shpak et al, 2013; Tomita et al, 2002). These studies have calculated the evolution of the bubble radius over time and modelled the diffusion inside the liquid for different applications such as drug delivery and erosion. However no such research has been conducted on cavitation bubbles from ultrasonic scalers.

A range of phenomena have been identified which occur during the collapse of cavitation bubbles and may contribute to their cleaning effect. If a cavitation bubble collapses near a boundary, such as a wall or another bubble, it will form a high velocity micro liquid jet which penetrates through the centre of the bubble and impacts the opposite surface with large local stresses (Brennen, 2013). The re-entrant jet penetrates the bubble at a higher velocity than the rest of the collapsing bubble surface, impacting the opposite surface at speeds of over 100 ms^{-1} and a pressure of ~400 MPa (Philipp & Lauterborn, 1998). It is believed that the jet and resulting shock wave imposes a localised high hydrodynamic load on the solid surface nearby, removing the biofilm from the surface (Verhaagen & Rivas, 2016). In terms of damage from erosion, Phillip and Lauterborn identified that the jet only has an effect when the bubble is very near to

or touching the surface, and that the main mechanism is the formation of a vortex ring bubble (a torus shaped bubble rotating poloidally) which collapses producing high pressure pulses (Philipp & Lauterborn, 1998; Tomita et al, 2002). This may also contribute to ultrasonic cleaning but the exact bubble dynamics which lead to biofilm removal remain to be elucidated (Verhaagen & Rivas, 2016). Cavitation bubbles can also lyse cellular membranes and could kill bacterial biofilm as well as disrupting it, but the cellular pathways which occur in bacteria when cavitation is applied have not yet been identified (Erriu et al, 2014; Verhaagen & Rivas, 2016).

Individual microbubbles have been imaged around dental instruments such as endodontic files and lasers (Blanken et al, 2009; Jiang et al, 2010; Matsumoto et al, 2011; Peeters et al, 2014). Peeters et al. showed how air trapped in a root canal can be released and Matsumoto et al. showed that more cavitation occurred in an enclosed root canal model compared to in free space. However these studies are qualitative and have not performed image analysis of individual cavitation bubbles. In addition, very little is known about the characteristics of individual cavitation bubbles around ultrasonic scalers. Bubble dynamics around ultrasonic scaler tips have not yet been studied using high speed imaging combined with image processing. Observing bubble phenomena will help to determine the timescales of growth and collapse, how this is affected by scaler power settings and where nucleation sites are located. This will contribute to discovering how cavitation microbubbles cause biofilm disruption.

The aim of this study is to characterise individual microbubbles around ultrasonic scaler tips using high speed imaging and image processing. Specifically, we aim to observe cavitation bubble phenomena and calculate bubble speed and radius during the growth and collapse phases.

3.2 Materials and Methods

3.2.1 High Speed Imaging

An ultrasonic scaler (Satelec P5 Newtron, Acteon, France) was imaged with tip 10P at various power settings (Power 5, 7, 10, 15, 20) using high speed cameras. A Photron SA1.1 high speed camera was used to image bubbles on different ultrasonic scaler tips at 250,000 fps or 500,000 fps (Figure 2.2). Details of the experimental setups are provided in Section 2.2.1.

To give more details about the bubble collapse phase, an ultra-fast high speed camera (HPV1, Shimadzu Corporation, Japan) was used to image cavitation microbubbles around tip 10P at 1,000,000 fps (Figure 2.3). Details of the experimental setups are provided in Section 2.2.1.

3.2.2 Image Analysis

All image analysis was done using Fiji (distribution of the ImageJ software, US National Institutes of Health, Bethesda, Maryland, USA) (Schindelin et al, 2012). Data graphing was done using SigmaPlot 12.3 (Systat Software, USA) and statistical analysis was performed using SPSS (IBM, USA).

The image analysis process is described in Figure 3.1. Image sequences where individual bubbles were seen to grow and collapse completely within the imaging field of view were used to extract the outline of the bubbles for further analysis.

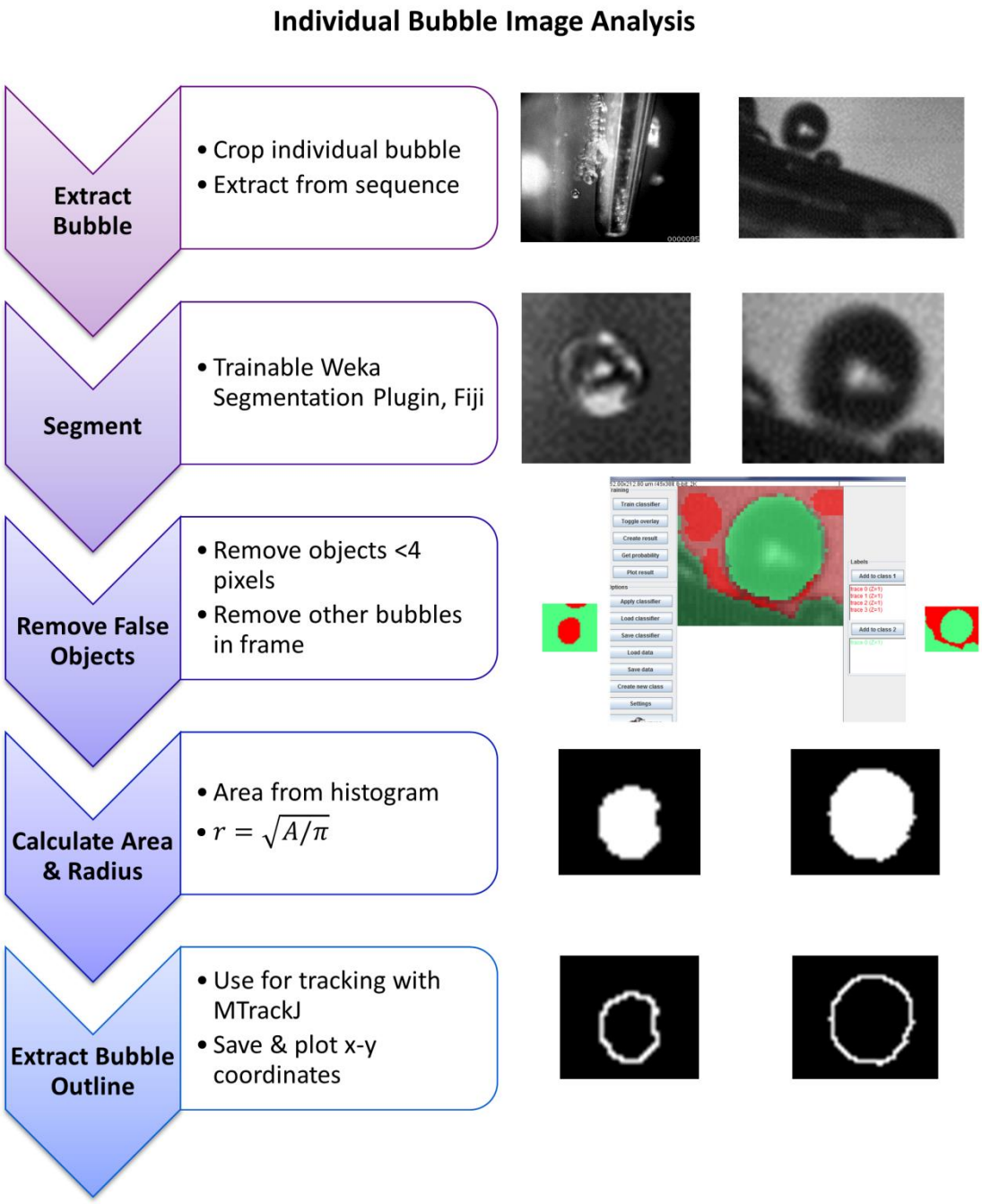

Figure 3.1 Flow chart showing image analysis steps for calculating individual bubble area, radius and speed from high speed image sequences

These images were first cropped and segmented using the Trainable Weka Segmentation Plugin (Arganda-Carreras et al, 2013, Accessed 07.09.2016) (more details on the segmentation process in Section 5.2.5.4). A background subtraction was not applied. Some parts of the background were falsely segmented, so these were eliminated by removing objects smaller than 4 pixels using the Analyse particles plugin. Objects touching the edge of the image were also removed (using the 'exclude on edges' feature in the Analyse particles plugin) to remove other bubbles which were partially in the field of view. The outline of the bubble was then created using the 'outline' function in the Binary menu of Fiji. For the cases where there were multiple individual bubbles in the images, a watershed segmentation was performed to separate bubbles in the image which were touching each other before creating an outline of the binary bubble shapes. These steps were completed for all time points during a bubble's growth and collapse.

The x-y coordinates of the binary outline of two bubbles were saved for an image sequence with a frame difference of 2 μs and plotted as a 3D graph to visualise the bubble localisation during the different stages. 3D visualisation (with the 3rd dimension being time) was also done using the 3D viewer in Fiji for multiple individual bubbles observed simultaneously. To aid in visualisation through time, the image sequence was colour coded to show the different bubble behaviour at different time points.

3.2.2.1 Calculating bubble radius

The equivalent radius of a bubble at each time point was calculated and plotted as a function of time from the binary images of the bubbles. Circularity was assumed to calculate the equivalent radius (*r)* (Equation 2):

$$r = \sqrt{A/\pi} \qquad [2]$$

where *A* is the bubble area. The assumption of spherical bubbles in this study is valid for most of their life cycle except during collapse, which is asymmetrical. It is difficult to accurately perform calculations of an asymmetric bubble because the internal gas dynamics and the fluid mechanics of the liquid need to be taken into account.

3.2.2.2 Calculating speed of bubble wall

Bubble growth and collapse speed was calculated using the MTrackJ manual tracking plugin in Fiji (Meijering et al, 2012). Tracking was done at 8 locations on the binary outline of the bubble for each time point and the mean speed was calculated. The locations on the edge of the bubble were chosen to be equispaced approximately every 45º. The inter-rater reliability of the manual tracking was calculated using the intra-class correlation coefficient (ICC) to test the reproducibility of the tracking method when performed by different people. Seven operators performed manual tracking of one bubble as described above. The average speed of the bubble at each time point was calculated from the 8 tracks. The different speeds obtained by the different users were compared using the ICC.

3.3 Results

Transient cavitation was observed in all high speed videos, i.e. microbubbles continuously grew and collapsed. Stable cavitation (where bubbles oscillate over many cycles without collapsing) was not observed (Figure 3.2). On tip 1 the diameter of the microbubbles observed ranged from 35-150 µm (Figure 3.3). Typical bubble behaviour at the end of tip 10P is shown in Figure 3.2a. One or two individual bubbles first grew and collapsed. After their collapse, many more bubbles or a bubble cloud emerged at the same location of the previous bubble during the next oscillation cycle of the

ultrasonic scaler tip. The cavitation then formed into a cluster of bubbles growing and collapsing at the end of the tip.

There were many frames within the image sequences where no cavitation happened at the tip for many oscillations of the scaler. Once a single bubble formed and collapsed, it prompted the formation of a group of bubbles at the same location. Figure 3.2(b) shows a distinct 'v' shape made by a bubble on tip 10P during the collapse phase. Groups of cavitation microbubbles can be seen around tip 10P at different power settings of the ultrasonic scaler (Figure 3.4). At low power (Figure 3.4a) cavitation can be seen at one point on the tip. At medium powers (Figure 3.4b & c) more cavitation occurs around the whole end of the tip and at the higher powers (Figure 3.4d & e) it increases further, with larger microbubbles.

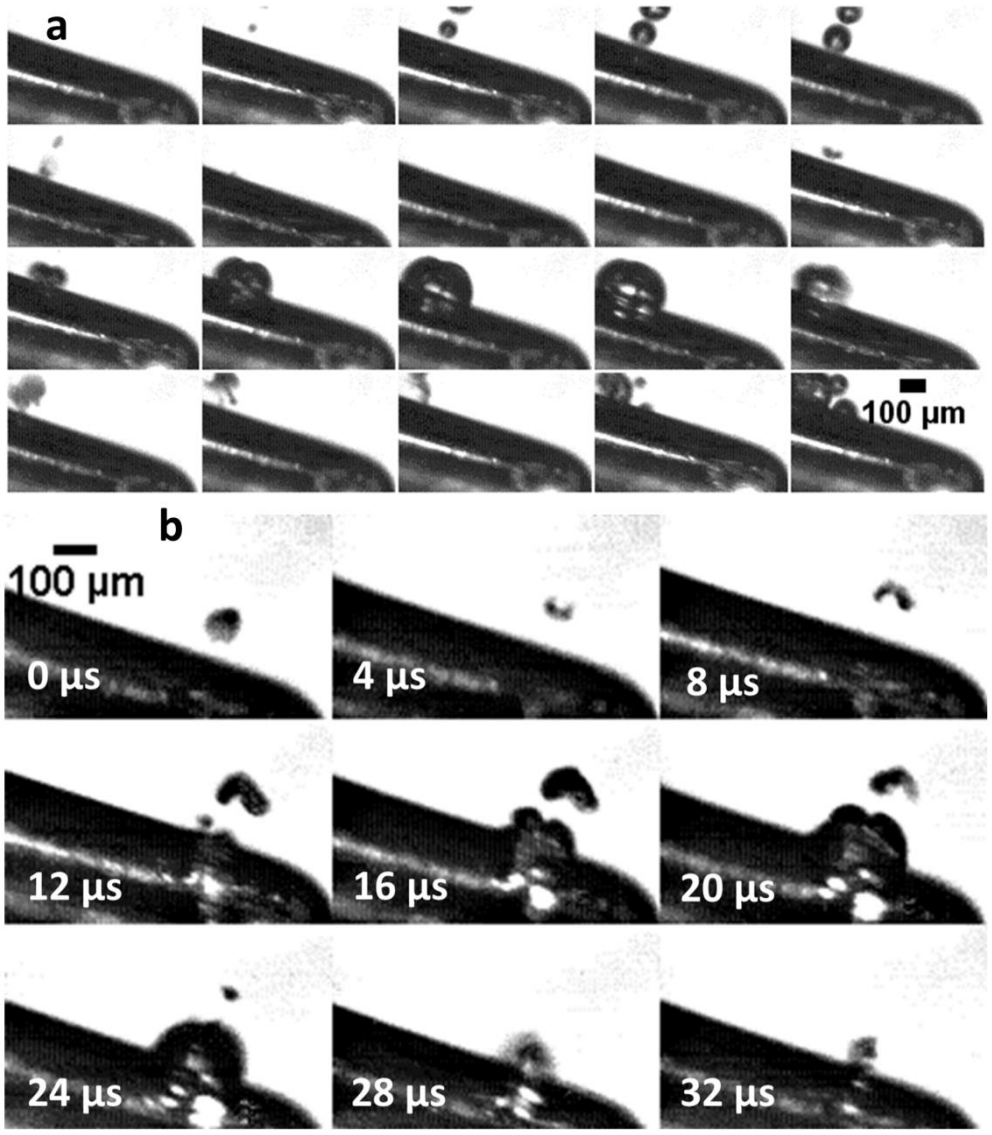

Figure 3.2 Image sequences of bubbles growing and collapsing around at the end of tip 10P. (a) Example of multibubble growth, collapse and regrowth. Frame difference: 4 µs (b) example of a single bubble's 'v' shape collapse.

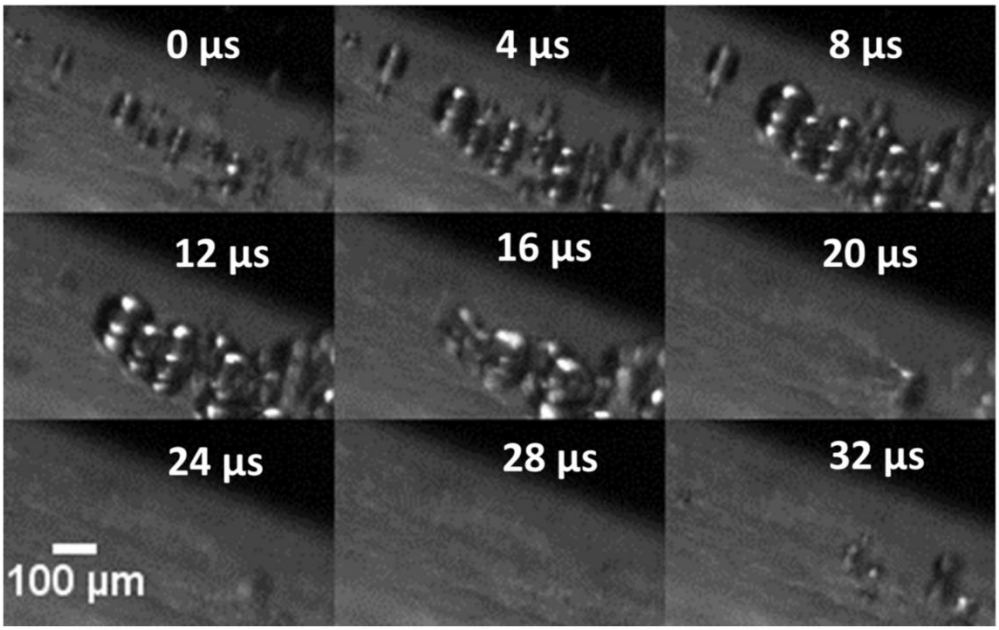

Figure 3.3 Image sequence of microbubbles growing and collapsing around tip 1

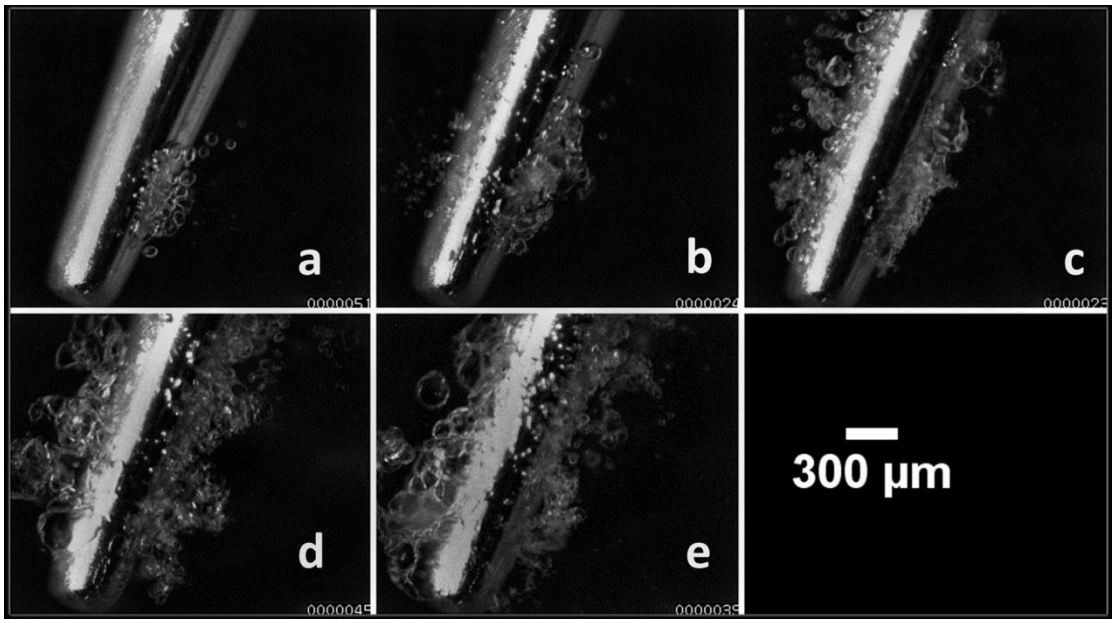

Figure 3.4 High speed images of tip microbubbles around 10P at various power settings (a) power 5 (b) power 7 (c) power 10 (d) power 15 (e) power 20 (maximum power setting)

The 3D plot in time of individual microbubble outlines shows the non-linear bubble collapse which starts at one point on the bubble (Figure 3.5). In (Figure 3.5b) the bubble grows again for 1 microsecond after the first collapse before disappearing. This is not observed in Figure 3.5(a).

There were more cavitation clouds around the tip rather than individual bubbles. A group of individual microbubbles could be seen in one high speed video (Figure 3.6, highlighted by the rectangle). The evolution of these bubbles over time can be visualised more clearly in Figure 3.7. They start as small microbubbles shown in magenta, then evolve to the larger microbubbles shown in cyan and green. One of these jets upwards (shown in yellow) before collapsing.

Figure 3.8(a) shows an example of the manual tracking done with MTrackJ and the tracks drawn by an operator at 8 points on the bubble. The single measures ICC for the manual tracking was 0.993 (Figure 3.8b). An example of the bubble outline extracted from the image sequences is shown in Figure 3.8(c) in magenta overlaid on the original cropped bubble images. The corresponding original image sequence in Figure 3.8(d) shows the individual bubble growing and collapsing near the end of tip 10P. Out of the bubbles analysed, the maximum radius ranged from ~40 μm to ~80 μm (Figure 3.9). It increased over time before reaching a peak and decreasing rapidly when the bubbles collapsed. The speed of bubbles remained constant for the first half of the growth cycle and then increased rapidly during the collapse phase (Figure 3.10).

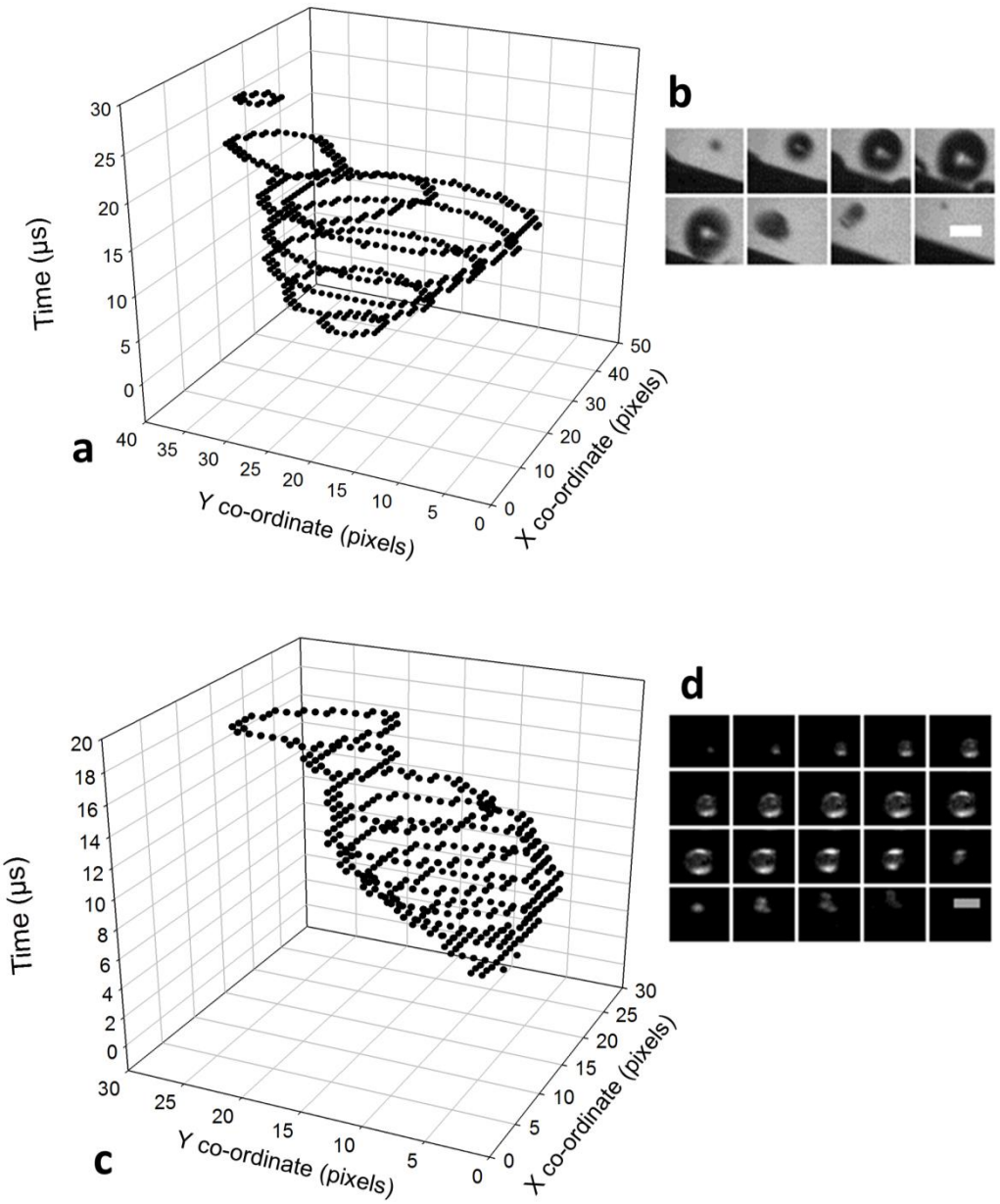

Figure 3.5 (a,c) 3D plots in time of the x-y coordinates of bubble outlines as they grow and collapse, showing the position of the bubble at each time point. The origin in the graphs refers to the top left corner of the high speed image. Images from cavitation around tip 10P at power 10. (b,d) corresponding original cropped images from high speed video. Scale bar represents 100 µm.

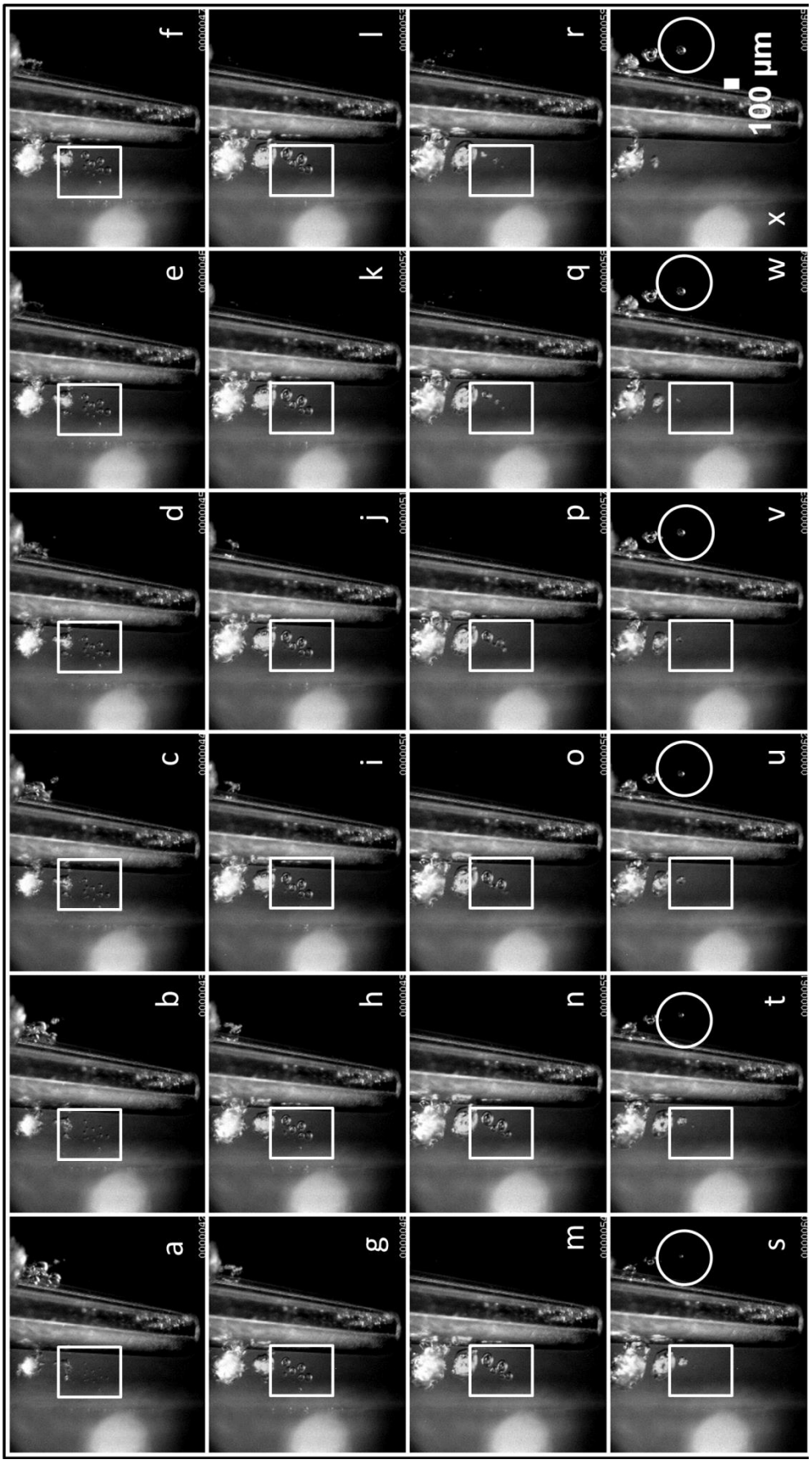

Figure 3.6 High speed image sequence of cavitation occurring around tip 10P, with a group of microbubbles (highlighted in rectangles) and an individual micro bubble (circled). Time difference between frames is 1 µs

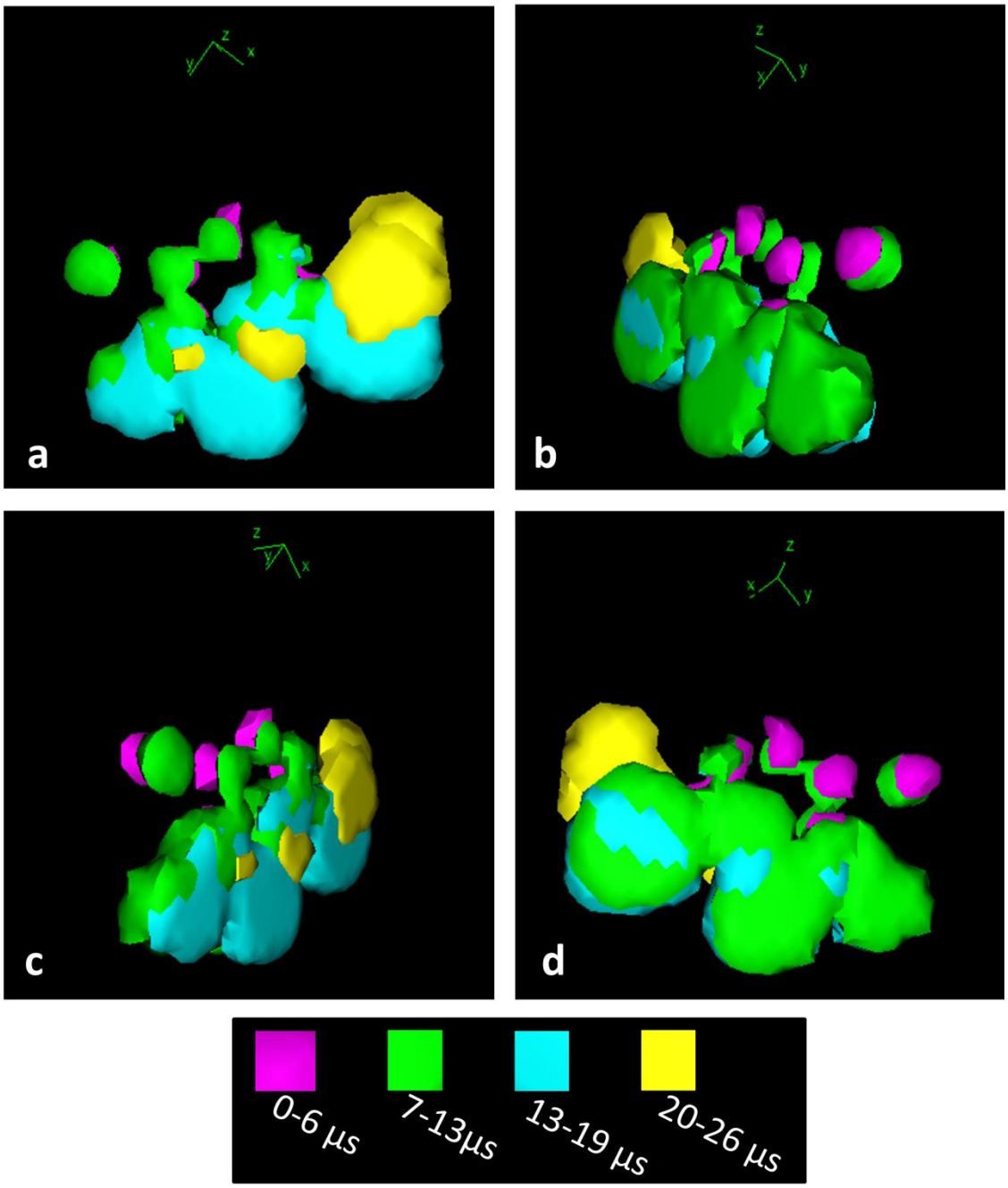

Figure 3.7 Three dimensional views in time of the group of microbubbles rectangled in Figure 3.6. Colour scale shows evolution of bubbles over time. Z dimension is in time

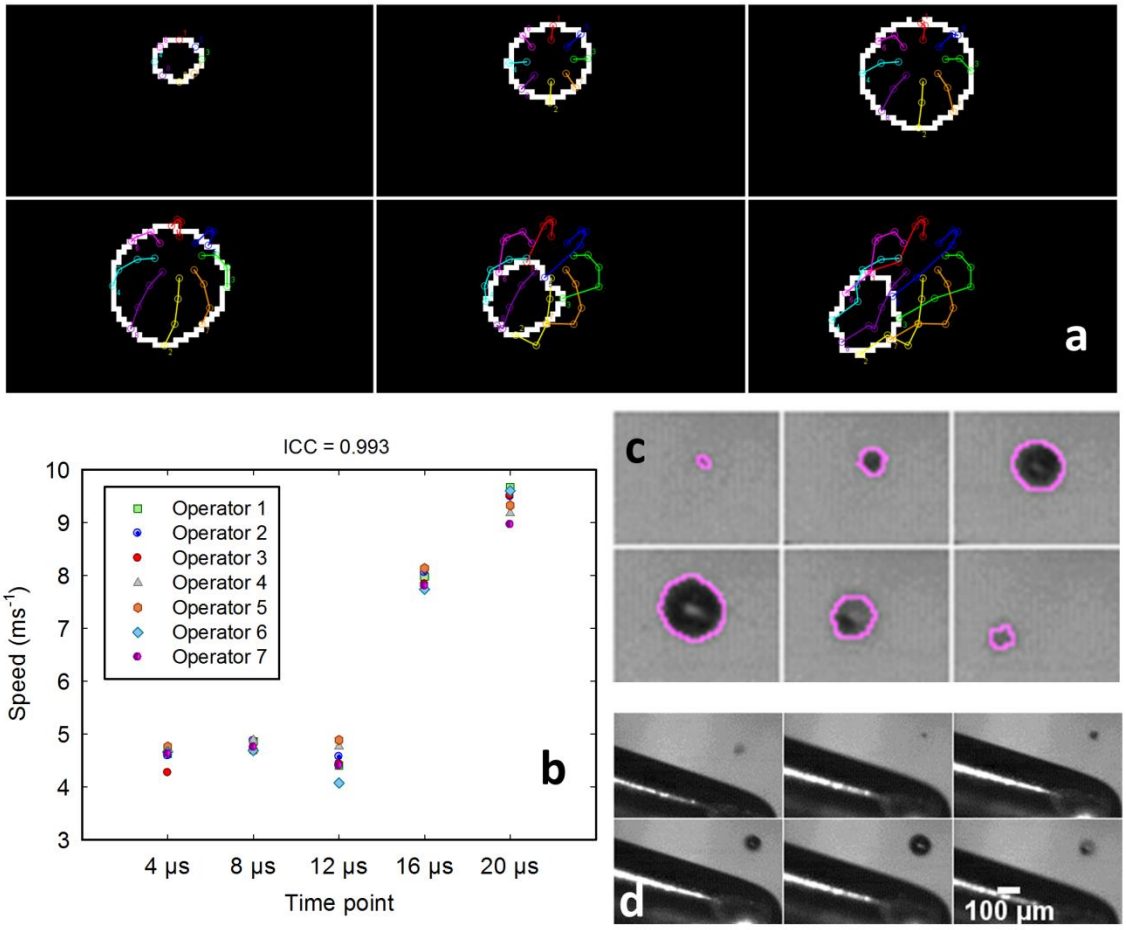

Figure 3.8 (a) example of the MTrackJ plugin showing the tracks at 8 points selected manually (b) Dot plot showing the mean bubble speed measurements from 7 people at each time point, demonstrating that the manual tracking procedure is reproducible (c) example of an individual bubble used for tracking, with the binary outline overlaid in magenta (d) original image sequence of the bubble near tip 10P. Frame interval is 4 µs

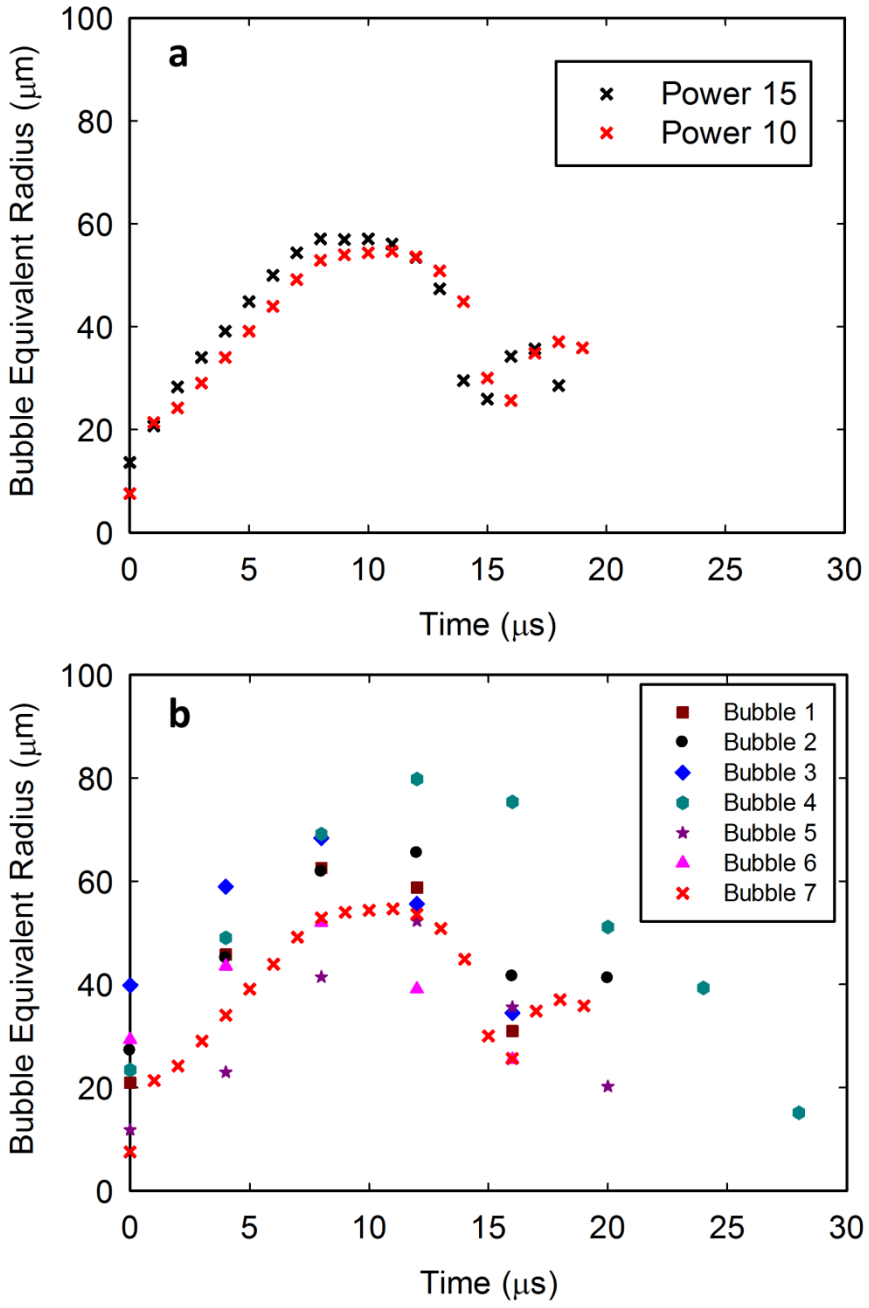

Figure 3.9 (a) Bubble equivalent radius plotted over time for single bubbles around tip 10P at power 10 and power 15.Extracted from images taken at 1 million fps (b) Bubble equivalent radius over time for single bubbles around tip 10P at power 10. The cross symbol plot is the same as in (a) at 1 million fps, the others are from image sequences taken at 250 kfps

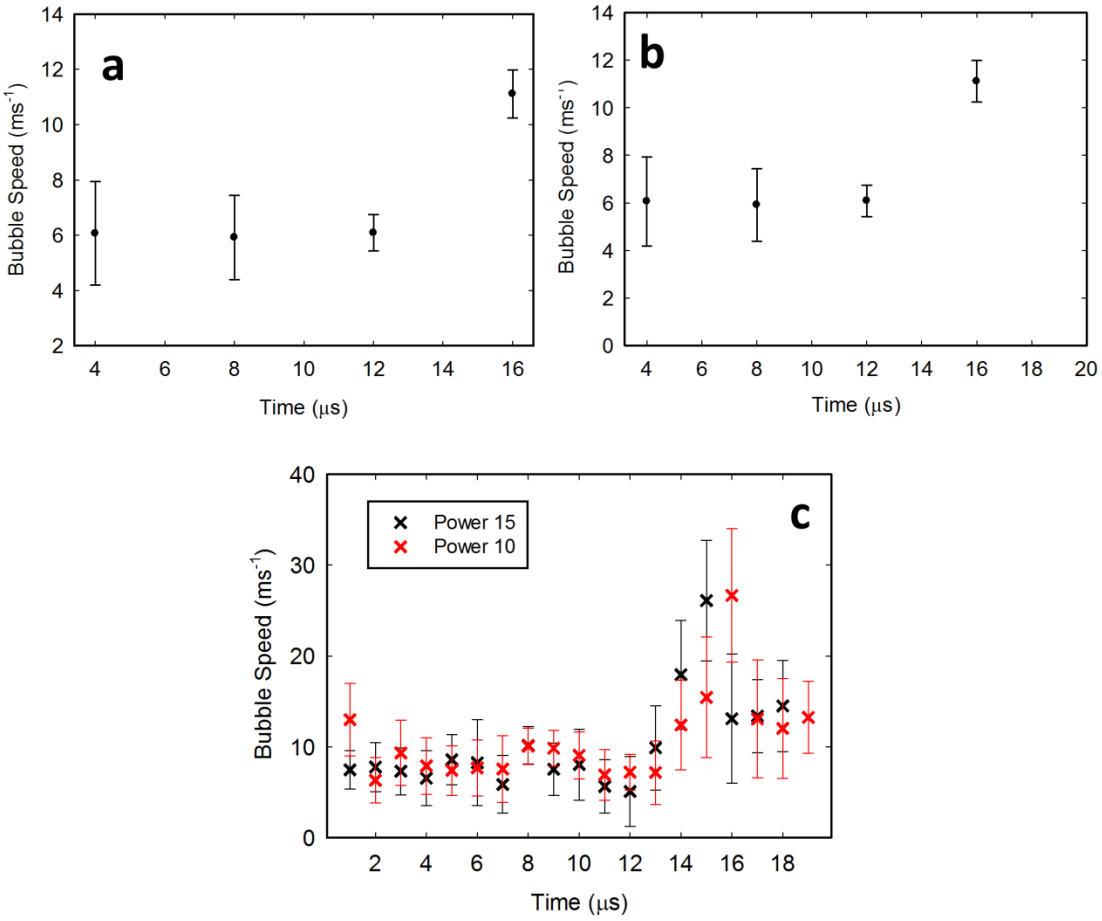

Figure 3.10 Plots of the speed of the bubble wall over time (a) mean and standard deviation of three bubbles which expanded and collapsed within 16 μs (b) mean and standard deviation of two bubbles which expanded and collapsed within 20 μs (c) mean and standard deviation of one bubble at power 10 and one bubble at power 15.

3.4 Discussion

High speed imaging of ultrasonic scalers showed that whilst the majority of cavitation is in the form of clouds, individual microbubbles were also observed. Image analysis and manual tracking enabled bubble radius and speed to be calculated at various points in their life cycle.

The scaler tip was operated at 29 KHz giving an oscillation period of approximately 34 µs. The oscillation period of the single microbubbles ranged from 16-20 µs (Figure 3.10). Therefore one acoustic cycle is equal to two deformation cycles of a bubble.

At power 5 bubbles appear at one point on the end of the scaler tip. They may have occurred at this point in particular because that is the location of the pressure antinode at that power setting. Cavitation bubbles grow above the tip just as it reaches its maximum amplitude whilst moving upwards, and continue to grow larger as the tip moves downwards (Figure 3.2). They then collapse when the tip reaches its maximum amplitude whilst moving downward or as soon as it starts to move upward. This shows that the rarefaction phase of low pressure happens on the side which the scaler is moving away from. This was also observed for bubble clouds. Therefore bubbles collapse on one side of the scaler tip whilst others grow on the opposite side, and this reverses at the tip moves.

At the end of tip 10P a single bubble split into two bubbles and formed a V-shape, before moving away from the scaler (Figure 3.2b). This is common during the formation of high-speed micro-jets when a cavitation bubble collapses near a boundary and could be due to the Bjerknes force associated with the pressure wave generated at the vibrating tip (Blake & Gibson, 1987; Lim et al, 2010). The bubble collapse happens much faster than the growth phase so the micro-jet cannot be visualised in this set of

images taken at 250,000 fps. In this case the closest boundary was the ultrasonic scaler tip itself, so the bubble collapsed onto the tip.

All individual bubbles analysed in this study collapsed asymmetrically (Figure 3.5). This suggests that they were influenced by proximity to the scaler tip or to other bubbles, since bubble collapse near a boundary is asymmetric (Brennen, 2013). This can also be seen in Figure 3.7 where the bubble coloured in yellow moved upwards before it collapsed. This happened because it was attracted to the bubble cloud above it which can be seen in Figure 3.7. This is in line with theoretical calculations which show that collapse propagates from the outer bubbles to the centre of a bubble cloud (Blake et al, 1999).

The high ICC value shows good inter-operator reliability in manually tracking the bubble growth and collapse using the MTrackJ plugin, therefore this method is reproducible. The dot plot (Figure 3.8b) further demonstrates good agreement between the different speeds measured by the different operators. The tracking procedure could be automated to decrease analysis time (Chenouard et al, 2014)

Two bubbles analysed at different power settings had similar radii (Figure 3.9a) but larger bubbles can be seen at higher power settings in Figure 3.4. Therefore although this work shows that increasing power causes an increase in the quantity of cavitation microbubbles, further research is needed to confirm how the power of the scaler affects their size. The radius of the bubbles in Figure 3.9a increases again after 15 µs. This is due to bubble regrowth occurring after the first collapse phase.

In Figure 3.10c, plotted from image sequences taken at 1 million fps, the maximum speed of the bubbles reached approximately 25 ms^{-1}. However in Figure 3.10a & b,

plotted from image sequences taken at 250k fps the maximum speed was 10-12 ms^{-1}. This discrepancy is because the lower frame rate of 250k fps could not capture the increase in speed.

Microjets could not be visualised in this study because the frame rate is too low. As typical microjets have a velocity of 100m/s (Philipp & Lauterborn, 1998), for a cavitation bubble with a maximum radius of 60 µm (as was often observed in this study) the microjet would travel ~150 µm as it passes through and out of the bubble. To visualise this over 10 frames as done by Philipp and Lauterborn (Philipp & Lauterborn, 1998), a frame difference of 150 ns is needed, which requires a high speed camera to record at 6.6 million fps or higher.

This work can be improved and further developed in several ways. Most high speed imaging studies of cavitation microbubbles use laser generated bubbles whose sizes and locations can be precisely controlled. As we have imaged cavitation occurring around a clinical instrument, it is difficult to localise the bubble dynamics, making it challenging to image individual bubbles in the restricted field of view of the Photron camera. In addition many individual bubbles were obscured by the bubble clouds so their outline could not be extracted using the image analysis procedure used in the study. This meant that only a small number of cavitation bubbles could be analysed and therefore the samples may not be representative. Further work can be done using the methods established in this study to analyse bubble microjets and their effect on biofilm removal. The radii produced by ultrasonic scaling and endodontic instruments have not previously been published therefore it is difficult to compare these results with previous studies. Future work can involve comparing experimental results to theoretical predictions. It is difficult to calculate the exact focal depth of the camera due to the

bespoke setup. It is possible that only a part of a bubble was in focus during imaging and therefore its maximum size may have been inaccurately calculated. However this is unlikely to have occurred because the individual bubbles imaged were completely in focus and there were no out of focus regions observable around the bubble.

Further experimental work could be done at higher frame rates to investigate the bubble jet formation. Combining experimental observations with theoretical simulations of bubble processes can obtain further information on which parameters affect the jetting speed and bubble size, and eventually help to create instruments which produce optimal cavitation bubbles for biofilm removal.

3.5 Conclusion

In this investigation, the aim was to gain a better understanding of the individual cavitation bubbles that occur around ultrasonic scaler tips. A strength of this study is the extraction of a range of parameters from the images including the rate of bubble growth and collapse. Cavitation bubble dynamics around ultrasonic scalers have been visualised and analysed to show the average sizes of microbubbles and their size and speed during various phases of their life cycle. The study was limited by a small sample size due to the difficulty of imaging individual cavitation bubbles. Overall, this study has highlighted the usefulness of image processing and high speed imaging in evaluating cavitation around ultrasonic scalers. So far this thesis has focussed on the cavitation dynamics of ultrasonic scalers. The next phase of the study involves using the information obtained about the locations of cavitation around the ultrasonic scaler tips to develop methods to evaluate the effects of the cavitation for biofilm removal. This will firstly involve evaluating removal in 3D and secondly quantifying removal at nanometre resolution.

4. MICRO-COMPUTED TOMOGRAPHY IMAGING OF ARTIFICIAL BIOFILM REMOVAL IN 3D

4.1 Introduction

The ability to image biofilm in 3D is important for a wide range of scientific and industrial processes such as evaluating removal, monitoring growth and evaluating biofilm models (Iltis et al, 2011). Imaging disrupted biofilm in 3D on a tooth or implant model can show the macroscale cleaning effectiveness of cavitation and where the instrument is most and least effective. 3D imaging can also give information on localisation of biofilm on particular materials, indicating where the most and least growth occurs. This will provide information that may be useful to clinicians and manufacturers who are wishing not only to improve ultrasonic scaler designs but also to assess the cleaning ability of different instruments. This would also be useful to other researchers in Dentistry studying periodontal therapy methods and in the wider biofilm research area such as for environmental life sciences and biomaterials (Beyenal et al, 2004; Costerton et al, 1999; Donlan, 2001; Haisch & Niessner, 2007; Jones et al, 2012; Mueller et al, 2006). An area that has not been researched in depth is the use of

microCT to image biofilm for dental applications. There are no studies which calculate its thickness on a 3D structure such as a tooth from microCT data (Santini et al, 2015). As this type of imaging has not been done extensively before, we wish to develop analysis methods and protocols to image biofilm removal. Biofilm imaging in 3D can be done on a 2D surface, in a flow cell or on an opaque 3D object.

Confocal laser scanning microscopy (CLSM) gives sub-micron resolution (Seymour et al, 2004; Xavier et al, 2003) allowing imaging of live biofilm in its natural state (Neu et al, 2010) from which roughness, porosity and thickness can be calculated (Neu & Lawrence, 2015). The disadvantages are that, as fluorescent staining is required, not all oral bacteria can be labelled and this may also interfere with cell activity causing inaccurate measurements (Inaba et al, 2013). Ultrasound and optical coherence tomography (OCT) have also been used to image biofilm in 3D on a surface. These do not require staining, but the resolution is lower than CLSM (approximately 20 µm/pixel) (Haisch & Niessner, 2007; Shemesh et al, 2007; Vaidya et al, 2011)

The above-mentioned methods can image biofilm on a horizontal surface. It can also be imaged live in 3D in a transparent flow cell. This has been done using OCT (Xi et al, 2006) and Magnetic Resonance Microscopy (MRM) (Gjersing et al, 2005; Manz et al, 2003; Seymour et al, 2004), and flow velocity and shear rate can be calculated. However OCT and MRM also have relatively low resolution (up to 20 µm/pixel) (Seymour et al, 2004) and it is difficult to image opaque or complex 3D structures. Biofilm has been imaged inside a flow cell using synchrotron based microCT for the first time at a resolution of 4 µm/pixel (Iltis et al, 2011). However synchrotron sources are not readily accessible and the technique has not been used to image biofilm on different materials.

It is more useful to image biofilm on opaque materials to assess its growth/removal on different surfaces and to study distribution and localisation. Biofilm has been imaged on a range of opaque 3D surfaces using benchtop x-ray micro computed tomography (microCT) with a resolution of 5-10 µm/pixel (Davit et al, 2011; Iltis et al, 2011; Santini et al, 2015). A contrast agent is required to differentiate between the biofilm and other materials such as water which have similar x-ray absorption coefficients (Thomas et al, 2014). Selecting the correct contrast agents and their required concentration is a challenge. Davit and colleagues used potassium iodide and barium sulphate to image biofilm in porous media using benchtop microCT (Davit et al, 2011). This was a proof of principle study to show that biofilm can be imaged using such a system, and the authors acknowledge the need for improved image processing methods to segment the biofilm more accurately. In addition, the use of contrast agents may complicate image interpretation, and the ionising x-rays may damage live biofilm. Davit et al. have confirmed that a 3 hour exposure of biofilm to x-rays does not cause changes in its geometry, but further investigations into the effects of radiation exposure on biofilms are needed.

Scanning laser optical tomography (SLOT) is an advancement of optical projection tomography, which is similar to microCT, but uses light in the visible spectrum and allows detection of fluorescence (Heidrich et al, 2011). Heidrich et al. used SLOT to image biofilm localisation on dental implants with a resolution of 12 µm/pixel (Heidrich et al, 2011). Although SLOT is expected to cause less biofilm damage than x-ray based techniques, it is less accessible than microCT.

The overall aim of this research is to investigate biofilm disruption from an ultrasonic scaler on optically opaque materials such as teeth and dental implants, therefore we used

microCT. The aims of this particular study are to investigate methods of imaging artificial biofilm on a tooth and to calculate biofilm removal in 3D. This will give insights into the efficiency of cavitation from an ultrasonic scaler. As this is a preliminary study, we will use a synthetic hydrogel to mimic biofilm because of ease of application and imaging. We investigated two methods: imaging on a real tooth using dual energy and imaging on a plastic model tooth for quantitative measurements. We studied dual energy as a method of imaging both the tooth and the hydrogel simultaneously. As teeth have a large x-ray attenuation coefficient and hydrogel/biofilm has a low attenuation coefficient, a higher beam energy is required to image teeth and a lower beam energy is required to image hydrogel/biofilm. Imaging at two energies and combining the scans could therefore aid in visualisation of both the tooth and hydrogel.

Aims of the study:

1. Develop a method to calculate artificial biofilm removal in 3D on a human tooth and plastic tooth model
2. Use this method to evaluate the effectiveness of cavitation in biofilm removal

We hypothesised that hydrogel can be stained and imaged in microCT on a human tooth and segmented using dual energy imaging and that hydrogel removal can be calculated in 3D from dual energy microCT scans and scans taken before and after removal.

4.2 Materials and Methods

4.2.1 Dual Energy Method of Segmentation

This study used modified versions of a hydrogel formulated by Macedo et al. (2014a) for mimicking biofilm in the root canal. The storage and loss moduli of the hydrogel have previously been found to be similar to those of real biofilm. A hydrogel with added contrast agent was produced by dissolving 3 g gelatine and 0.06 g hyaluronan in 35 ml filtered water and 10 ml Lugol's solution (1% Iodine and 2% Potassium Iodide). The hydrogel was centrifuged at 3000rpm for 10 minutes to remove air bubbles and stored at 4^0C until use.

Two extracted human premolar teeth were used for dual energy imaging. The use of teeth was authorised by a licence from the United Kingdom Human Tissue Act (HTA) (Licencing number: 12313, Clinical Research Network Consortium Reference: BCHCDent355.1548.TB, Ethical Approval Number 90/H0405/33). After extraction, the teeth were disinfected in 15 mM Sodium Azide, washed under running water for 8 hours and stored at -20^{o}C until use. Before use, the hydrogel was melted in a weighing boat on a hot plate and applied to the crown of the tooth. After hydrogel application the teeth were stored at -80^0C until microCT imaging, which was done within 24 hours.

For dual energy imaging, each tooth was scanned at low energy and high energy. Three low energies were tested to determine the most accurate: 30 kV, 40 kV and 50 kV (± 3 kV) without a filter. High energy scans were taken at 80 kV with a 0.5 mm Al filter (SkyScan 1172 microCT scanner, Bruker, Belgium). The scans were taken consecutively without moving the sample in between scans, unless a flat field correction was taken. A flat field correction was applied when the operating voltage was changed from low energy to high energy. In this case the samples were returned to the same

imaging position after applying the correction. The following settings were used for dual energy scanning: pixel size: 9 µm, source current: 100 µA, rotation step: 0.7°, frame averaging: 3.

Images were reconstructed with NRecon software (Bruker, Belgium) using uniform attenuation coefficients. Image analysis was done using Fiji (distribution of the ImageJ software, U. S. National Institutes of Health, Bethesda, Maryland, USA) (Schindelin et al, 2012), Dehist (Bruker, Belgium) and MATLAB (The Mathworks, MA, USA). 3D Slicer (available from http://www. slicer. org/) was used for image co-registration.

The Dehist software was used to combine and segment the low and high energy 2D reconstruction slices (Figure 4.1). It works by creating a dual histogram of the low and high energy images. The operator then uses this histogram as a guide to choose a threshold value to segment each image. The T-bar can be manually adjusted until the desired segmentation is achieved. In this study the same settings (threshold for low energy image, threshold for high energy images and angle of T-bar) were used for each segmentation performed using dual energy to ensure consistency.

Without any noise reduction applied, noise was also included in the segmentation. Noise reduction methods were therefore tested in Fiji by applying different filters (mean, minimum, remove outliers, Gaussian blur) on a 2D reconstruction slice from each of the low energy scans (Figure 4.2). The effectiveness of each filter was evaluated by calculating the signal to noise ratio: the noise was calculated from the mean intensity inside seven ROIs measuring 540 x 540 pixels placed in areas of the image where there was no hydrogel or tooth. The average signal value in the hydrogel was found using the same method on areas where there was hydrogel in the image. The

removed outliers filter increased the S/N more than the other noise removal techniques (Figure 4.3) and was therefore applied to all the low energy images before segmenting in Dehist. The removed outliers filter calculates the median value inside a certain pixel area where the pixel radius is supplied by the user (a radius of 50 was used in this study). The user must also set a threshold value (a threshold of 1 was used in this study) – so any pixels which vary from the median value by the threshold value are replaced in raw (uncalibrated) units.

The accuracy of the dual energy segmentations was evaluated by comparing to reference segmentations (Figure 4.4 and Figure 4.5). 3D reference images were created by subtracting a scan taken at 80 kV from a scan taken at 30, 40 or 50 kV and binarising. The reference segmentation was compared to the corresponding dual energy segmentations for each slice in the scan. Sensitivity (true positive rate) and specificity (true negative rate) were calculated using MATLAB and plotted as a receiver operating characteristics (ROC) curve. To see how robust the dual energy segmentation method was against noise in the image, sensitivity and specificity was calculated on two different scan sets, with differing amounts of noise. The scan set with more noise (referred to as scan set 2) was performed in the same way with the same scan settings, but at a different time point, therefore there were differences in instrument calibration and the x-ray source may have decayed over time. The noise was a combination of ring artifacts and quantum mottle (Goldman, 2007). The quantum noise results from the limited number of x-rays hitting the detector at low energy because they are absorbed by the tooth which has a high attenuation coefficient. The ring artifacts are a due to miscalibration of detector elements (Barrett & Keat, 2004).

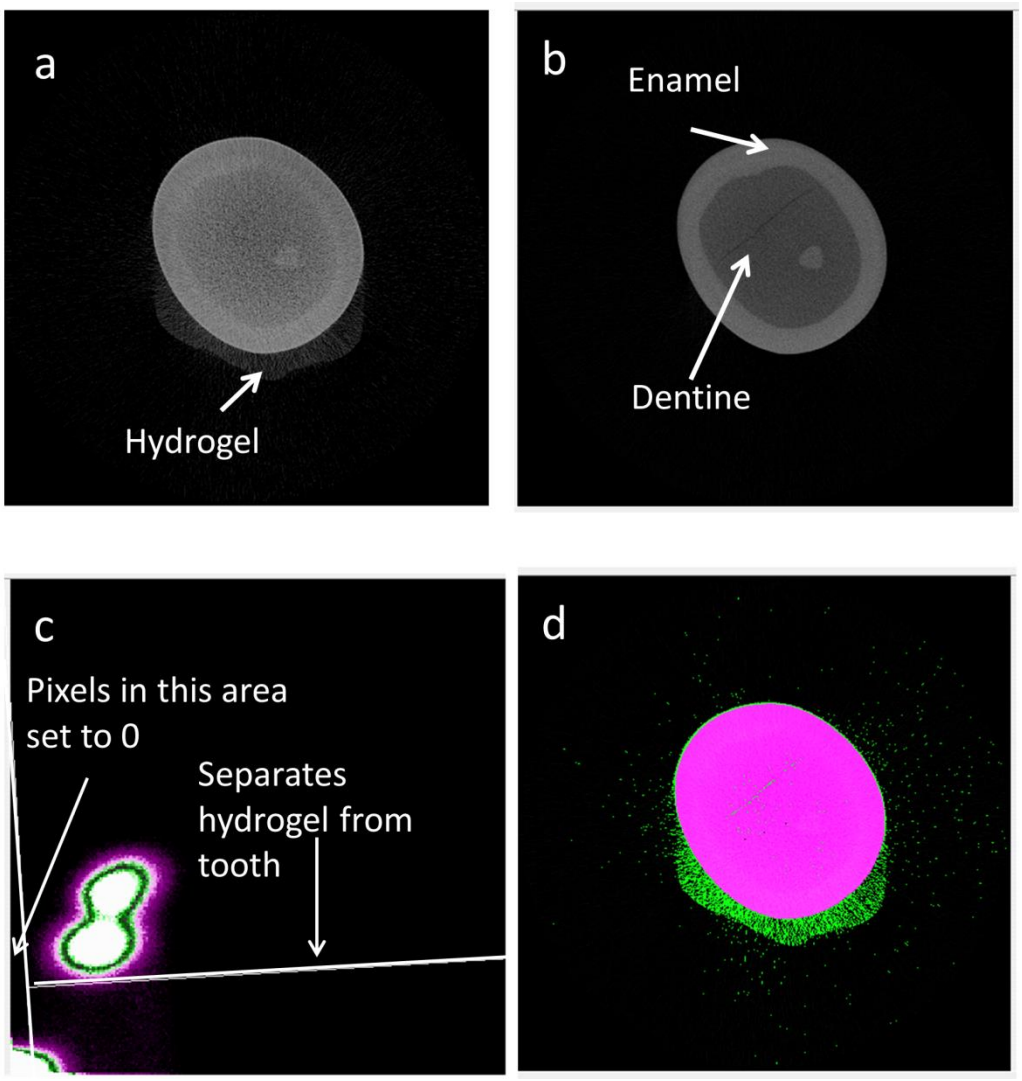

Figure 4.1 Modified screenshot of the Dehist dual energy segmentation program. (a) microCT reconstruction slice from a low energy scan (b) microCT reconstruction slice from a high energy scan (c) histogram of the low and high energy images. The T-bar shows where the segmentation takes place. This can be oriented by the operator to adjust the segmentation. (d) Segmented image showing tooth (magenta) and hydrogel (green)

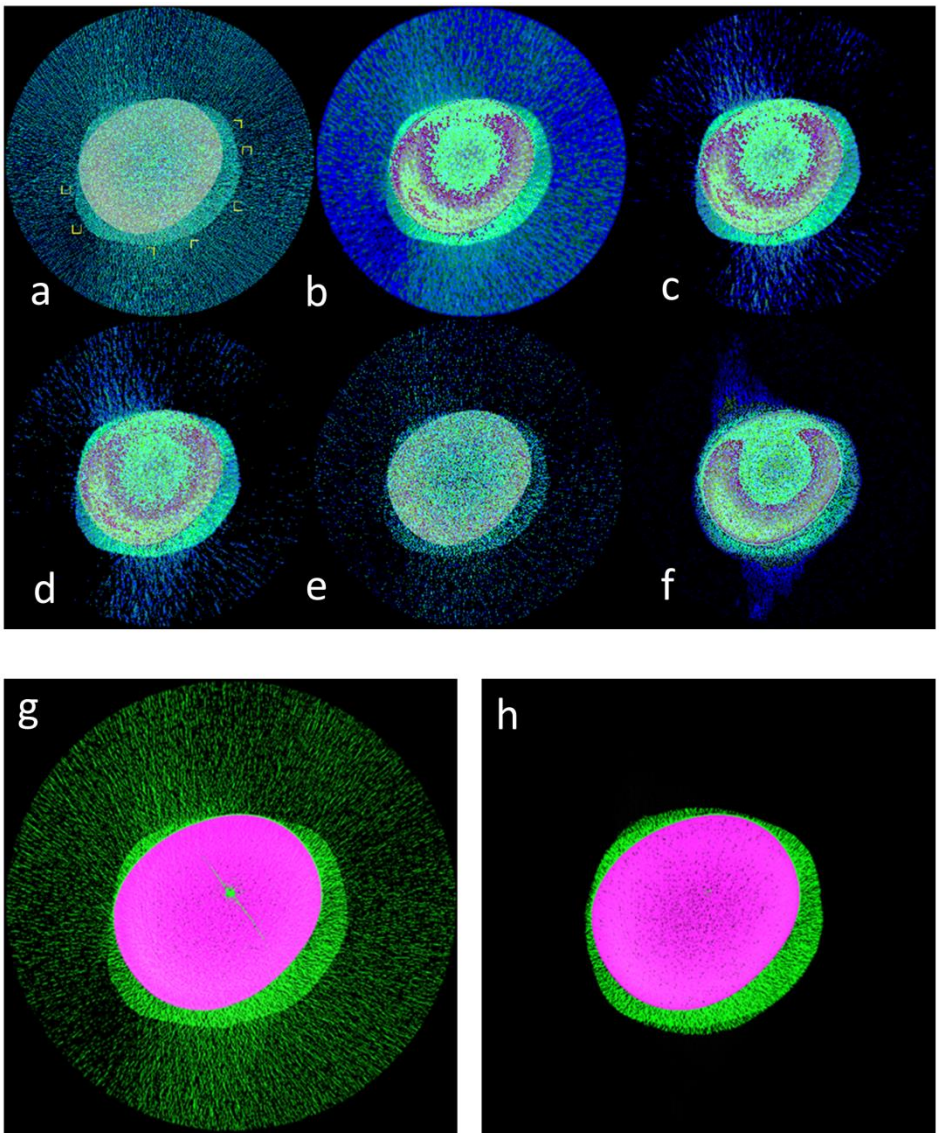

Figure 4.2 Images of a slice from a microCT scan of hydrogel on a tooth, before and after application of various noise reducing filters applied in Fiji (ImageJ). The images have been false coloured to show the noise surrounding the sample. (a) no filter (b) mean filter with radius 10 (c) median filter with radius 10 (d) Gaussian blur filter with radius 10 (e) Minimum filter with radius 1 (f) Removed Outliers filter with radius 50 and threshold 1(g) Dehist segmentation without noise reduction and after noise reduction (h) using the remove outliers filter.

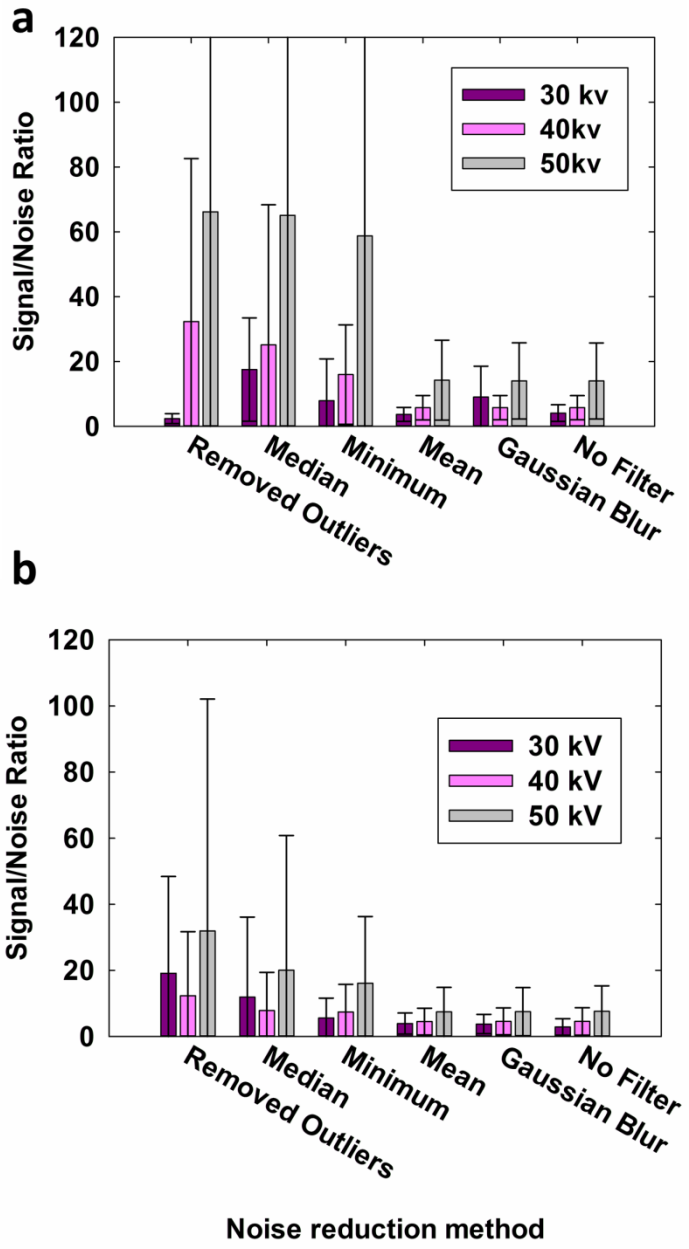

Figure 4.3 Graphs showing signal to noise ratio on 2D reconstruction slices after application of the different noise reduction filters. (a) scan set 1, with less noise (b) scan set 2, with more noise

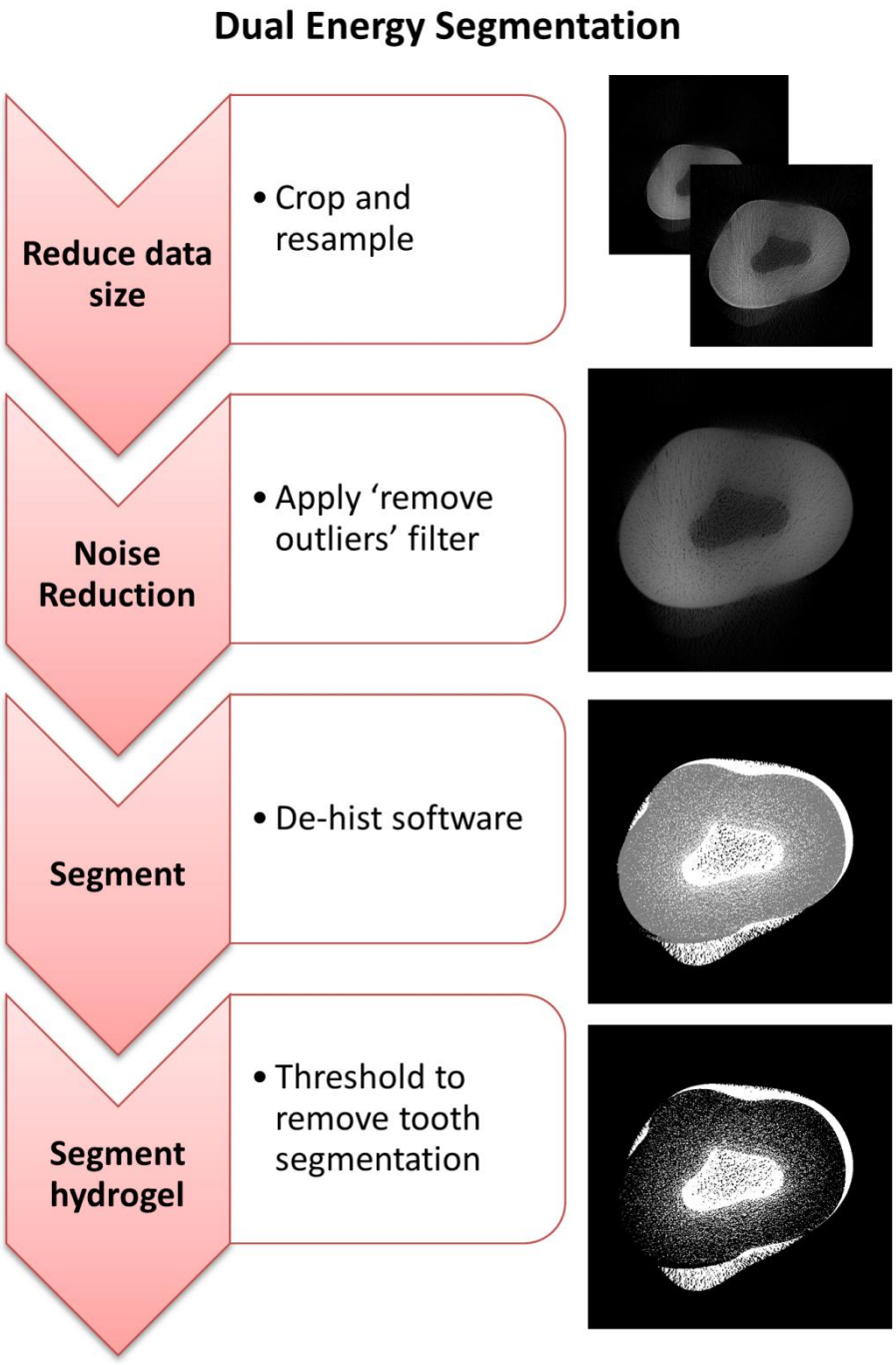

Figure 4.4 Schematic outlining the image analysis steps performed for dual energy segmentation.

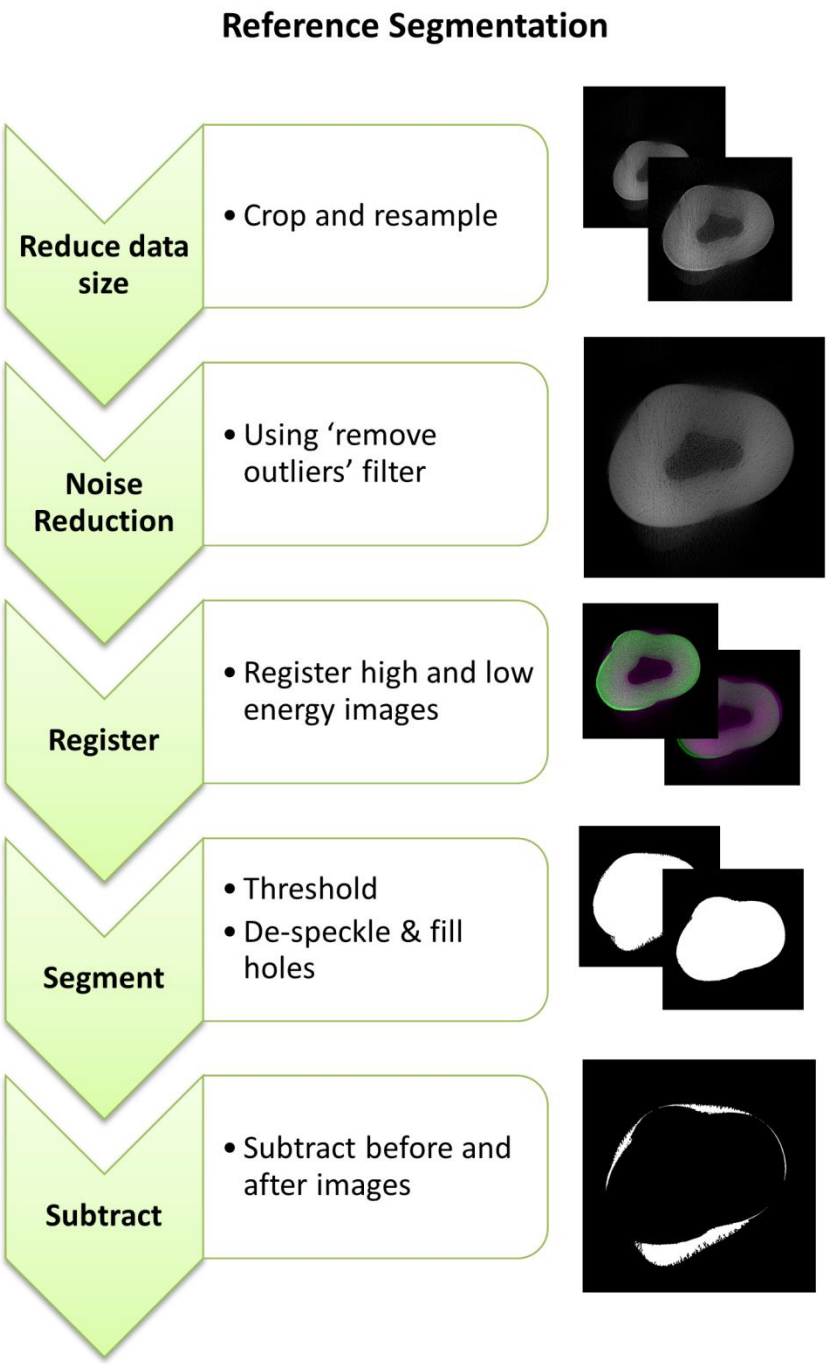

Figure 4.5 Schematic outlining the image analysis steps performed for the reference segmentation which was used to validate the dual energy segmentation method.

4.2.2 Segmentation by Subtraction: Calculating Hydrogel Removal

Gelatine (3 g) (Merck, Whitehouse Station, NJ, USA) and 0.06 g hyaluronan (sodium hyaluronate 95%, Fisher, Waltham, MA, USA) were dissolved in 45 ml RO water at 50^0C to create an unstained hydrogel (Macedo et al, 2014a). The hydrogel was centrifuged at 3000 rpm for 10 minutes to remove air bubbles and stored at 4^oC until use. Before use, the hydrogel was melted in a weighing boat on a hot plate and applied to the crown of the tooth. Six plastic model premolar teeth (Kavo, UK) were used for imaging removal of hydrogel. After application the teeth were stored at -80^0C until microCT imaging within 24h.

The model teeth were imaged in microCT before and after hydrogel removal (SkyScan 1172, Belgium) (n=3). The following settings were used: Source voltage: 33 kV, pixel size: 0.9 µm, source current: 100 µA, rotation step: 0.7º, frame averaging: 2, random movement: 4. Hydrogel was removed with a Satelec P5 Newton ultrasonic scaler with tip 10P (Satelec, Acteon, France), either at medium power (power 10) where cavitation occurred or at low power (power 5) when no cavitation occurred. The scaler was held 1 mm away from the hydrogel for 20 s (Figure 4.6) using a translation stage (PT3, Thorlabs, USA). The model tooth with hydrogel was submerged in water at 4ºC during the removal process.

The image analysis processes for calculating the amount of hydrogel removed are summarized in Figure 4.7.

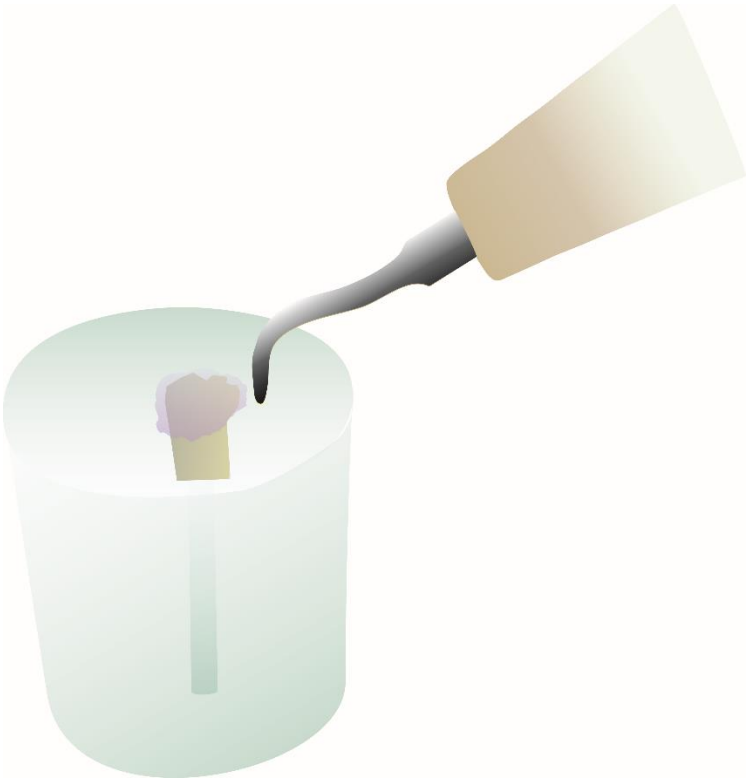

Figure 4.6 Schematic of the experimental setup used for hydrogel removal using an ultrasonic scaler. The tooth and hydrogel were immersed in RO water and the ultrasonic scaler tip was fixed 1 mm away from the hydrogel.

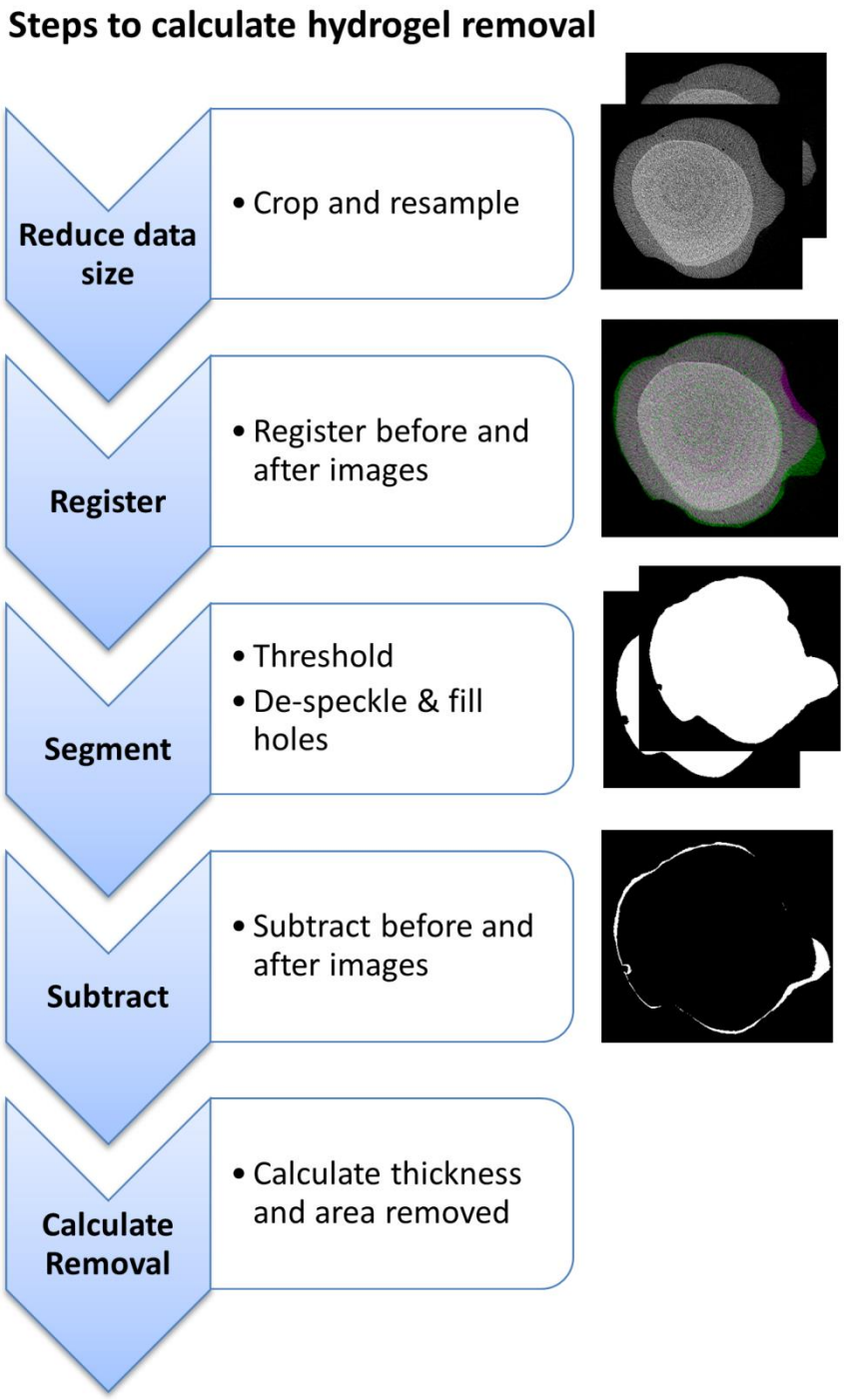

Figure 4.7 Schematic outlining the image analysis steps performed for calculations of hydrogel removal on a plastic tooth model.

MicroCT images were reconstructed with NRecon software using uniform attenuation coefficients. Image analysis was done using Fiji. The before-after scans were first cropped, resampled and co-registered in DataViewer (Bruker, Belgium). Images were registered again for more accuracy in Fiji using the Rigid Registration Plugin with the following settings: n initial positions to try: 1, tolerance: 1, level: 4, stop level: 2.

The registered images were then thresholded automatically using the Li threshold in Fiji, and the fill holes and despeckle functions were applied. The scan taken after hydrogel removal was then subtracted from the scan taken before hydrogel removal to show the amount of hydrogel removed after treatment. The thickness of the hydrogel at each point in the 50 most accurately co-registered slices in each scan was calculated using the BoneJ plugin in Fiji. This is an implementation of the Local Thickness plugin, which calculates thickness by finding the largest spherical diameter which can fit within the structure at each point (Dougherty & Kunzelmann, 2007).

The percentage of hydrogel removed after treatment was calculated from the thresholded before-after images:

$$\%\ hydrogel\ remaining = \frac{thresholded\ image\ area\ after\ removal}{thresholded\ image\ area\ before\ removal} \times 100$$

$$\%\ hydrogel\ removed = 100 - \%\ hydrogel\ remaining$$

4.3 Results

3D volume renderings of the hydrogel on the tooth show the difference between the dual energy hydrogel segmentation and the reference segmentation (Figure 4.8). The dual energy segmentation has falsely segmented the tooth as hydrogel at some points in figure Figure 4.8b.

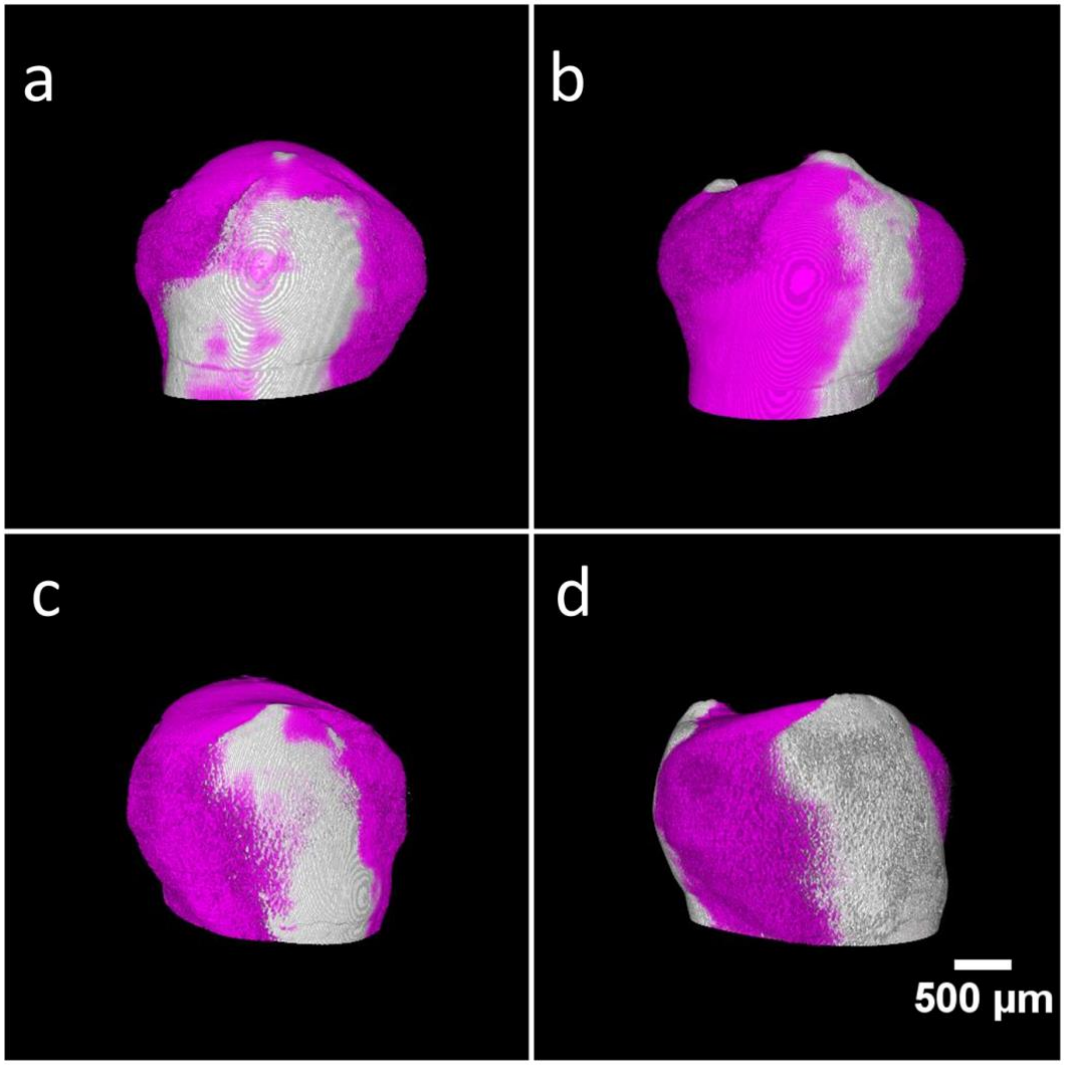

Figure 4.8 3D renderings of the hydrogel on the tooth (a,c) 3D reference segmentations showing the hydrogel in magenta on the tooth. (b,d) corresponding 3D dual energy segmentation using the 40-80 kV energy combination

There was more noise in scan set 2 compared to scan set 1 (Figure 4.3). The sensitivity and specificity values are lower for scan set 2 than scan set 1 (Figure 4.9), showing that the dual energy segmentation is more accurate for scan set 1.The dual histograms for scan set 1 shows two clearly defined regions whereas the dual histograms for scan set 2 show two indistinct regions (Figure 4.9). The 30 kV and 80 kV combination gives the most accurate segmentation but only when the initial noise in the image is low.

The mean and maximum hydrogel thickness removed was approximately equal (Figure 4.10). The hydrogel thickness removed varied at each point along around the tooth (Figure 4.10b). The percentage of hydrogel removed was approximately equal in the case of cavitation and no cavitation (Figure 4.11). An example of the removed hydrogel can be seen in an overlay of one of the registered before and after reconstruction slices (Figure 4.11b).

3D heat map reconstructions show the varying thickness of hydrogel removed around the tooth (Figure 4.12). A larger amount of hydrogel was removed from the occlusal surface compared to the buccal, lingual and interproximal surfaces.

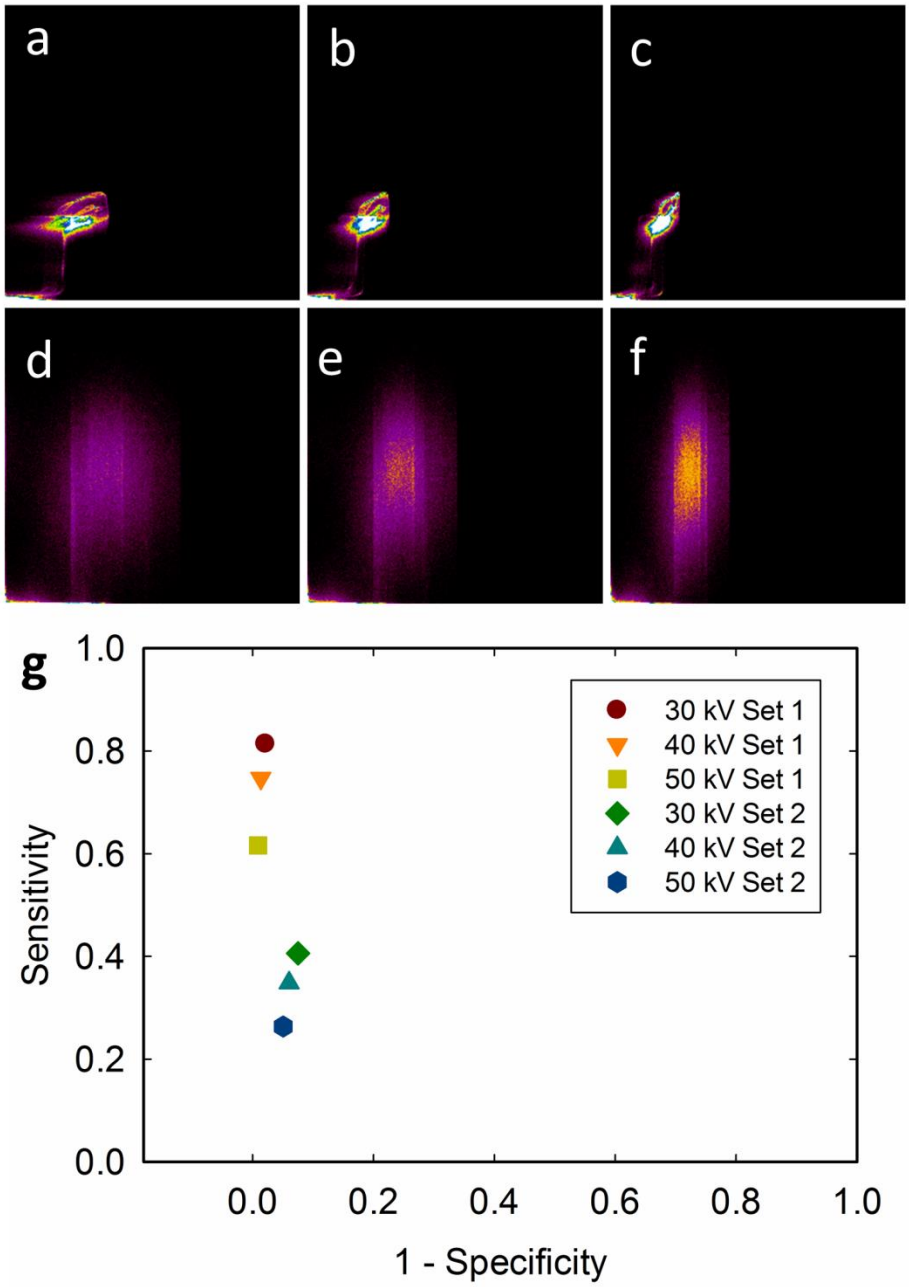

Figure 4.9 (a-c): dual histograms from scan set 1.(d-f) dual histograms from scan set 2.(a,d): dual histogram of images from 30 kV and 80 kV scans (b,e): dual histogram of images from 40 kV and 80 kV scans (c,f): dual histogram of images from 50 kV and 80 kV scans (g) ROC curve showing the accuracy of the different dual energy segmentations for different energy combinations. The low energies used are shown in the legend. The high energy was 80 kV for all cases.

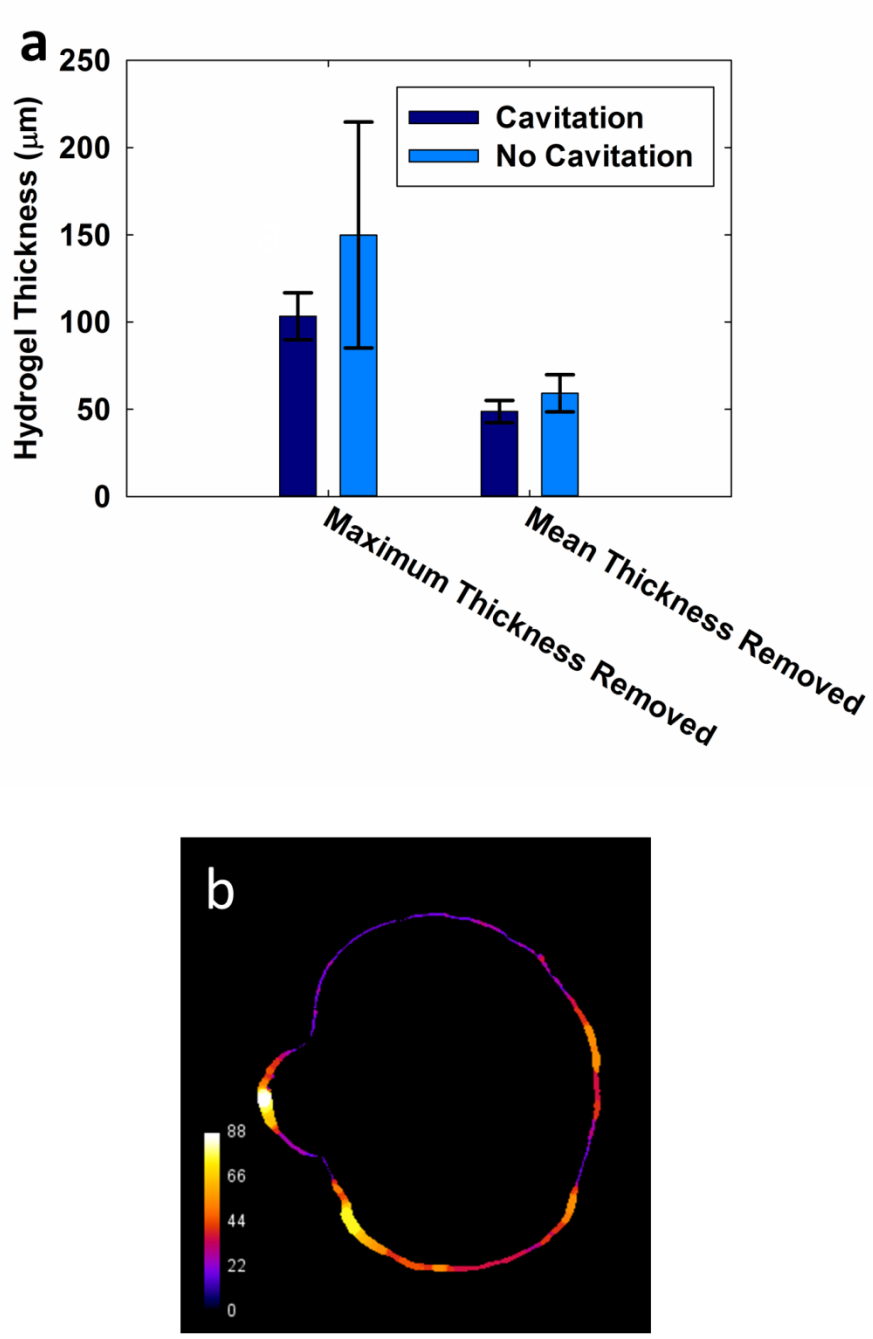

Figure 4.10 (a) Graph showing the mean and maximum thickness of hydrogel removed when cavitation was and was not applied. (b) 2D microCT slice showing a heat map of the amount of hydrogel removed. Calibration bar shows thickness in micrometres

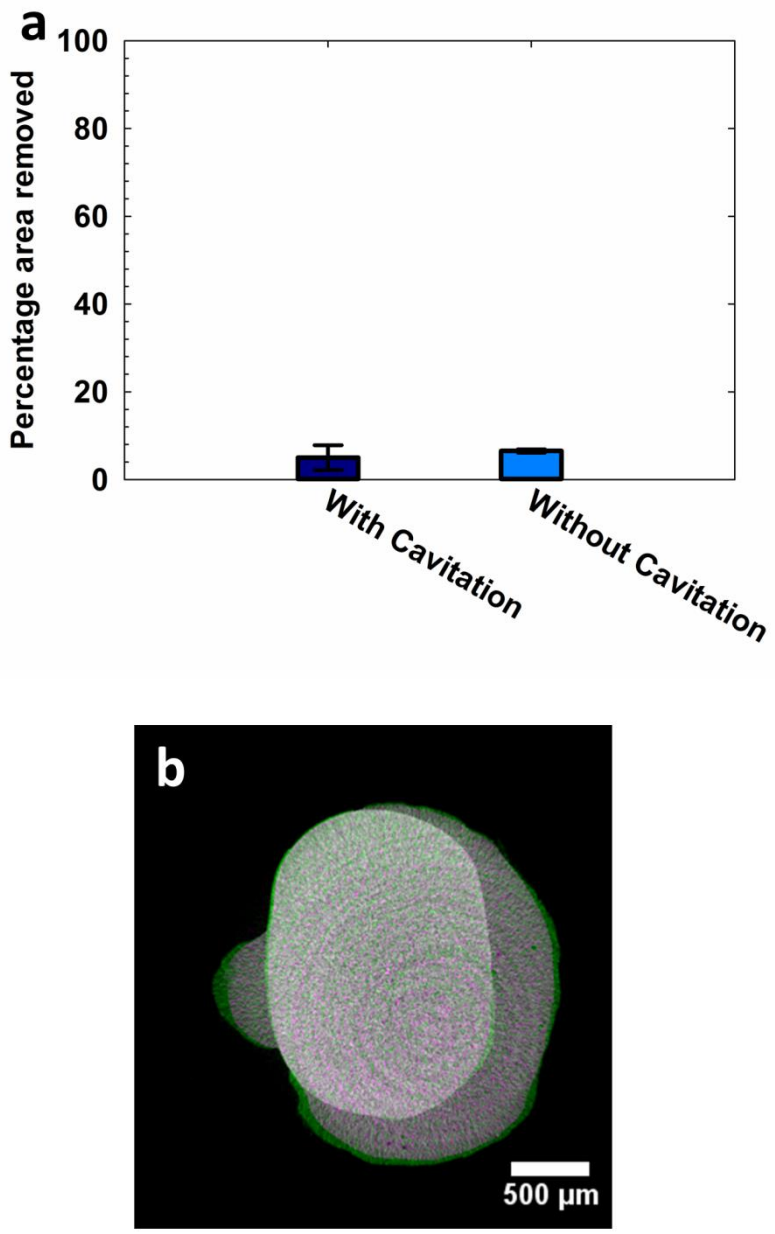

Figure 4.11 (a) Graph of percentage of hydrogel removed after applying the ultrasonic scaler (b) overlay of two reconstruction slices taken before and after removal. The change in hydrogel can be seen in green.

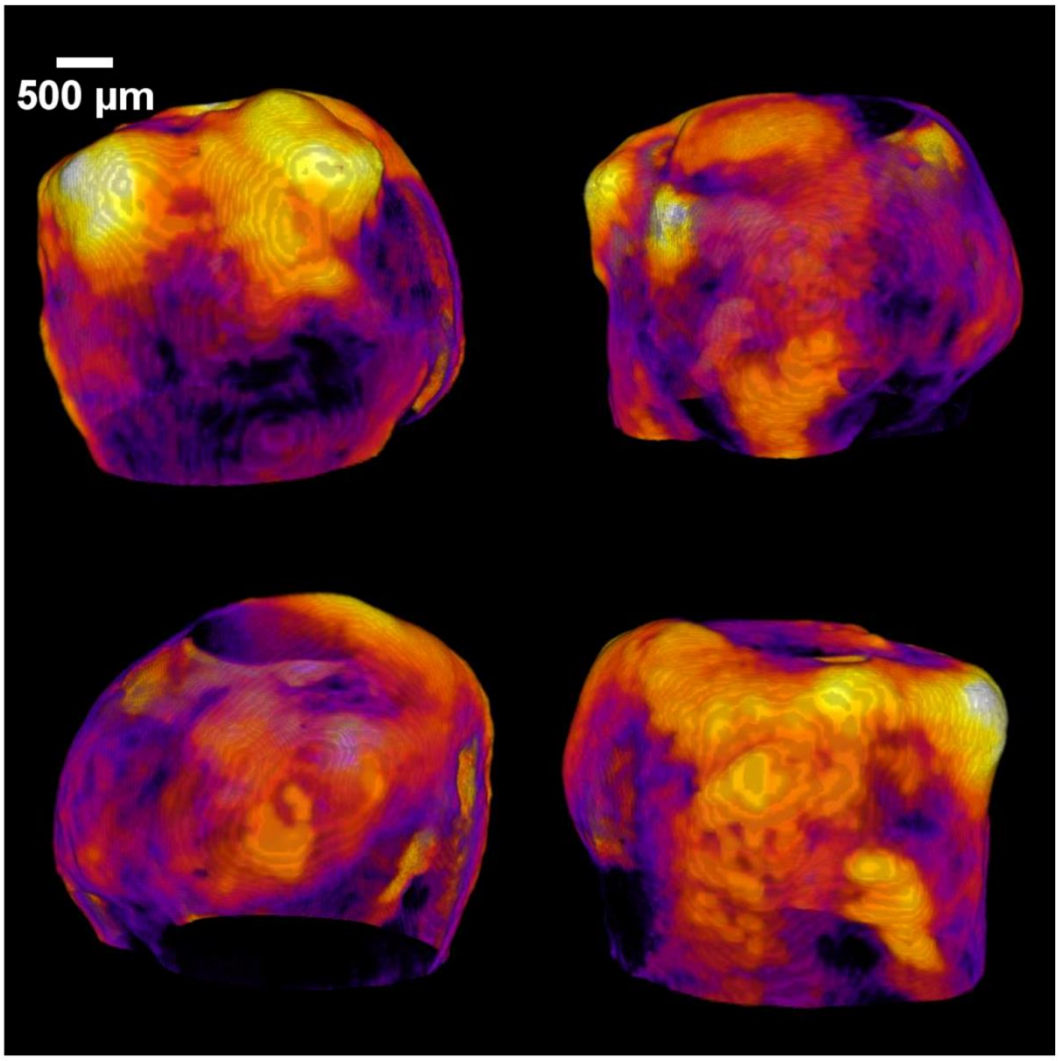

Figure 4.12 Example 3D reconstructions of the removed hydrogel. The heat map indicates hydrogel thickness at each point (light color = thicker hydrogel)

4.4 Discussion

Imaging a hydrogel on a tooth in microCT is difficult due to the different attenuation coefficients of both materials, therefore we investigated if dual energy imaging could be used to image both materials simultaneously. Hydrogel was imaged and segmented from a tooth using dual energy software and the accuracy of the segmentation was evaluated for a range of energy combinations to determine the optimal settings.

The dual energy method has higher sensitivity and specificity when the initial scans have less noise. Two scan sets were tested in this study, one with less noise and one with more ring artifacts and scatter noise to determine how the dual energy segmentation performs on scans with more noise. The segmentation was less accurate on the scan set with more noise (Figure 4.9). The dual histograms for the scan set with more noise are less defined. Therefore the dual energy method will segment better if the original scanning parameters are first optimised to minimise noise. Another reason for the low sensitivity and specificity values is because of sample misalignment as it was repositioned during application of the flat field correction. For future work, the segmentation method could be optimised by adding steps such as image co-registration.

The energy combination of 50 kV and 80 kV had a lower sensitivity than the 30 kV and 80 kV combination, although both had similar specificity values. This suggests that less hydrogel was segmented from the 50 kV images, despite them having a larger signal to noise ratio. This may be because there was increased hydrogel contrast at 30 kV since the Iodine K-edge is at 33.2 keV (Riederer & Mistretta, 1977). The K-edge is the energy at which the K shell of an atom is ejected. Due to this increased x-ray absorption, there is a sudden increase in the attenuation coefficient at the K-edge. Overall, the dual energy method is effective as a rapid method of segmenting

preliminary test scans, but further optimisation is needed if accurate results are required for quantification purposes.

For the second part of the study, a plastic model tooth was chosen for microCT imaging. As this has similar attenuation coefficients to the hydrogel, a single energy scan can be acquired and there is less quantum noise. It was possible to calculate the thickness of hydrogel removed at each point around the tooth, as well as the overall percentage of hydrogel removed after treatment with the ultrasonic scaler (Figure 4.10 & Figure 4.11).

The cavitation from the ultrasonic scaler did not result in more removal of hydrogel compared to applying the scaler without cavitation. The hydrogel may not be a precise representation of dental plaque and was therefore more difficult to remove than biofilm. It is known that less cavitation occurs at medium power than at full power, however medium power was used in this study to keep the conditions more comparable to those used clinically. The cavitation settings and application time can be investigated in further work using the imaging protocol developed in this study.

Approximately 5% of hydrogel was removed in both cases. This removal is likely to have occurred due to hydrogel melting or shrinkage as the viscoelastic properties of the hydrogel change with temperature (Robinson, 2014). As the hydrogel was kept cold to prevent melting during microCT scanning, its properties were different to dental plaque. The hydrogel liquefies at 26°C (Robinson, 2014) whereas the temperature inside the microCT scanner can reach up to 30°C therefore a hydrogel which liquefies above 30°C would be optimal for further research. Different hydrogel compositions were not considered in this study but this can be investigated in future work, for example a dextran hydrogel similar to that used by Rmaile et al. (2014). A mineralised hydrogel

could also be investigated to mimic dental calculus and to aid in contrast enhancement in microCT (Koburger et al, 2013).

It is difficult to compare this work with other research as there are no published studies where a biofilm mimicking hydrogel has been imaged in microCT. Studies have however attempted to image and segment real biofilm using microCT (Davit et al, 2011; Iltis et al, 2011; Santini et al, 2015). Davit et al applied a lookup table in ImageJ to pseudo-colour the biofilm and background (Davit et al, 2011). They stated however that this was only for visualisation purposes and quantification was not attempted in the study as the segmentation method was not accurate. Iltis et al investigated the use of synchrotron based microCT to image biofilm in a flow cell (Iltis, 2013; Iltis et al, 2011). A 'Point Wrap' algorithm was used to segment the biofilm. They compared segmentation in part of a 2D reconstruction slice with the same area segmented from a light microscopy image. Although the error between the two features was 4%, only one part of a reconstruction slice from the entire image stack was evaulated. The segmentation efficiency for the whole stack of images was not calculated, therefore it is unclear how well it performs overall. In contrast, in this study we have calculated sensitivity and specificity values over the whole 3D image stack of 490 images, giving more understanding of the segmentation accuracy. Santini et al. imaged a mineralised biofilm on a 3D object in microCT (2015) but the segmentation method was not specified. No previous studies have measured biofilm thickness from microCT images. Therefore it would be useful to further develop the methods established in this study and apply them to image and quantify real biofilm in situ in 3D.

The dual energy method can be compared with the segmentation by subtraction method to determine if it is a valid method of analysis. However the method of segmentation by

subtraction could also contain errors such as from inaccurate co-registration. The accuracy of this has not been evaluated in this study but it could be compared to manual co-registration in future work.

4.5 Conclusion

The purpose of the current study was to determine whether artificial biofilm can be imaged on a tooth in microCT and if it can be used to calculate removal in 3D. There were minimal noise artifacts when imaging a plastic tooth model therefore it was possible to quantify removal of hydrogel in 3D from microCT images. Although this is preliminary work and further research is needed to optimise the methods, the imaging and analysis protocols developed in this study can be useful for future work and are relevant to biofilm removal research in Dentistry and in other fields such as Biomedical and Environmental Engineering.

However, these results may not be applicable to all situations and the imaging and analysis procedures may need to be altered due to differences in microCT instruments and sample x-ray attenuation coefficients. A second limitation is the imperfect co-registration which needs to be improved for more accurate measurements of hydrogel removal. Although these findings should be interpreted with caution, this study has several strengths, such as the ability to combine images of samples with very different attenuation coefficients and also the development of a method to calculate the thickness of artificial biofilm removed from a complex structure at any point.

The protocol can be used to test the effect of various periodontal therapy methods in 3D, and can aid in the development of more efficient instrumentation for biofilm

removal. The dual energy method can be applied to other studies such as imaging connective tissue interfaces.

This chapter provided a method of 3D biofilm quantification. Although it is useful to evaluate where the most and least biofilm removal occurs on different structures, it is also important to visualise biofilm at a higher resolution to study its disruption from a surface. The next chapter considers removal of real biofilm from dental implant surfaces and quantification from scanning electron microscopy images.

5. AN SEM AND IMAGE ANALYSIS STUDY OF ULTRASONIC BIOFILM REMOVAL FROM TITANIUM SURFACES

5.1 Introduction

The surfaces of dental implants are routinely roughened to promote early osseointegration with the surrounding bone (Le Guéhennec et al, 2007). However, increasing the surface roughness increases the surface area and consequently exacerbates biofilm formation as the bacteria have more sites for attachment. In peri-implantitis, bone loss can lead to the exposure of the roughened surfaces of the implant threads to the oral environment, enabling biofilm to form which will further potentiate bone loss (Rosen et al, 2013).

Current mechanical instruments for implant surface debridement (e.g. metallic and non-metallic curettes, rotating titanium brushes) have been shown to be ineffective at removing sufficient biofilm (John et al, 2014; Lin et al, 2013). In addition, implant surface instrumentation may damage the titanium surface (e.g. ultrasonic scalers with

metal tips) or may leave residue following air-abrasive powder systems or the use of plastic tips on the implant (Fox et al, 1990; Kawashima et al, 2007; Koh et al, 2013; Lea & Walmsley, 2009; Louropoulou et al, 2014; Mann et al, 2012; Park et al, 2013). Surface damage to the implant can make it more susceptible to biofilm colonisation or can disturb the biological seal between the implant and soft tissue (Baek et al, 2012; Kawashima et al, 2007).

Biofilm formation on other implantable medical devices such as catheters, heart valves and orthopedic implants is also an issue (Costerton et al, 1987; Ramage et al, 2006). As a consequence, considerable research effort is currently being spent developing methods and instrumentation to remove biofilms from dental implants and other biomaterial surfaces.

The cavitation from ultrasonic scalers may be able to disrupt biofilm without modifying the implant surface. The aims of this study were therefore to develop novel quantitative methods to assess the effectiveness of mechanical biofilm disruption on Ti dental implant surfaces.

A current deficiency in the research effort is the inability to quickly and objectively evaluate the efficiency of biofilm disruption with a high level of accuracy. Rapid analysis methods are required to optimise the experimental process. Many different methods have been used to assess biofilm removal efficiency. Biological approaches include semi-quantitative staining, measurements of dried biomass, protein or DNA quantification, or assessments of residual viable organisms through standard microbial culture techniques (Hadi et al, 2010; John et al, 2014; Kite et al, 2004; Park et al, 2013; Qian et al, 1996). Each method has advantages and deficiencies but they all provide

only indirect values of the removal efficiency and are prone to operator induced variability.

In contrast, direct imaging of the biofilm provides information on its structural characteristics, its interaction with the surface, as well as spatial information regarding the homogeneity of biofilm disruption. Confocal laser microscopy, electron microscopy, light microscopy, bioluminescence imaging and macroscale photography have all been used as measurements to assess biofilm disruption (Agarwal et al, 2014; Clegg et al, 2006; Cruz et al, 2011; Fricke et al, 2012; Hägi et al, 2015; Li et al, 2012; Nance et al, 2013; Salles et al, 2007; Schwarz et al, 2006; Sedgley et al, 2004; Tawakoli et al, 2015; Vickery et al, 2004; Whittaker et al, 1984; Wu et al, 2011; Zhang & Hu, 2013). Frequently however, such techniques are only used qualitatively or semi-quantitatively leading to a high risk of bias in the investigation. When quantitative measurements are made, information such as biofilm area/volume and thickness can be acquired to establish the effectiveness of the intervention (Nance et al, 2013; Zhang & Hu, 2013). Image segmentation has been used to calculate the area of the surface covered by biofilm. One common approach is simple thresholding, which is effective when there are differences in the pixel intensity value between biofilm and background. Many studies investigating biofilm removal have used thresholding to segment images of biofilm from photographs and light microscopy images, however typically manual thresholding has been employed (Fricke et al, 2012; Murphy et al, 2015; Vickery et al, 2004), which is subjective leading to large errors and making intra-operator reproducibility impossible. Others studies using automatic thresholding have failed to specify the exact method of segmentation or validate its accuracy (Cruz et al, 2011; Salles et al, 2007; Schwarz et al, 2006). Moreover, the imaging techniques used in

these studies for calculating such data (light microscopy, confocal microscopy and photography) do not give sufficient resolution to image individual bacteria in biofilms. Therefore a gap exists to develop a methodology that can consistently, accurately and objectively segment biofilm from images to quantify biofilm disruption.

Scanning electron microscopy (SEM) has been used extensively for qualitative observation of biofilm disruption due to its high resolution and is usually applied in combination with biological assays of biofilm removal efficiency (Clegg et al, 2006; Hägi et al, 2015; Li et al, 2012; Schwarz et al, 2006; Vickery et al, 2004; Whittaker et al, 1984). Using SEM images, simple thresholding often cannot be implemented as the intensity values of the biofilm and normal surface are similar due to the same effective contrast seen by SEM. Rough (textured) biomaterial surfaces such as those found on components intended for osseo-integration further complicate the image analysis, so advanced segmentation methods such as semi-supervised machine learning techniques are typically required (Chan et al, 2006).

The overall objective of the study is to develop a work-flow for SEM imaging and quantitative image analysis of biofilm samples before and after mechanical disruption that can be applied to complex surface topologies for a wide variety of biomaterial applications. An imaging and image analysis protocol is presented for calculating the area of biofilm on Ti surfaces from SEM images, before and after application of cavitation from an ultrasonic scaler. This is used to calculate the area of biofilm removed after treatment.

5.2 Materials and Methods

5.2.1 Preparation of the Biomedical Ti Substrate

The following protocol from Yu et al. was used to replicate dental 'SLA' (Sandblasted, Large-grit, Acid-etched) implant surfaces (2015): 16 commercially pure ASTM Grade II Ti discs of 14 mm diameter and 1 mm thickness (Titanium Products Ltd, Birmingham, UK) were polished manually (DAP-7, Struers, Ballerup, Denmark) using P500 SiC paper and then sandblasted with 250 µm corundum particles (Korox, BEGO) (SANDIMAT, Local exhaust ventilation, Allianz Engineering Inspection Service Ltd, Italy). Discs were then cleaned in distilled water (dH_2O) for 15 mins in an ultrasonic bath, and etched in 37% HCl/ 98% H_2SO_4 (1:1) at 80 °C for 5 mins. A further 16 Ti discs were polished to a high surface finish to mimic the surface generated at the superficial 'collar' region of dental implants using sequentially increasing grades of SiC abrasive papers from P500-P2000 for standardised time periods using RO water as the lubricant. The prepared discs were then sequentially cleaned in acetone, ethanol and RO water in an ultrasonic bath for 15 mins each and subsequently sterilised by autoclaving at 121 °C for 1 h.

5.2.2 Bacterial Cell Culture and Biofilm Generation

The Gram-positive bacteria *Streptococcus mutans* (strain 3209) was used in the current study to form a simplistic early biofilm model for the development of the image analysis techniques. Briefly, the stock microorganisms were recovered from porous storage beads maintained at -20 °C and initially grown on the Tryptone Soya Agar (Oxoid, UK) media for 24 h. The *S mutans* culture was transferred to a sealed CDC biofilm reactor Model CBR 90-3-DH-int (Biosurface Technologies Corp, Montana, USA) into which the Ti discs were suspended vertically in a bespoke holder with

Tryptone Soya Broth (Oxoid, UK containing 25 % Sucrose (Sigma Aldrich, USA)) as the media. After 24 h in batch mode the fed batch (continuous flow) of incubation was then commenced by turning on a peristaltic pump for 96 h. Agitation of the culture media was maintained throughout using a magnetic stirrer at 100 rpm. The Ti discs were removed from the biofilm reactor after a total of 5 days of incubation and then fixed in 0.1M sodium cacodylate buffer and 2.5% glutaraldehyde (25 % EM grade, Agar Scientific, Essex, UK), dehydrated using serial ethanol gradient immersions and then gold sputter-coated (Emitech K550X, Kent, UK) for SEM as previously described (Macaskie et al, 2005). Copper SEM finder grids (Agar Scientific, UK) of 10 mm diameter and a mesh size 450 x 450 μm were attached to the discs to aid in locating the same areas before and after biofilm removal (Figure 5.1).

5.2.3 Biofilm Removal

Biofilm was removed with a an ultrasonic scaler (Satelec P5 Newtron, Acteon, France). The tip was immersed in RO water with the water flow from the scaler turned off (Figure 5.1). The following setting combinations were used: power 5 or 10 (corresponding to low and medium power); held 0.5 mm or 1 mm away from disc; scaler operated for 30 s or 60 s. The removal process was also imaged with a high speed camera (HPV-1, Shimadzu Corporation, Japan) at 128,000 fps to visualise cavitation.

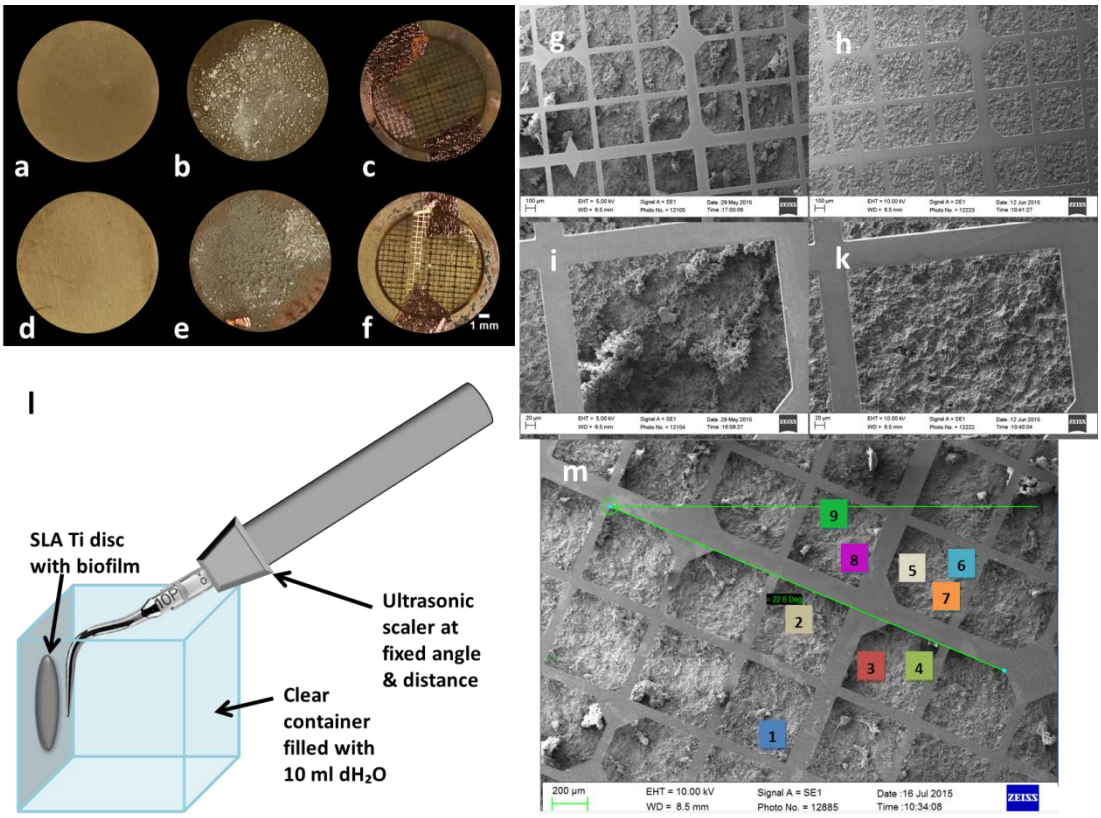

Figure 5.1 Photographs of the discs: (a) after sand blasting and acid etching. (d) after polishing. (b,e) after biofilm growth (e,f) after applying the SEM finder grid for imaging. (g-k) SEM images showing how the finder grids were used to locate the same area before (g,i) and after (h,k) removal. (l) Schematic showing experimental setup for biofilm removal experiments. (m) example of marking an angle and locations of measurements on the SEM image for relocating the same area after removal experiments

5.2.4 SEM Imaging

A Zeiss EVO MA-10 scanning electron microscope was used for imaging. Ti discs were placed into the SEM sample holder at the same orientation before and after removal so the same area could be identified and standardised. Imaging was performed at x100, x500 and x1250 magnifications at a working distance of 5-8 mm to aid in locating the same area after biofilm removal. Images taken at x1250 magnification were used for analysis (Figure 5.1). Biofilm was imaged in areas where the Ti surface was also visible before removal, so features in the surface could be used as markers for accurate co-registration.

5.2.5 Image Analysis

All image analysis was performed using Fiji (distribution of the ImageJ software, U. S. National Institutes of Health, Bethesda, Maryland, USA) according to the following methods (Schindelin et al, 2012). The pixel size of SEM images used in the analysis was 250 nm.

5.2.5.1 Image Registration

SEM images of biofilm taken in similar locations on the Ti discs before and after removal were firstly co-registered (aligned) so the same area was observed in both images. Registration used the 'Register virtual stack slices' plugin (Arganda-Carreras et al, 2006), with a rigid feature extraction model and a rigid (translate & rotate) registration model. The shrinkage constrain option was employed so a reference image did not need to be chosen. The maximal alignment error of the geometric consensus filter was set to 8 pixels for more precise registration, and the default settings were used for the feature descriptor and scale invariant interest point detector. Images were then cropped to the same size to enable batch processing in the segmentation step and

ensured that blank pixels (due to the image being translated and rotated during the registration procedure) were removed.

5.2.5.2 Pre-processing for SLA Surface Images

Different pre-processing steps were conducted according to the surface topology (rough SLA surface and the polished surface) to enable more accurate segmentation. For images of biofilm on the SLA surface, a rolling ball background subtraction was applied (1000 rolling ball radius, sliding paraboloid) to correct for uneven illumination, which occurred due to the rough texture of the surface which had microscale pits due to the exposed grain boundaries resulting from acid etching. The contrast was enhanced by 1% and the Remove Outliers filter was applied using a threshold of 50 and radius of 2 to remove any bright pixels on the SLA surface for easier segmentation. This filter replaced any pixels greater than 50 with the median value of the surrounding area (circle of radius 2). The gamma operation was applied with value 0.6 for non-linear histogram adjustment before sharpening the images to obtain improved contrast between individual bacteria and the surface.

5.2.5.3 Pre-processing for Polished Surface Images

For images of biofilm on the polished surface, contrast was enhanced by 0.4% and the Remove Outliers filter was applied with a threshold of 0 and a radius of 2, so that all pixels were replaced by the median of the surrounding area (circle of radius 2). This 'smoothed' the scratches in the surface so they would not be misinterpreted as biofilm in the segmentation step.

5.2.5.4 Segmentation

The biofilm was segmented from the surface using the Trainable Weka Segmentation plugin (Arganda-Carreras et al, 2013, Accessed 07.09.2016) which utilises a collection

of machine learning algorithms for segmentation. Specifically, this algorithm computes features from the input image using edge detectors, texture filters, noise reduction filters and membrane filters to create feature vectors, which are then applied to the learning algorithm. Pixel samples are provided by the user, and a classifier is trained using these samples in a semi-supervised way. The trained classifier can then be applied to segment the rest of the image(s) automatically. The default classifier (Fast Random Forest) was used for all analysis in this study.

The pixel samples chosen by the user for training can be free-drawn, for example with the lasso tool in Fiji, but to ensure consistency and reproducibility a set of square regions of interest measuring 12x12 pixels were used. This size was optimal as it was large enough to provide enough pixel values for training and small enough to fit over small clusters of biofilm and individual bacteria. Around 10 to 20 regions of interest (ROIs) were placed on the image by the user and put into one of two classes - biofilm or surface. If needed, the ROIs were repositioned by the user to retrain the classifier for improved segmentation. The following training features were chosen to create a classifier for the majority of images: Gaussian blur, Sobel filter, Hessian, Difference of Gaussians, Membrane projections, Variance, Mean, Minimum, Maximum, Median and Bilateral, as this combination gave the most effective segmentation in the least amount of time (approximate computation time: 10 s per image). All of the training features available were chosen for segmenting the SLA images with less bacteria as they were more difficult to segment (approximate computation time: 120 s per image) (in addition to the features mentioned above, the following were also used: Anisotropic diffusion, bilateral, Lipschitz, Kuwahara, Gabor, Derivatives, Laplacian, Structure, Entropy,

Neighbours). Other settings were kept as default (membrane thickness 1, membrane patch size 19, minimum sigma 1.0, and maximum sigma 16.0).

For certain images, batch processing was possible so a classifier only needed to be trained once and could then be applied to the rest of the images to automatically segment them. This could be done for all of the images of the polished discs - in this case two classifiers were trained, one for images with more than half of the surface covered by bacteria and secondly for images with less than half the surface covered by bacteria. Two separate classifiers were required for this because the images with more biofilm had different features to the images where more titanium was visible.

Batch processing was possible for some images of biofilm on the SLA surface - two classifiers were again trained as before, and any images which could not be segmented by these classifiers were segmented separately (e.g. if there was surface charging in SEM resulting in artefacts), with a separate classifier being trained for each image. In some cases, images needed further brightness and contrast adjustments for accurate segmentation.

5.2.5.5 Post-processing

Objects smaller than 20 pixels were assumed to be noise and were removed from the segmented images using the 'Analyse Particles' plugin. The binary images were inverted if necessary so the surface was black and the biofilm areas were white. The histogram of each image was calculated to find the number of white pixels, corresponding to the biofilm area. The percentage of biofilm remaining on the surface after instrumentation was calculated (Equation 3):

$$biofilm\ remaining = \frac{biofilm\ area\ after\ removal}{biofilm\ area\ before\ removal} \times 100 \qquad [3]$$

5.2.6 Statistical Analysis

The Mann-Whitney Rank Sum Test was used for testing the statistical significance, with significance defined as $\alpha=0.05$. SigmaPlot 12.3 (Systat Software, USA) and MATLAB (The Mathworks Inc, USA) were used for analysis and data plotting. The accuracy of the segmentations was evaluated by comparing to a manual segmentation done by the user, for one pair of images for each setting measured (16 pairs of images in total), and calculating the sensitivity and specificity using a custom written MATLAB script (For code see Appendix, Chapter 9). The regions of interest chosen by the operator for training the classifier were randomly selected. To test the reproducibility of this method, a classifier was trained 6 times on one image where 10-20 sample ROIs were placed in different locations each time, resulting in 6 segmented images. These were compared to a reference image segmented with a classifier trained with 40 sample ROIs, and sensitivity and specificity were calculated.

5.3 Results

SEM images of the two surfaces prepared on the Ti test specimens are shown in Figure 5.2. Culture of *S mutans* on Ti surfaces under biofilm conditions resulted in typically heterogeneous distributions of biofilm with greater growth observed on roughened 'SLA' surfaces. Figure 5.3 demonstrates the developed methodology to segment biofilm from the Ti surface in SEM images using an automatic machine learning process. Figure 5.4 demonstrates the use of the Trainable Weka Segmentation plugin whereby baseline user classification of the surface and of the biofilm trains the programme to subsequently segment the image (Arganda-Carreras et al, 2013, Accessed 07.09.2016).

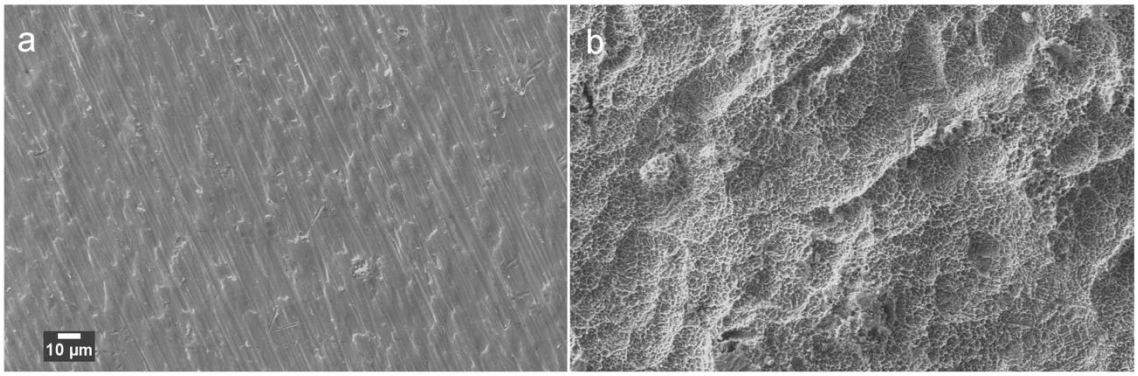

Figure 5.2 SEM images of the clean surfaces produced in the study, imaged before biofilm colonisation. (a) Polished surface (b) SLA surface

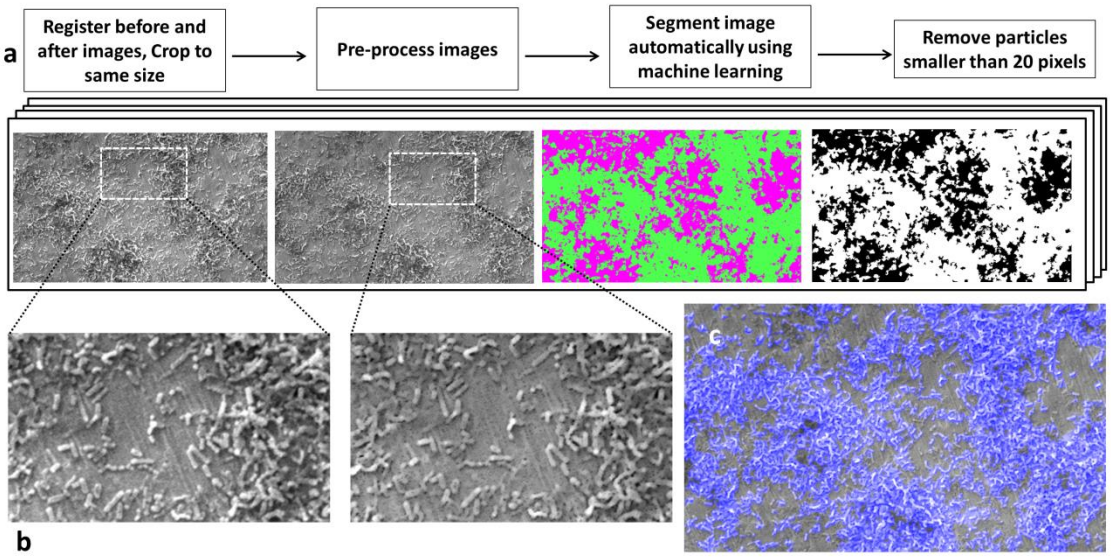

Figure 5.3 (a) Method developed to segment biofilm from the surface in SEM images. (b) close-up showing image before and after pre-processing – outliers were removed to smooth scratches on the surface, for better segmentation. (c) Overlay of the segmented area (blue) on the SEM image, showing accurate detection of biofilm.

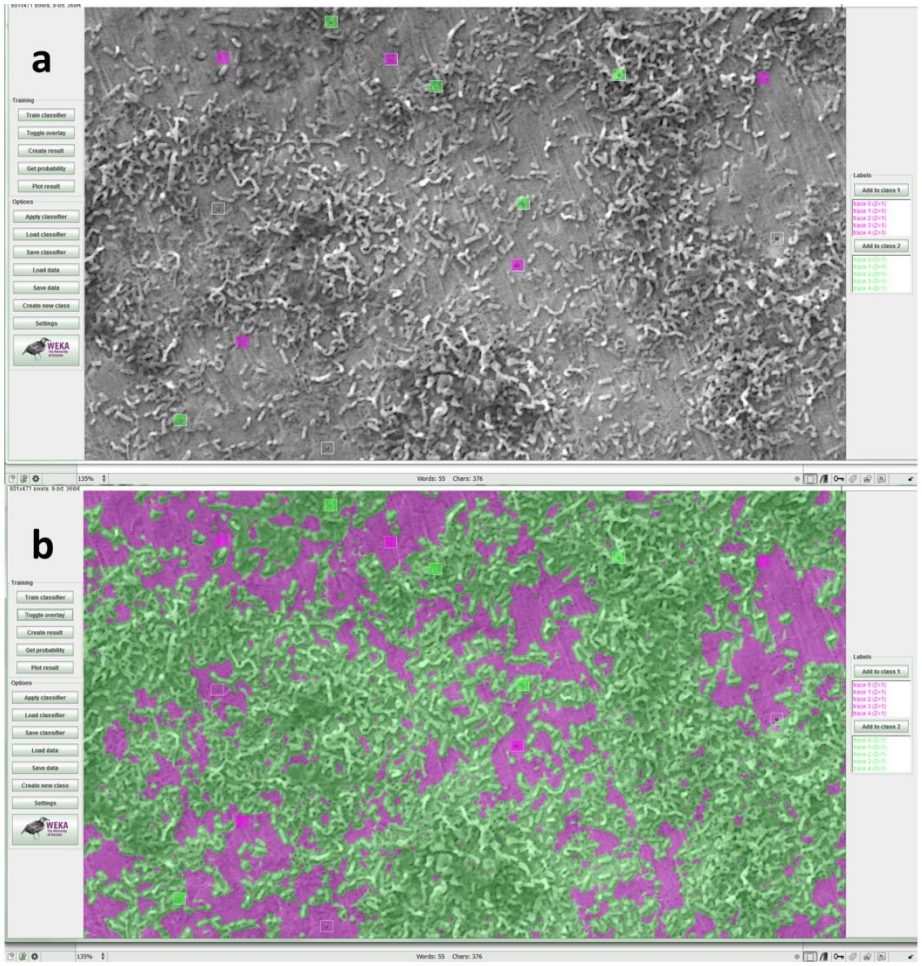

Figure 5.4 Screenshots of the Trainable Weka Segmentation plugin in Fiji(Arganda-Carreras et al, 2013, Accessed 07.09.2016). (a) Square regions of interest were classified by the user as samples to train the program to segment the rest of the image, where biofilm is labelled green and the surface is labelled magenta. (b) Whole image segmented automatically from the samples given in (a). The Weka logo http://www. cs. waikato. ac. nz/ml/images/Weka (software) logo. png> is available under the Creative Commons Attribution-ShareAlike 2.5 http://creativecommons. org/licenses/by-sa/2.5/ License (http://creativecommons. org/licenses/by-sa/2.5/)" for the use of the logo in this figure. Please see the terms of use on the Weka website for more information: http://www. cs. waikato. ac. nz/ml/weka/citing. html

The sensitivity and specificity of automatic segmentation were calculated by comparison with manual segmentation (manually delineating all bacteria in the image) for both types of surface topology. The mean sensitivity and specificity for segmentation of the polished surface images were 0.74±0.13 and 0.88±0.09 respectively (Figure 5.5). The mean sensitivity and specificity values for segmentation of the SLA surface images were 0.80±0.18 and 0.62±0.20 respectively. The receiver operating characteristics curve in Figure 5.5 demonstrates the accuracy of segmentation of different images and outlying data was noted only when very few bacteria were present in the image field. ROIs were randomly placed on either the surface or the biofilm in the SEM images by the operator when training the algorithm. The reproducibility of this selection method was tested to determine whether the placement of the ROIs had an effect on the outcome of the segmentation. The mean sensitivity and mean specificity were calculated as 0.93±0.01 and 0.89±0.04, respectively (Figure 5.6).

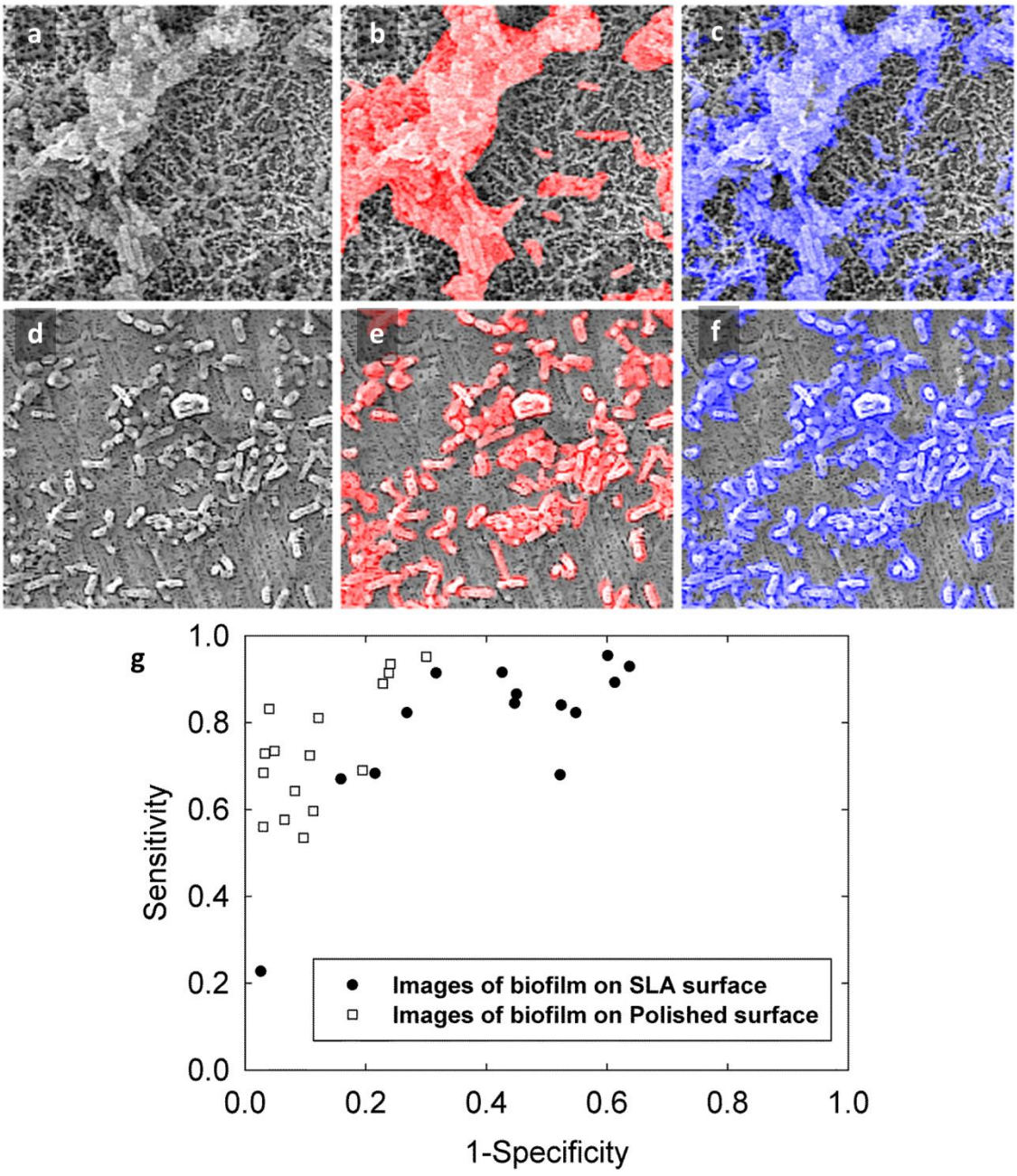

Figure 5.5 Examples of comparing the automatic segmentation to a manual reference segmentation. (a) SLA surface with biofilm growth. (b) Overlay in red showing the manual segmentation. (c) Overlay in blue showing the automatic segmentation. (d) Polished surface with biofilm growth. (e) Overlay with manual and (f) automatic segmentation. (g) Receiver Operating Characteristics plot showing accuracy of segmentation for different images.

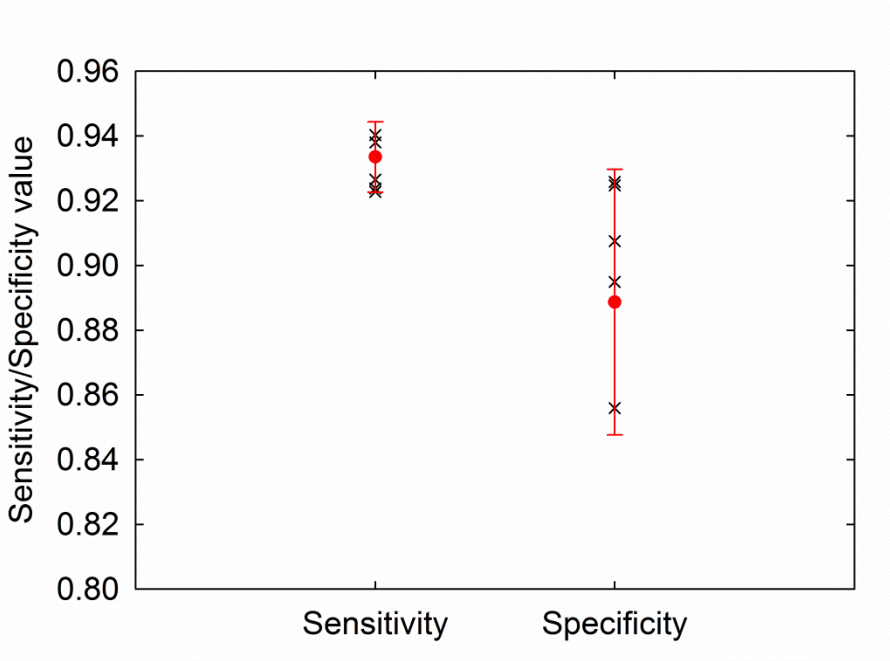

Figure 5.6 Sensitivity and specificity values obtained when testing the reproducibility of the initial sample pixel choice. All values are over 0.8, which shows that the method of choosing sample pixels is reproducible.

More biofilm was disrupted when the scaler was used at higher power for a longer duration. There was a statistically significant difference between the amounts of biofilm removed at power 5 and power 10 for all except 1 condition. More biofilm was removed when the scaler was used at medium power compared to low power (Figure 5.7, Figure 5.8). There were also statistically significant differences in the amount of biofilm removed when the scaler was operated for 30 s and 60 s for the following settings: distance 0.5 mm, power 10, SLA discs ($p=0.021$), and distance 1 mm, power 10, polished discs ($p<0.001$). In these cases more biofilm was removed after operating the scaler for 60 s (Figure 5.9).

Cavitation bubbles were observed continuously around the scaler tip at medium power, but rarely at low power (Figure 5.10). At 0.5 mm from the disc, cavitation clouds originating from the scaler tip impacted onto the surface, but not at 1 mm. Cavitation bubbles were also observed on the surface of the disc at both distances.

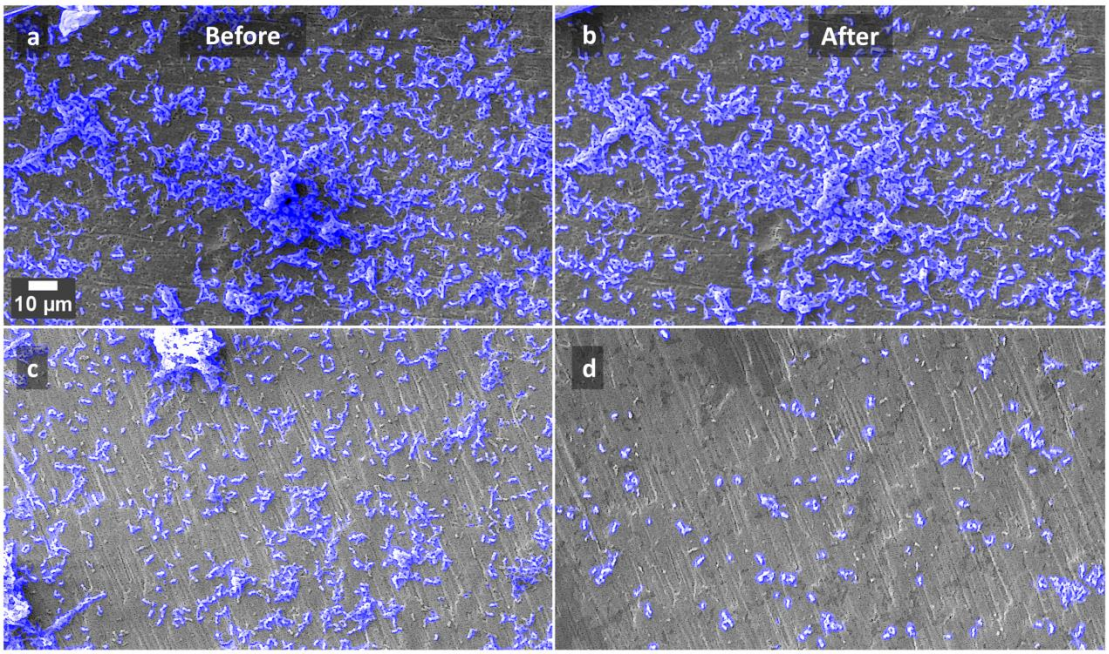

Figure 5.7 Examples of SEM images of the polished discs, before and after treatment with the ultrasonic scaler held 1 mm away for 30 s, at low power (a,b) and medium power (c,d). The blue overlay shows the automatic detection of bacteria.

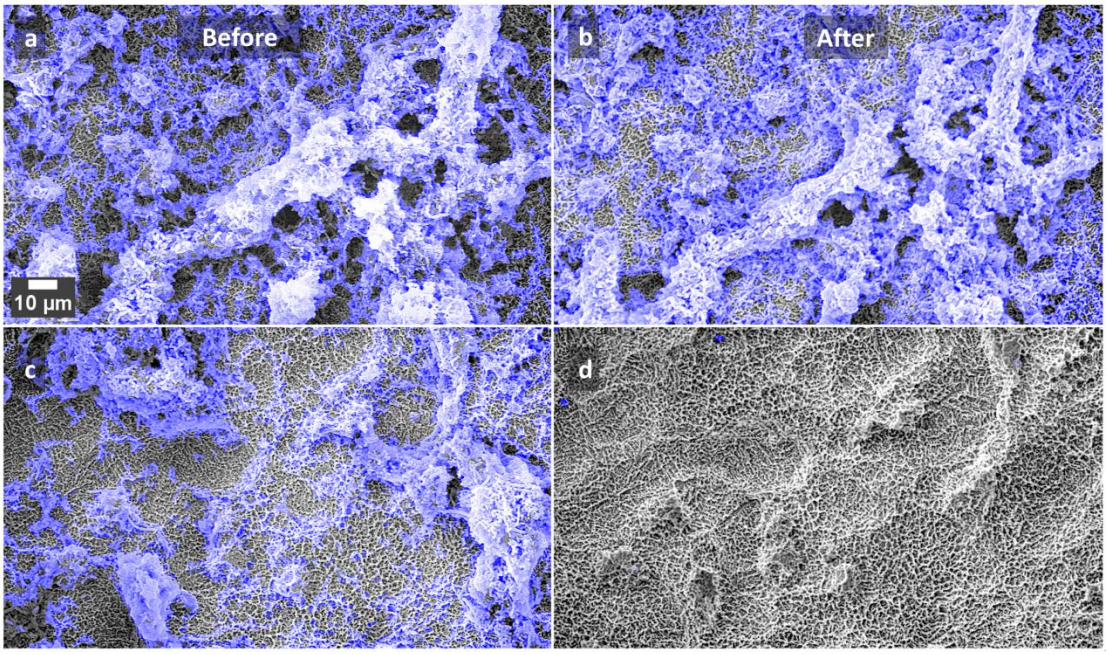

Figure 5.8 Examples of SEM images of the SLA discs, before and after treatment with the ultrasonic scaler held 1 mm away for 30 s, at low power (a,b) and medium power (c,d). The blue overlay shows the automatic detection of bacteria.

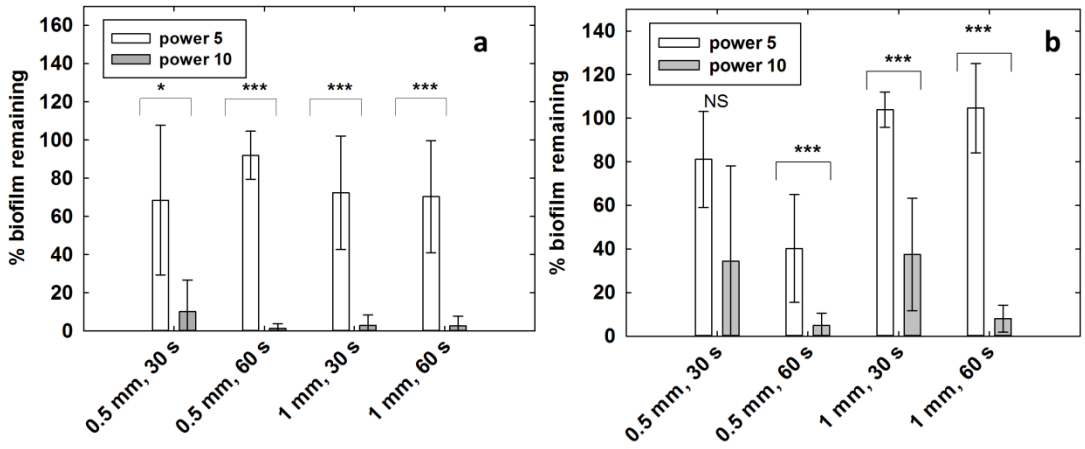

Figure 5.9 Mean percentage of biofilm remaining calculated from the segmented before and after images, (a) SLA surface, n=10 for each setting. (b) polished surface. n=8 for each setting. *p<0.05 ***p<0.001 (Rank Sum Test)

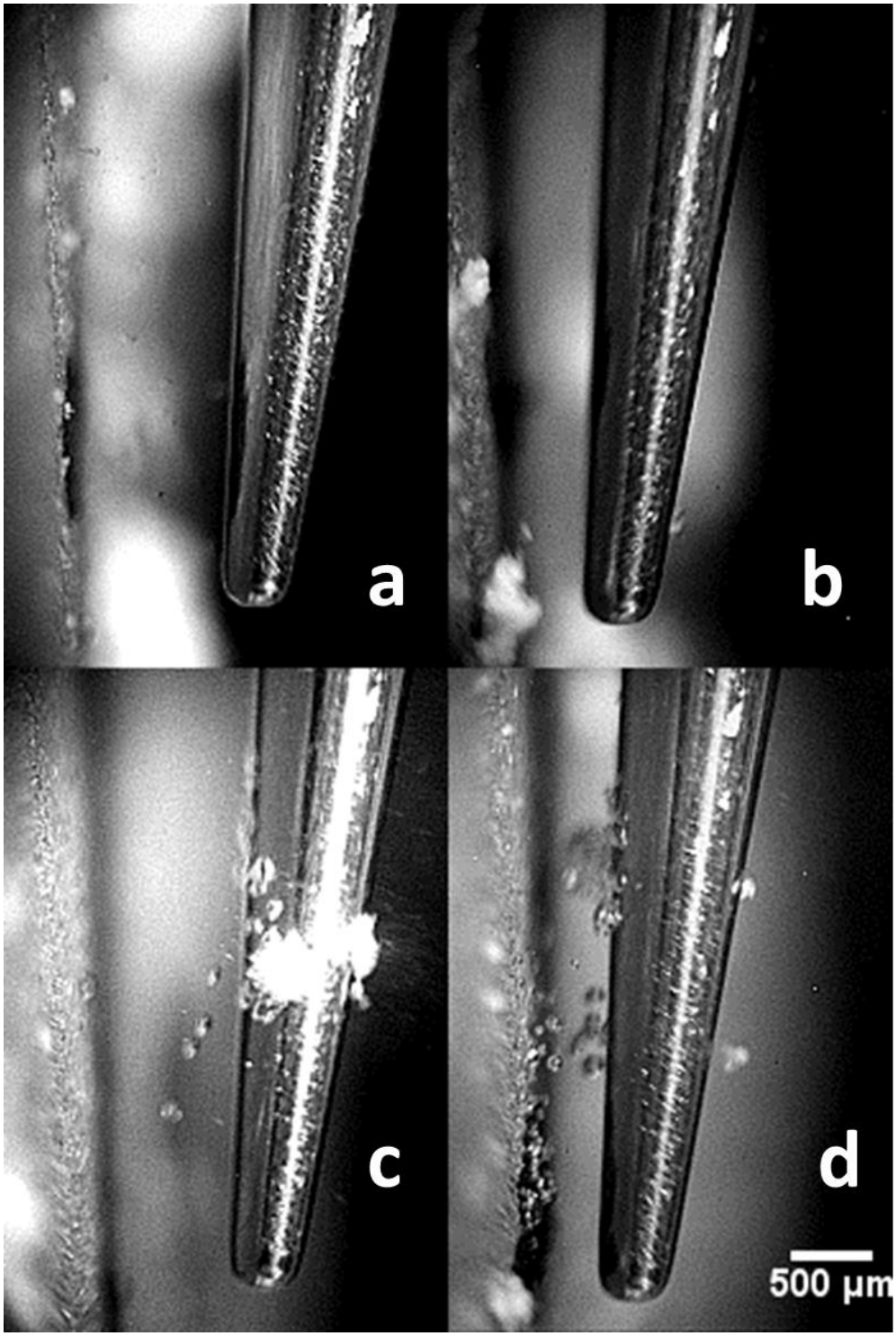

Figure 5.10 High speed image stills of the ultrasonic scaler tip next to the sample during biofilm removal. (a) power 5, 1 mm away from disc. (b) power 5, 0.5 mm away from disc. (c) power 10, 1 mm away from disc. (d) power 10, 0.5 mm away from disc.

5.4 Discussion

A large number of studies have reported the impact of experimental variables on biofilm disruption on native tissues and/or biomaterial surfaces, but have used qualitative methods or methods that have high susceptibility to measurement bias. As a consequence the interpretation of findings can be limited, impacting on technique development or adoption. The current study reports the development and validation of an image analysis protocol which can be used to quantify biofilm disruption on different surface topologies.

In contrast to previous studies which have used basic thresholding techniques to segment biofilm from low magnification microscopy images, the segmentation technique employed in this study uses machine learning, where a wide range of feature detection techniques including texture filters and edge detectors are used to train the algorithm from the image. As the method does not rely only on intensity differences in the image, it can be applied to segment SEM images where the background is non-uniform, such as tortuous biomaterial surfaces.

Another difference of this method is that no proprietary software is used; all image segmentation is done using the open source Fiji image processing package.

We have also tested the accuracy and the reproducibility of the method, which previous studies have not done. The ROC curve shows that segmentation was more accurate on the images of the polished discs, as expected, due to easier detection both automatically and manually as there was more contrast between the biofilm and background, and the surface was less irregular.

The accuracy of the segmentation of the SLA surface was lower (mean specificity 0.62±0.20 and mean sensitivity 0.80±0.18). This implies that the algorithm often detected bacteria where the reference segmentation labelled the area as surface. However, it should be noted that although manual segmentation is the gold standard and was therefore used as the reference segmentation, there were cases for the SLA samples where even an experienced operator may have inevitably incorrectly identified a few individual bacteria as surface. This however, does not invalidate the method. This occurred due to pixelation in the image making it difficult to resolve the individual bacteria (e.g. bottom right of Figure 5.5 b & c). There is an outlier on the ROC curve where the specificity is high (0.9) but the sensitivity is low (0.2). In this case it was difficult to identify a raised section in the image as biofilm/surface, and the operator labelled it as biofilm whereas the algorithm detected it as surface. Therefore it could be useful in similar cases to also take images in back-scattered electron mode and to perform energy dispersive X-ray spectroscopy to determine the chemical composition. The magnification of x1250 used in this study is sufficient to image and segment biofilm, however if individual bacteria need to be segmented then a either a higher magnification or a higher resolution would be required. Overall, the algorithm struggled to segment correctly in the same situations where the human operator struggled to segment correctly, and the lower sensitivity and specificity values are due to this.

Further work can be done to improve the accuracy of the method, for example by using other types of classifiers from the Weka Package manager and comparing the performance of different types of classifiers.

In terms of the biofilm removal effect, there was more disruption as the cavitation increased, as expected. Similar amounts of biofilm were removed at both 0.5 mm and 1 mm distance, suggesting that the scaler tip can be held at an even larger distance from the surface. The cavitation happened at only one point on the tip of 10P (Figure 5.10), so biofilm was removed in a small area on the disc. There were some locations imaged which were outside of the area where cavitation cleaned; this explains the result which was not statistically significant in Figure 5.9.

The graphs in Figure 5.9 suggest that more biofilm removal occurred from the SLA surfaces compared to the polished surfaces, which is an interesting finding. This result could be because the cavitation bubbles are more effective on the roughened surface due to its microgrooves. Tomita et al. (2002) have shown that surface roughness is a crucial reason for cavitation erosion, and it may also be a factor affecting cavitation cleaning. Further work (e.g. using high speed imaging) can be done to show the cavitation dynamics in more detail.

5.5 Conclusion

This study set out to objectively measure and assess biofilm removal from dental implant surfaces after applying cavitation from ultrasonic scalers. The second aim of this study was to find a new method for quantifying biofilm area from SEM images. The protocol for measuring the area of biofilm removal through the use of SEM finder grids and image processing is a novel application for quantitative analysis of SEM images before and after an experimental treatment. We have used this method to show that cavitation from ultrasonic scalers is effective at cleaning biofilm from dental implant surfaces, showing potential for this technique as a new method of dental implant debridement.

The protocol developed to determine biofilm area from SEM images will allow researchers who study biofilm growth and disruption to use SEM as a quantitative tool and will facilitate future breakthroughs in the field of medical implant infection.

The limitation of this study was the inability to accurately segment individual bacteria from complex surfaces, however these could also not be segmented manually by trained operators therefore the method is likely to be robust in cases where manual segmentation is possible.

This chapter has demonstrated that biofilm can be disrupted using cavitation from an ultrasonic scaler. The next part of this thesis will investigate another use of this cavitation for occluding dentinal tubules to treat dentinal caries and hypersensitivity.

6. IMAGING DELIVERY OF SUB-MICRON PARTICLES INTO DENTINAL TUBULES VIA ULTRASOUND

6.1 Introduction

The dentine in teeth consists of microscopic tubules which are arranged radially, running from the outside of the tooth to the pulp at the centre. On the outer surface they are covered by either the enamel or cementum and protected from the non-sterile oral environment. However, if the enamel or cementum is destroyed, either through acid erosion or attrition, the dentinal tubules can become exposed. This can lead to dentine hypersensitivity and dentinal caries. Bacteria which invade the tubules during caries invariably lead onto infection of the pulp chamber. This will cause pulp or periapical disease which can result in tooth loss (Love & Jenkinson, 2002). Eliminating the bacteria in dentinal tubules is fundamental to treating dentinal caries (Fejerskov & Kidd, 2009). Another problem that patients may suffer from is dentinal hypersensitivity. This is a common occurrence, with a prevalence of up to 57% (Dababneh et al, 1999). It presents as a short, sharp pain in the sensitive teeth when exposed to certain external stimuli such as cold, heat or dehydration. It is thought to occur due to fluid movement

in exposed tubules, which causes pain by distorting the plasma membrane of mechanoreceptors present on nerves at the inner end of the tubules (Brännström, 1986). This is the most commonly accepted explanation and is known as the hydrodynamic theory of dentine sensitivity (Dababneh et al, 1999). Therefore it is widely accepted that decreasing this movement, by reducing the permeability of the dentine, will lead to preventing the sensitivity pain and discomfort. This can be achieved through partially or fully blocking the tubules (Tian et al, 2014). The use of tubule blocking agents is a major area of interest within the oral healthcare industry for treating dentinal hypersensitivity (Dababneh et al, 1999).

The diameter of dentinal tubules varies from 2-4 µm (Ohl et al, 2010) and is wider near the centre of the tooth. To eliminate bacteria which have invaded the dentinal tubules, antimicrobials can be delivered during root canal therapy through the irrigant (Azim et al, 2016). Although they can penetrate into the tubules, this may be limited due to their small diameter and difficulty of covering the large number that are present. , This makes it difficult to treat dentinal caries using such techniques (Afkhami et al, 2015).

A range of chemicals and pastes are available which work by either blocking the dentinal tubules or causing dentine remineralisation. Clinically the most common materials employed are dentine bonding agents or glass ionomer cements (Dababneh et al, 1999). These can relive pain temporarily, but they become dislodged during brushing and eating and need to be frequently reapplied (Tian et al, 2014). Therefore there is an opportunity to develop a tubule blocking agent which can be retained for longer (Besinis et al, 2012; 2014; 2016).

Nanoscale materials have attracted interest as a more efficient method of delivering antimicrobials and remineralisation agents into dentinal tubules (Besinis et al, 2015;

Samiei et al, 2016). Sub-micron particles (SMPs) with a diameter between 100 – 1000 nm are considered to be safe, and have been shown to cause less inflammation than nanoparticles (NPs) (Oberdörster, 2000). NPs and SMPs have a large surface area, increasing their solubility and reactivity. If they are dispersed, they can easily enter dentinal tubules as their diameter is smaller than the tubule diameter (Tian et al, 2014). Such properties of NPs & SMPs may allow them to be delivered further into dentinal tubules, with the potential to be more effective than current treatments. This would be advantageous by allowing antimicrobials to reach bacteria deep in the tubules, and also for increasing the retention time of remineralising and tubule occluding materials. NPs and SMPs used for dentine tubule occlusion include nano-HA particles to act as seeds for remineralisation, and antibacterial nanoparticles such as silver and chitosan. Applying antimicrobial NPs into dentinal tubules from the outer surface of the tooth to treat early dentinal caries could preserve the tooth, eliminating the need for destructive restorative treatment. This would also make it less time consuming and more cost effective.

Mesoporous silica nanoparticles and sub-micron particles have attracted considerable research attention because their interior pore area and outer surface can be modified with functional groups (Chiang et al, 2014; Tian et al, 2014). Therefore it is possible to attach antimicrobials and/or calcium and phosphates to the particles and use them as delivery vehicles to transport antibacterials deeper into dentinal tubules. It has also been suggested that silica nanoparticles could bind to calcium receptors on the dentine surface, allowing the transport of remineralising agents into the tubules (Tian et al, 2014). Nanoparticles with a fluorescent agent have also been studied to enable investigation with a wider range of imaging modalities (Claire et al, 2015).

A key issue with NPs and SMPs is that it is difficult to deliver them deep into the dentinal tubules. Previous studies include the use of acetone or cavitation bubbles to help in delivering NPs further. Besinis et al. showed how acetone could be incorporated into nanoparticle solution to act as a carrier to deliver NPs further into dentinal tubules (2016). It could have the potential to displace water in the tubules, enabling the NPs to travel further inside. The investigators used nano-hydroxyapatite particles for remineralisation (Besinis et al, 2015) and found that the wettability of the NP solution significantly increased after addition of acetone and remineralisation of the tooth was therefore more effective. As acetone is already used in dentine bonding systems clinically, it is considered to be a safe ingredient for clinical use in dental applications.

Nanoparticle aggregation also hinders their delivery deep into the dentine. Claire et al. assessed the effect of surfactants on sub-micron silica particles and how this affected the surface interactions with dentine (2015). Surfactants reduce the surface tension, therefore reducing the hydrophobicity of the particles and preventing accumulation. Tubule occlusion was observed in SEM and confocal microscopy images with the Zonyl surfactant added, but fewer nanoparticle aggregations were observed with the Tween-20 surfactant added.

Shreshta et al. and Ohl et al. illustrated how cavitation could be used to deliver chitosan nanoparticles into dentinal tubules (Ohl et al, 2010; Shrestha et al, 2009). High speed imaging of a macroscale system simulating nanoparticles in dentinal tubules showed how cavitation bubbles with a diameter of 6.6 mm could push a rubber ball into an acrylic tube with a diameter of 3.3 mm. This was then repeated using dentine specimens and SEM images showed penetration of chitosan NPs up to 1 mm inside dentinal tubules. One limitation of this study is that for the method to be used

clinically, a new instrument would need to be developed. Instead, investigating the effect of cavitation from a clinically available dental instrument such as an ultrasonic scaler would therefore be more practical and could allow quicker transition of the research to the clinic. The aims of this research are to investigate the impact of cavitation from ultrasonic scalers, combined with acetone, in enhancing particle penetration into dentinal tubules. We hypothesize that:

1. Cavitation from ultrasonic scalers can deliver sub-micron silica particles into dentinal tubules.

2. Cavitation can break up aggregations of particles

3. Addition of acetone helps to deliver particles further into tubules.

6.2 Materials and Methods

6.2.1 Dentine Specimen Preparation & Particle Application

Intact, caries free, single-rooted human molars and premolars were used in this study. The use of teeth was authorised by a licence from the United Kingdom Human Tissue Act (HTA) (Licencing number: 12313, Clinical Research Network Consortium Reference: BCHCDent355.1548.TB). Teeth were decoronated at the cemento-enamel junction and 2 mm thick longitudinal slices were cut from the external surfaces of the roots using a low speed water cooled saw (Buehler, Isomet, UK). The area of each section was 8 ±1 mm length, 5 ±1 mm width. The outer surfaces of the slices were ground using silicon carbide (SiC) paper with grit size P500 until nominally flat, and then polished using P1200 and P4000 grade SiC paper to remove microscale grooves. The tooth slices were then immersed in 10% citric acid (BDH, Poole, England) for 2 minutes to remove the smear layer and expose the dentinal tubules. Following this the

samples were ultrasonicated in an ultrasonic cleaner (In-ceram, Vitasonic) in 200 ml RO water for 10 minutes. Samples were then imaged using a Zeiss PrimoTech stereomicroscope (Zeiss Oberkochen, Germany) (resolution 17 pixels/µm), to determine the direction of the dentinal tubules. Only specimens with dentinal tubules orientated perpendicular to the surface were used in this study to mimic the clinical situation where the tubules on the outer portion of the cervical third of the root become exposed. The specimens were stored in a humidified container until use.

The silica (SiO_2) particles were prepared according to a published method (Lewis et al, 2012) containing a luminescent ruthenium complex (tris-(2,2'-bipyridyl)ruthenium(II) dichloride) for introducing a luminescent core for potential luminescence imaging. Dynamic Light Scattering (DLS) was used to estimate the particle size distribution (Zetasizer Nano ZSP, Malvern Instruments, UK). 1% w/v solutions of sub-micron particles were prepared by adding 0.1g particles (dry weight) to 10 ml reverse osmosis (RO) water and 10 µl Tween 20 surfactant (Sigma-Aldrich) (Claire et al, 2015). The solution was dispersed via ultrasonication for 10 min and then centrifuged at 8000 rpm for 5 minutes. The supernatant was discarded and the particles were re-suspended in either 10 ml RO water or 5 ml RO water mixed with 5 ml acetone. Solutions were ultrasonicated for 10 min before application to the tooth slices to disperse the particles.

Each particle solution (5 ml) was pipetted into a compartment in a 12 well culture plate, and a tooth slice was placed inside. An ultrasonic scaler (P5 Newtron, Satelec, Acteon, France) with tip 10P was fixed 0.5 mm away from the tooth slice using a translation stage accurate to 10 µm (PT3, Thorlabs, USA) (Figure 6.1). The scaler was operated for 20 s at either power 1 (no cavitation) or power 10 (with cavitation) (n=6). The same procedure was used for both particle solutions.

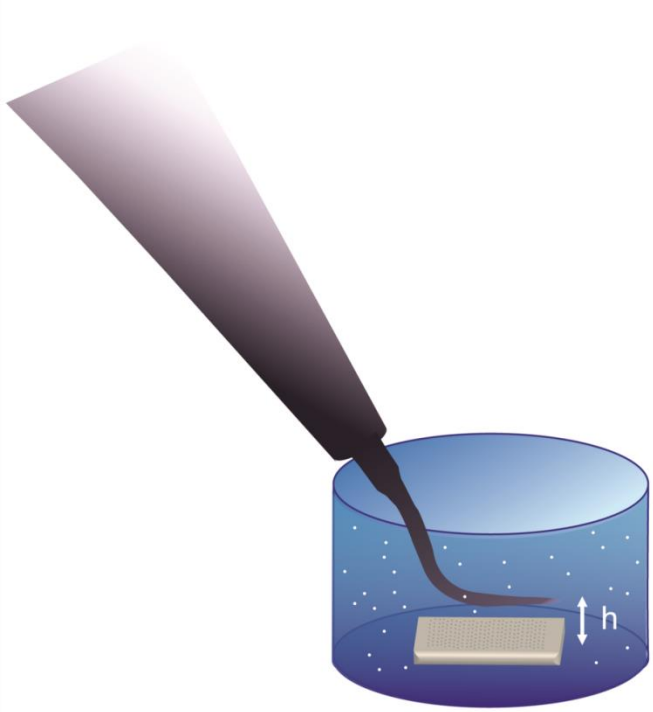

Figure 6.1 Schematic of experimental setup showing the orientation of the ultrasonic scaler. The tip was placed inside a well of a 12 well plate filled with 5 ml particle solution. The dentine slice was placed at the bottom of the well and the scaler was positioned at a fixed height h above the slice (h = 0.5 mm)

6.2.2 Scanning Electron Microscopy

Samples were then dried for 1h in a 60^{o}C oven and gold-coated (K550X, Quorum Technologies, UK) for SEM (EVO MA10, Zeiss). After imaging the surface of the samples, they were cryogenically frozen in liquid nitrogen, fractured manually using a hammer and dental chisel, gold coated and imaged in SEM perpendicularly to determine the depth the particles had travelled into the dentinal tubules. Acceleration voltages of 5-20 kV were used in secondary electron mode for SEM imaging. A dentine specimen was also imaged with no particles to determine the average tubule diameter.

A representative dentine slice from SEM measurements was also analysed using focussed ion beam (FIB) SEM (Quanta 3D FEG, FEI). The electron beam was operated at 20 kV with spot size 6-8 and the ion beam was operated at 30 kV. The initial trench was cut using milling parameters of 7 nA at 52°, and subsequent milling was performed at 2 nA, and then, 1 nA at 54°. FIB SEM was done by Theresa Morris, Centre for Electron Microscopy, University of Birmingham.

6.2.3 Image Analysis

Image analysis was performed using the Fiji distribution of the ImageJ software (Schindelin et al, 2012) (U. S. National Institutes of Health, Bethesda, Maryland, USA). The diameter of the dentinal tubules was calculated from SEM images of acid etched dentine. The 'minimum' automatic threshold was applied to segment the tubule openings. This was chosen after trying all of Fiji's auto thresholding methods (Figure 6.4) as it segmented the tubules with the least amount of noise. It works optimally when the image histogram is bimodal, which was the case with these images (the image histogram was obtained using the histogram feature in Fiji). The minimum method works by smoothing the histogram for an average of 3 successive iterations until there

are two maxima, and the threshold is calculated as the value between the two maxima. This segmentation technique was chosen instead of the trainable weka segmentation used in the previous chapters because it is less computationally intensive and there was sufficient contrast in the images to enable segmentation by thresholding.

After thresholding, objects which had a circularity less than 0.95 and size less than 2 μm^2 were removed to eliminate noise and tubules which had not been completely segmented. The Feret diameter of the objects was calculated from the particle analysis plugin in Fiji.

The coverage of the dentine surface by the sub-micron particles was also calculated for the different settings (with/without cavitation/acetone) (Figure 6.2). The brightness was reduced and contrast was increased manually to prevent the algorithm from thresholding the open dentinal tubules. The same brightness and contrast adjustments were applied to all the images being tested (minimum displayed value: 60, maximum displayed value: 255). The images were then segmented automatically using the 'minimum' threshold as described above. The percentage of surface covered by the particles was calculated from the histogram of the image, where the number of segmented pixels (pixels with intensity 255) was extracted. The ratio of this to the total number of pixels in the image gave the percentage of area covered.

SEM images were also used to confirm the size of the particles together with DLS studies by thresholding the images using the Huang auto-thresholding method, and retaining objects with size 30-300 and circularity >0.95 to remove noise and aggregated particles. The area of each particle was calculated using Fiji's particle analysis plugin. The particle diameter was calculated from the area, assuming circularity.

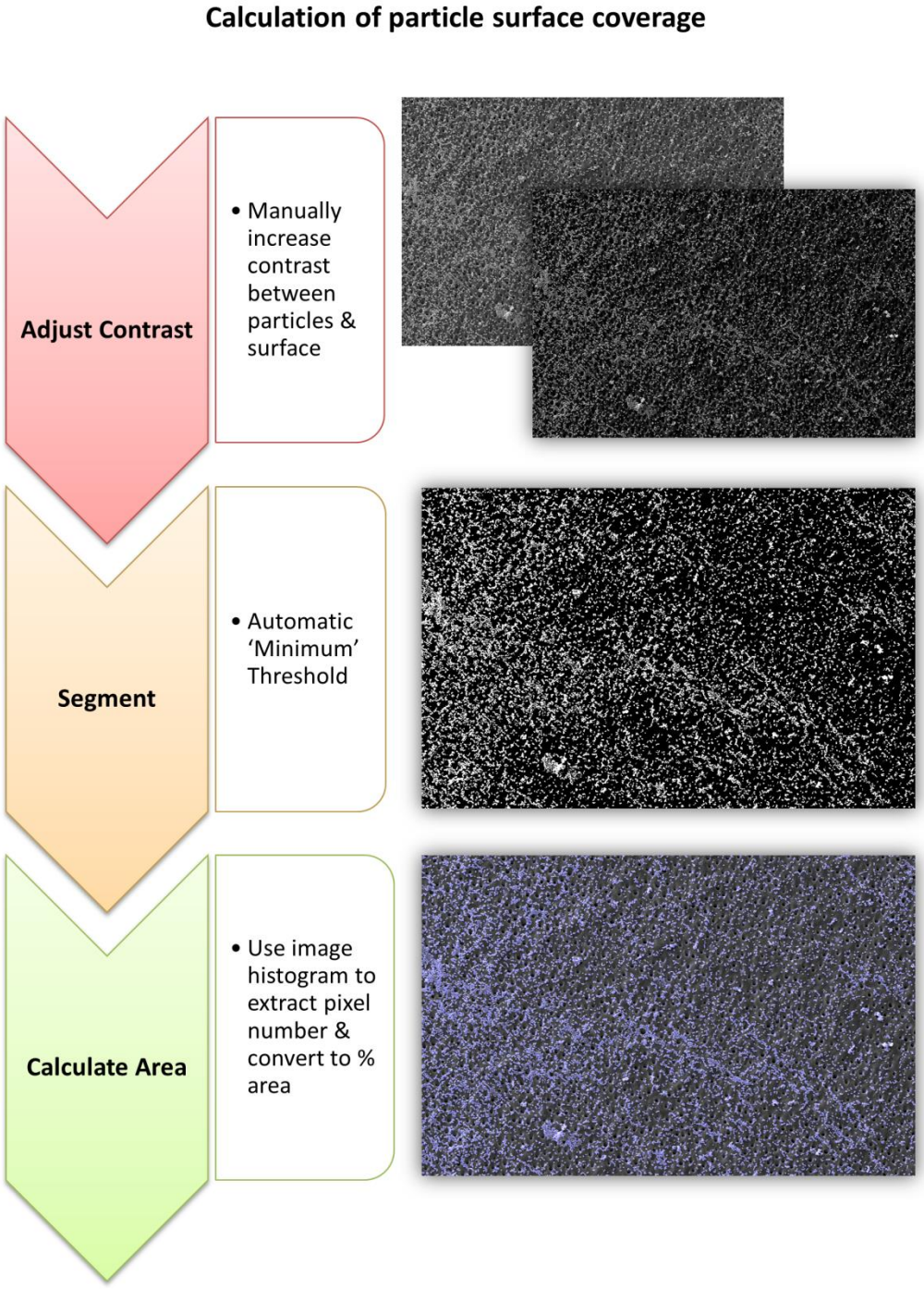

Figure 6.2 Flow chart showing the image analysis steps for calculating the percentage of the dentine surface covered in sub-micron particles.

6.3 Results

SEM images were used to calculate the dentine tubule diameter (Figure 6.3b & d). Out of 2,239 tubules detected from 5 images, the median diameter was 3.0 µm (Figure 6.3c). The dentine surface before application of particles was smooth and did not contain any grooves from the polishing stage (Figure 6.3e).

Dynamic light scattering provided the particle size in solution to be 960 ± 210 nm (intensity distribution) and 910 ± 210 nm (number distribution). The poly-dispersion index was 0.2 (number distribution) and 0.3 (intensity distribution). The mean particle diameter as calculated from the Feret diameter calculations of particles in the SEM images was 960±70 nm. (Figure 6.5b).

The ability of the SMPs to occlude and penetrate inside dentinal tubules was first investigated. Dentine tubule occlusion was found using SEM (Figure 6.6). Full and partial occlusion of some tubules at the surface was observed for all settings (with and without cavitation, with and without acetone) and there was no visible difference in the amount of tubules obstructed. Some dentinal tubules remained open with no occlusion at the surface. For the settings where cavitation was applied, micro indentations were seen on the dentine surface.

The particles covered approximately 50% of the dentine surface in all of the cases (Figure 6.7). There were larger agglomerations of particles on the dentine surface when cavitation was not applied (Figure 6.8 a & b) compared to when cavitation was applied (Figure 6.8 c &d). For the settings where the particles were in water, some appeared to

be sealed into the tubules (Figure 6.9). For the settings where cavitation was applied, micro indentations were seen on the dentine surface (Figure 6.10).

The dentine surface was not completely horizontal as shown by the stereomicroscopy images showing the particles on the sample, with only parts of the image in focus (Figure 6.11).

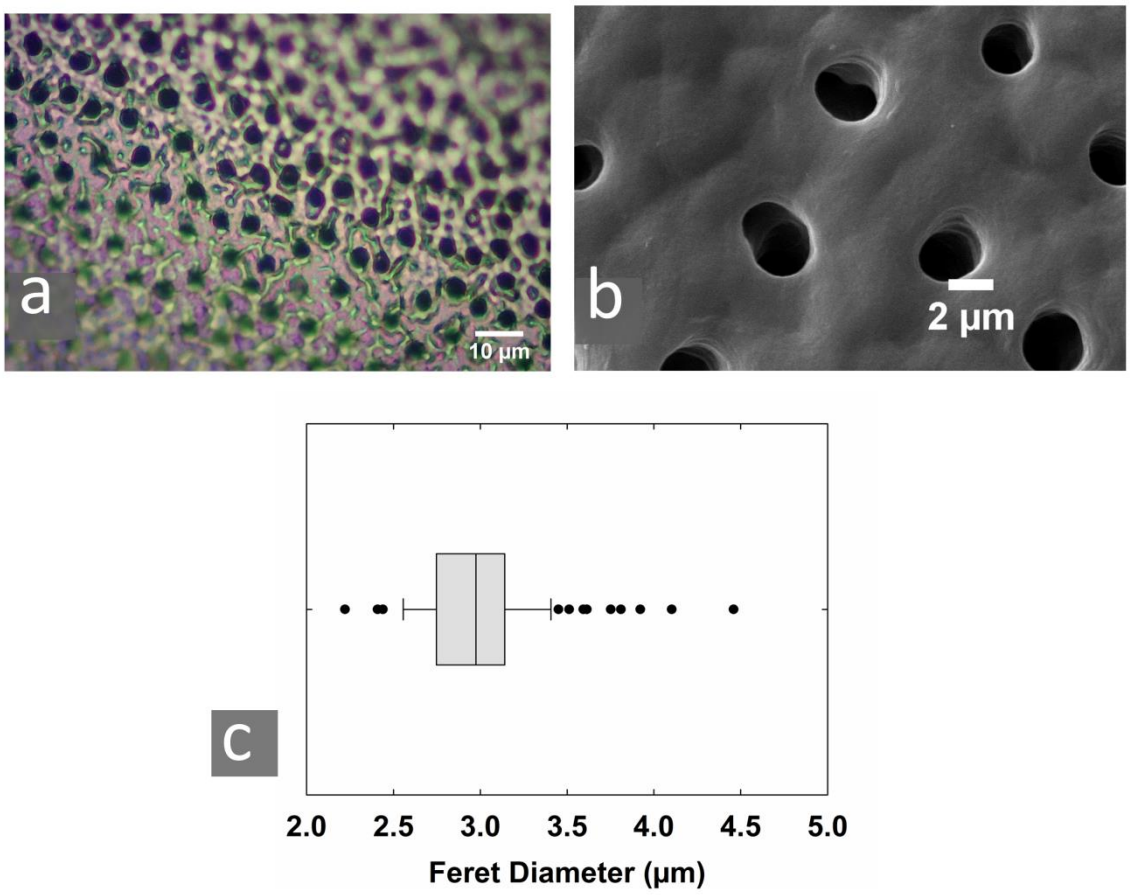

Figure 6.3 Images of the acid etched dentine surface (a) stereomicroscope image of dentine specimen with tubules perpendicular to the surface. (b) low magnification SEM image of dentine specimen (c) Box and whisker plot showing the average diameter of dentine tubules.

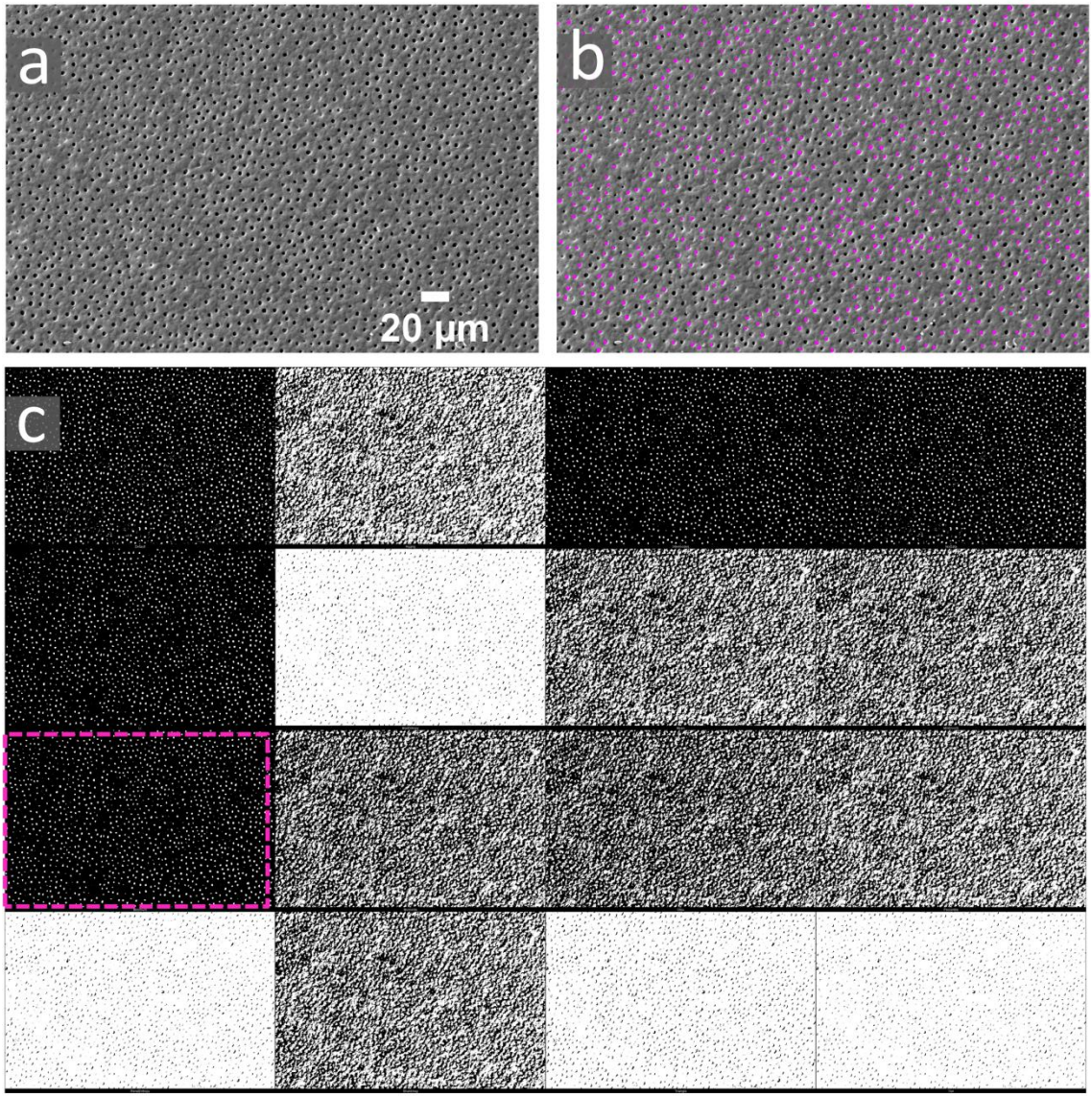

Figure 6.4 (a) high magnification SEM image of the dentine surface (b) example of a thresholded image used for diameter calculations overlaid on the original SEM image. Tubules included in the segmentation are shown in magenta (c) Montage of ImageJ's 'try all' auto threshold feature, used for determining the thresholding method. The chosen method, minimum, is outlined in the magenta colored box.

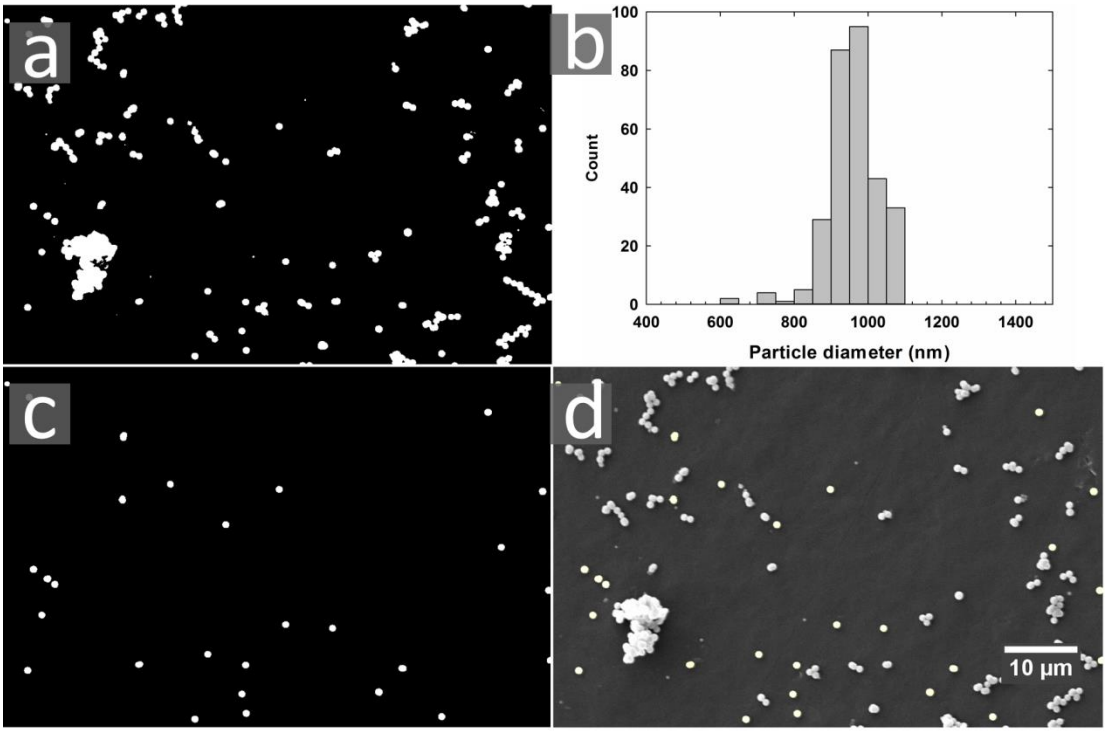

Figure 6.5 Calculation of the silica particle size distribution. (a) thresholded image (b) histogram showing particle diameter distribution (c) Thresholded image after removal of noise and agglomerated particles (d) Overlay of thresholded image on the original SEM image. Individual particles included in the segmentation are shown in yellow.

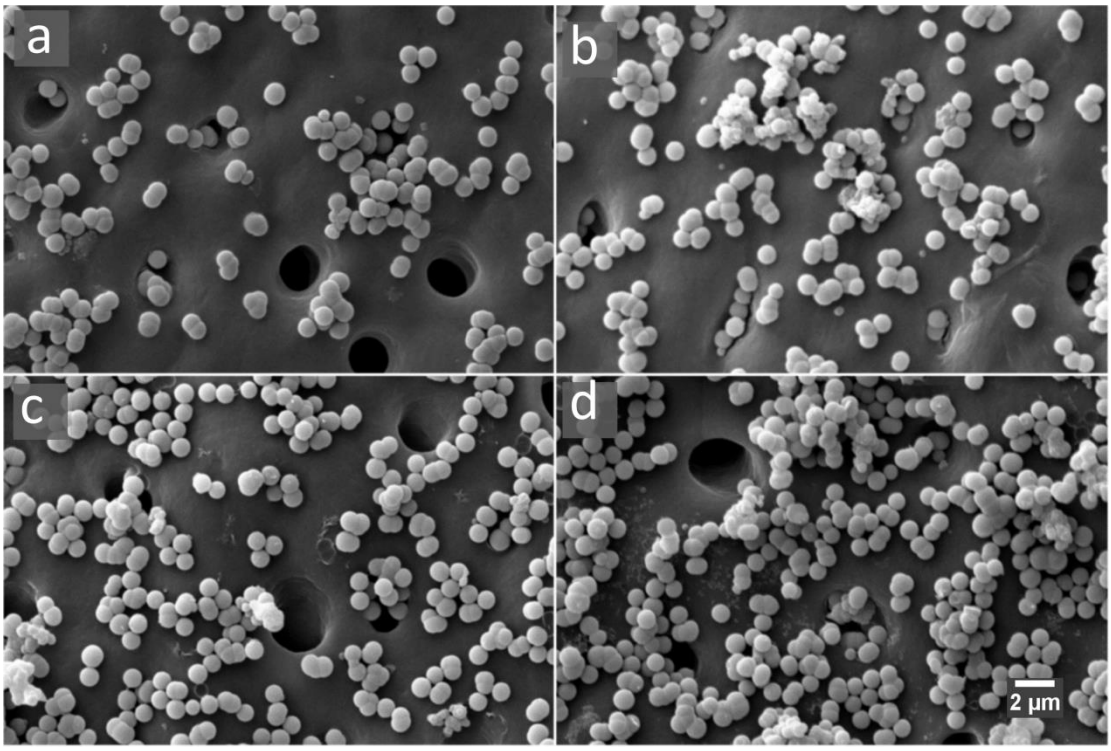

Figure 6.6 Electron micrographs of the particles on the dentine surface at x11,000 magnification (a) particles in 50% acetone, no cavitation applied (b) particles in water, no cavitation applied (c) particles in 50% acetone, cavitation applied (d) particles in water, cavitation applied.

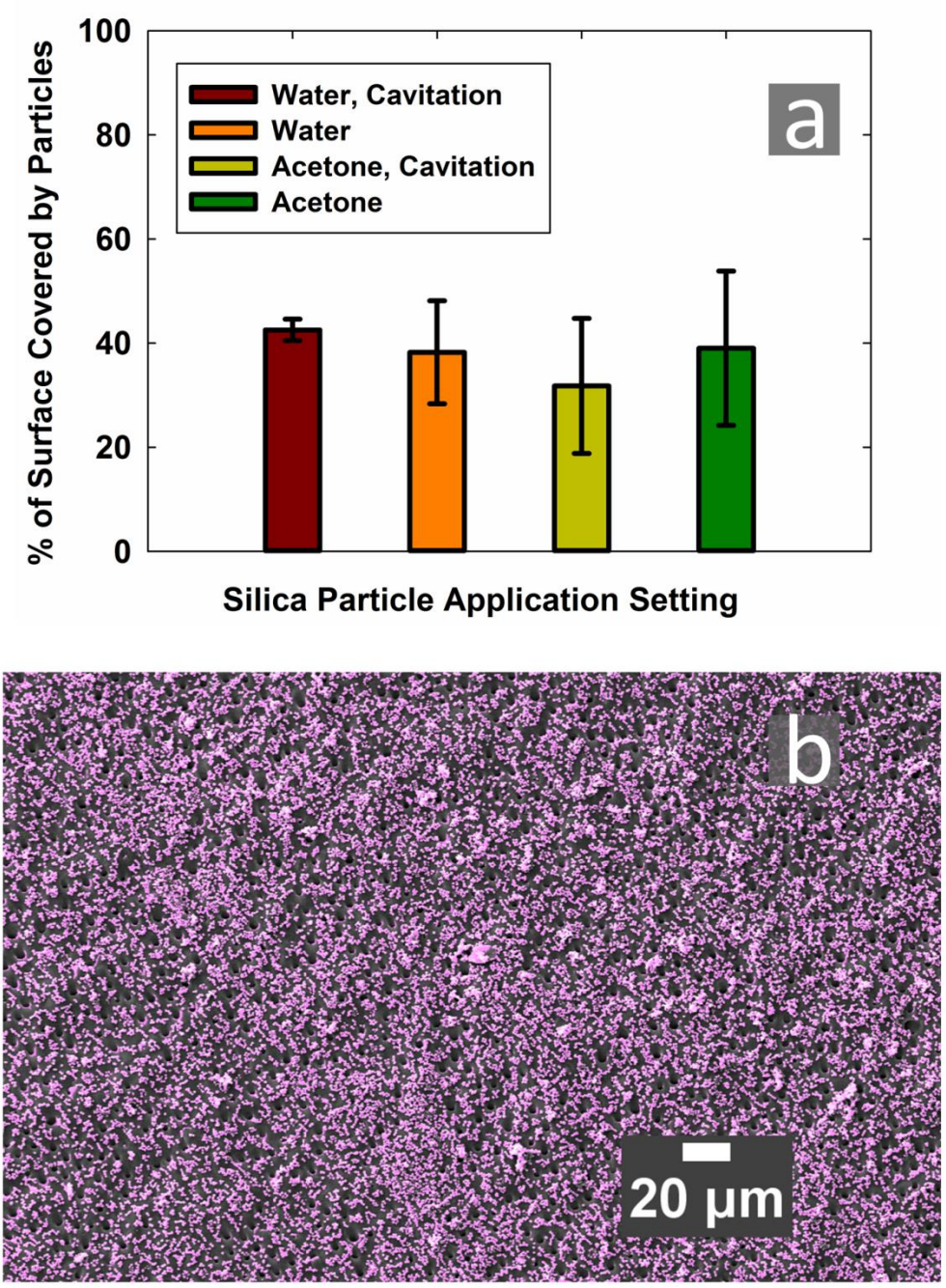

Figure 6.7 (a) Percentage of the dentine surface covered by the Si particles calculated using image analysis (b) Example showing one of the thresholded images used for calculating the area covered by particles, merged with the original SEM image.

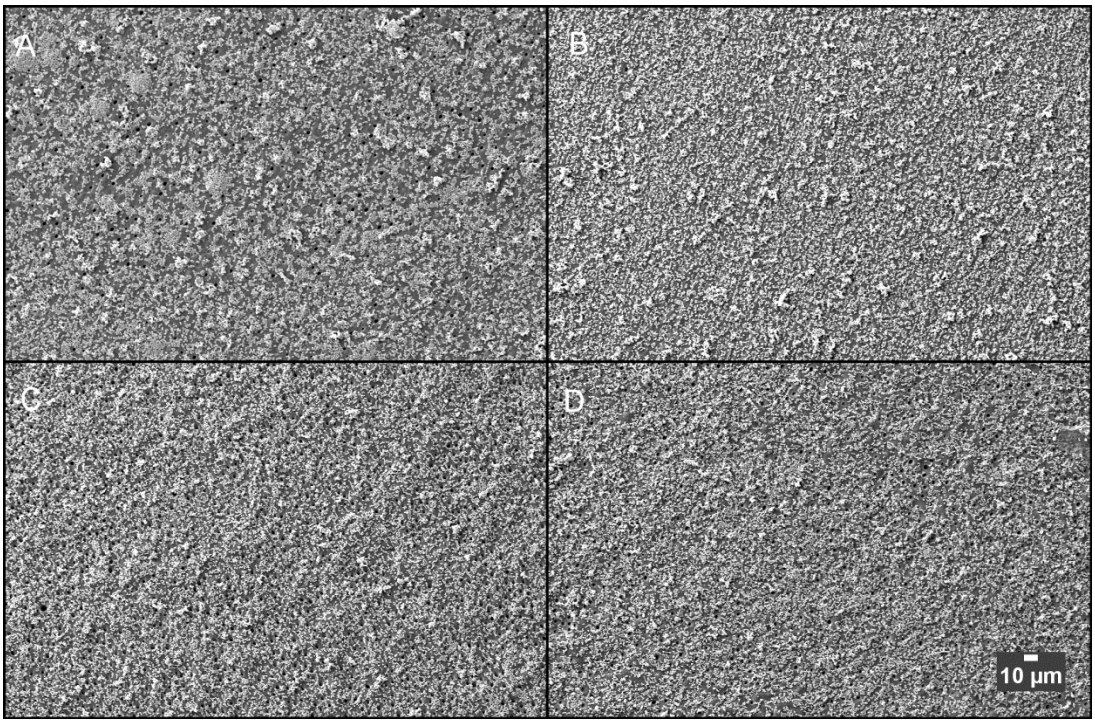

Figure 6.8 Low magnification SEM image of the particles on the dentinal surface showing larger agglomerations of particles when cavitation was not applied (a) particles in 50% acetone, no cavitation applied (b) particles in water, no cavitation applied (c) particles in 50% acetone, cavitation applied (d) particles in water, cavitation applied.

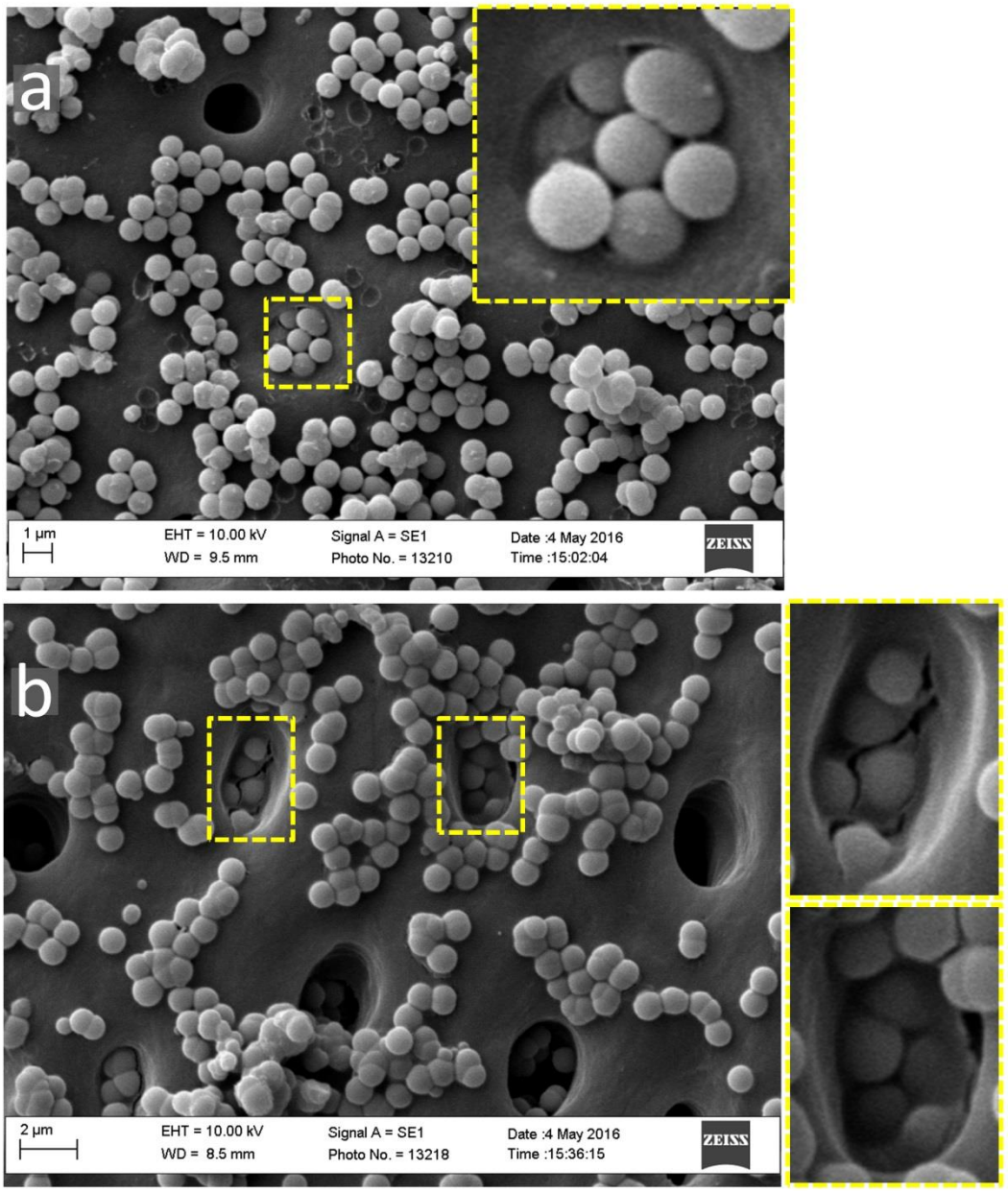

Figure 6.9 SEM images showing the Si particles sealed inside some dentinal tubules, outlined in yellow (a) cavitation applied, particles in water (b) no cavitation applied, particles in water

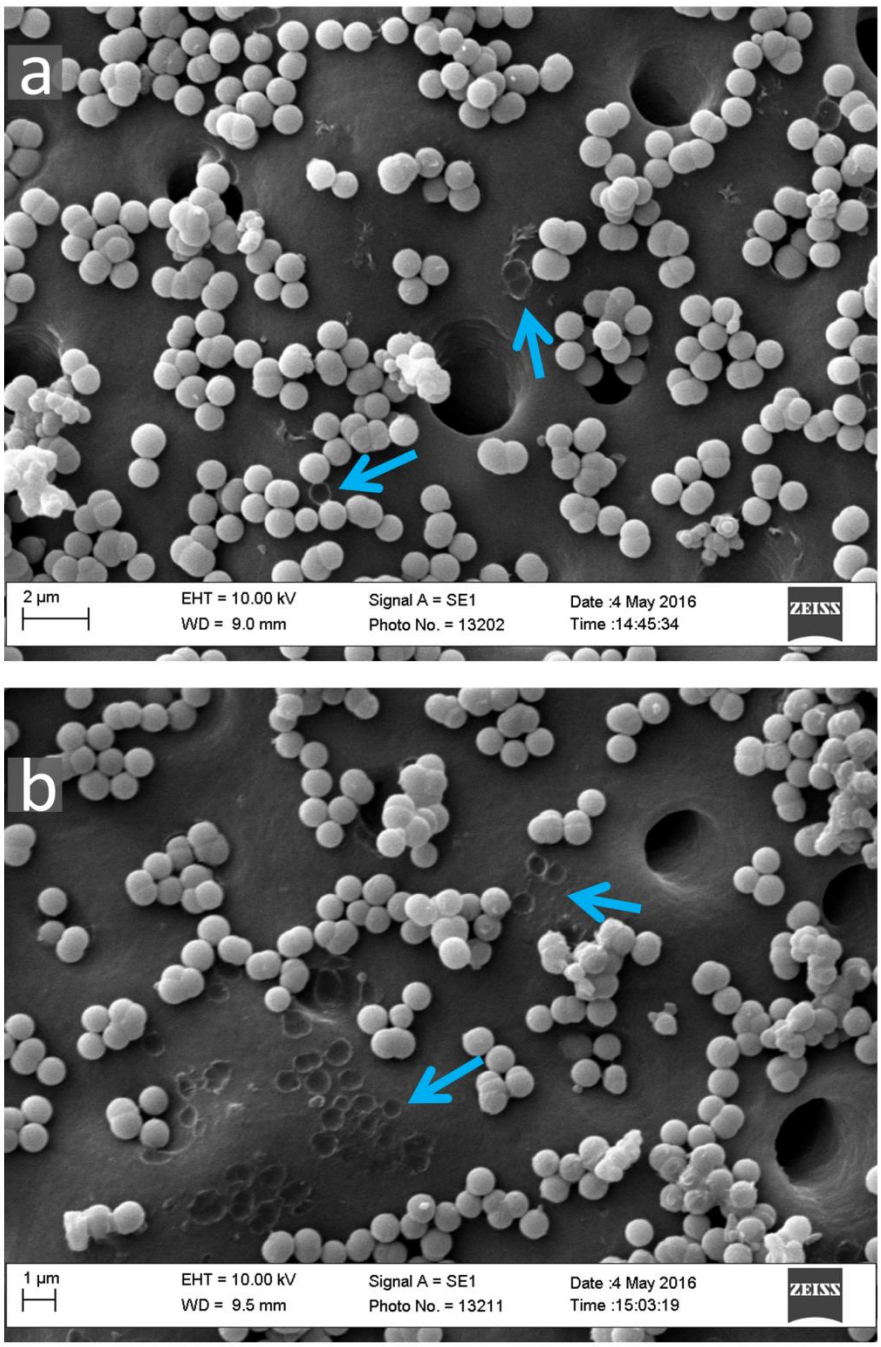

Figure 6.10 SEM images showing indentations in the dentine when cavitation was applied (a) particles in acetone (b) particles in water

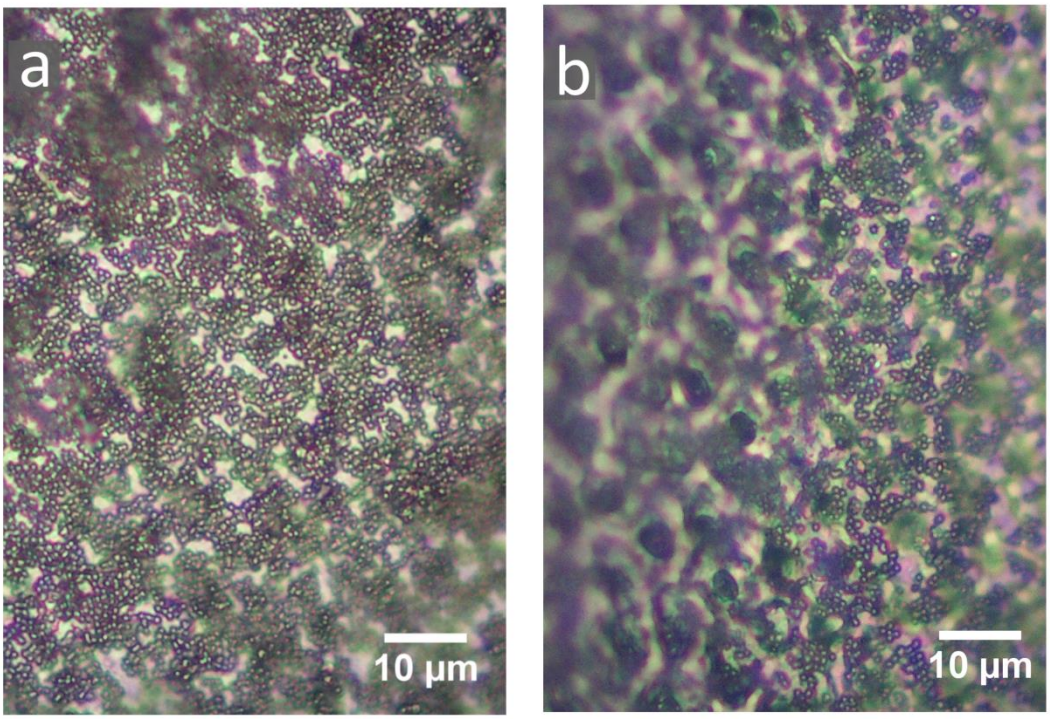

Figure 6.11 Stereomicroscope images of the particles on the dentine surface (a) particles in water, no cavitation applied (b) particles in acetone, no cavitation applied

Penetration of particles into the dentinal tubules was observed for all settings (Figure 6.12, Figure 6.13, Figure 6.14, Figure 6.15). For the particles in acetone, this was seen up to a distance of approximately 80 µm when cavitation was not applied and up to ~120 µm when cavitation was applied. Particles that had been dispersed in only water were observed to enter into the tubules up to a distance of approximately 60 µm when there was no cavitation and up to ~180 µm when there was cavitation.

Fracture face SEM images showed that in some cases the particles had obstructed the tubules near to the surface of the dentine (Figure 6.16). Although particles entered into some tubules, many were empty (Figure 6.17). The fracture of the dentine did not always occur vertically and in these cases it was not possible to view the full path of individual tubules in the dentine (Figure 6.17).

Imaging the dentine surface at an angle showed peaks and troughs where the tubule openings were (Figure 6.18). However, the particle distribution appears to be random and not affected by the surface irregularities. Particle deposition can be seen both in the valleys and on the peaks of the dentine.

Tubules could be milled to view particle penetration near to the surface using FIB SEM (Figure 6.19). One particle was found inside the tubule near the surface in one of the cases (Figure 6.19e) but for other cases there were no particles inside the tubules near to the surface.

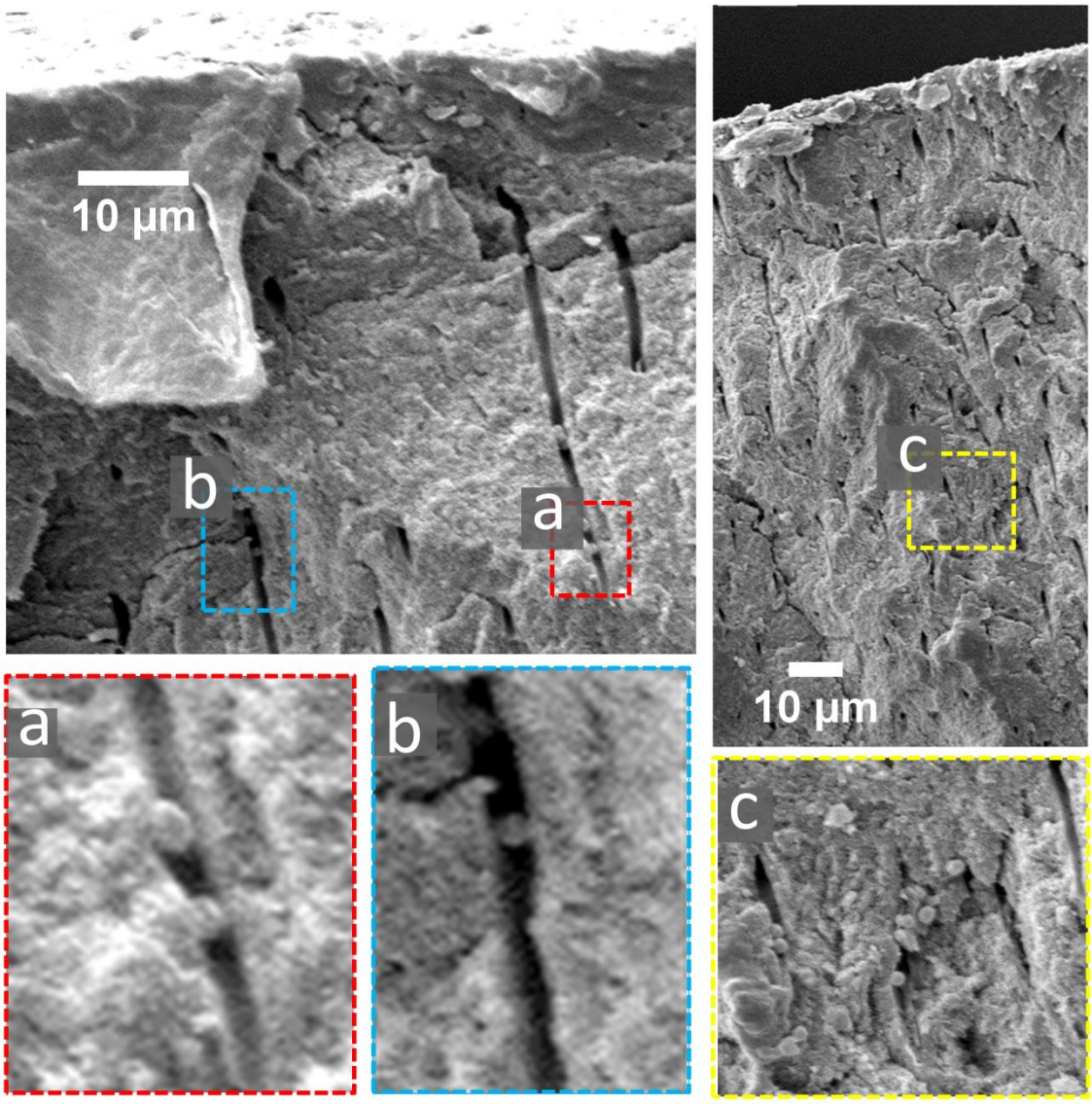

Figure 6.12 Cross section of a dentine specimen with particles in acetone, without cavitation and corresponding magnifications showing penetration of the particles into the dentinal tubules.

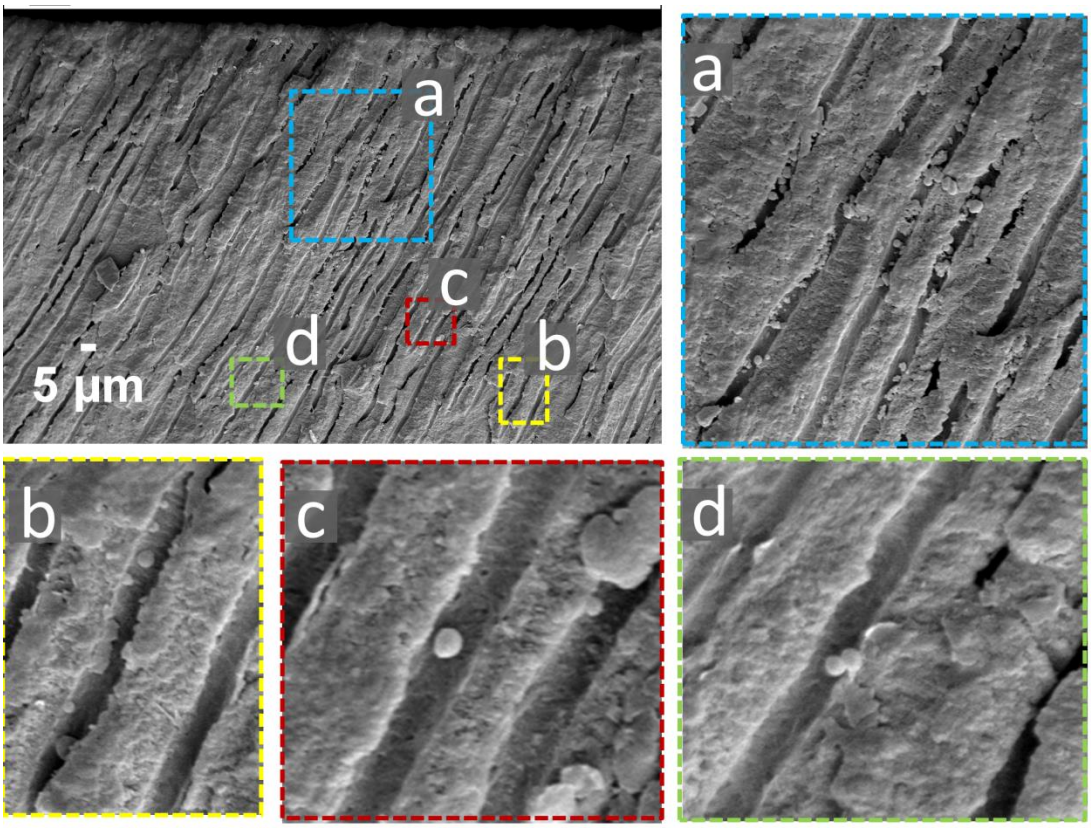

Figure 6.13 Cross section of a dentine specimen with particles in acetone with cavitation applied, and corresponding magnifications showing penetration of the particles into the dentinal tubules.

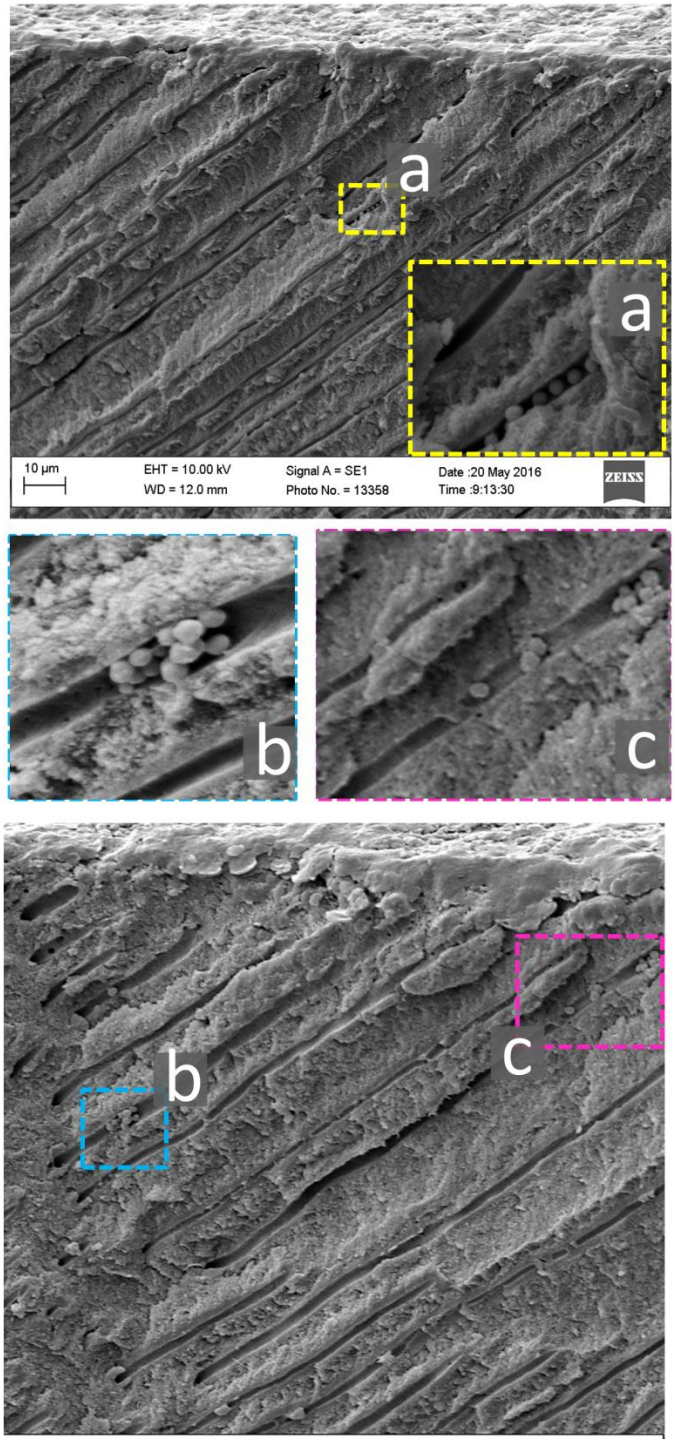

Figure 6.14 Cross section of a dentine specimen with particles in water, without cavitation, and corresponding magnifications showing penetration of the particles into the dentinal tubules.

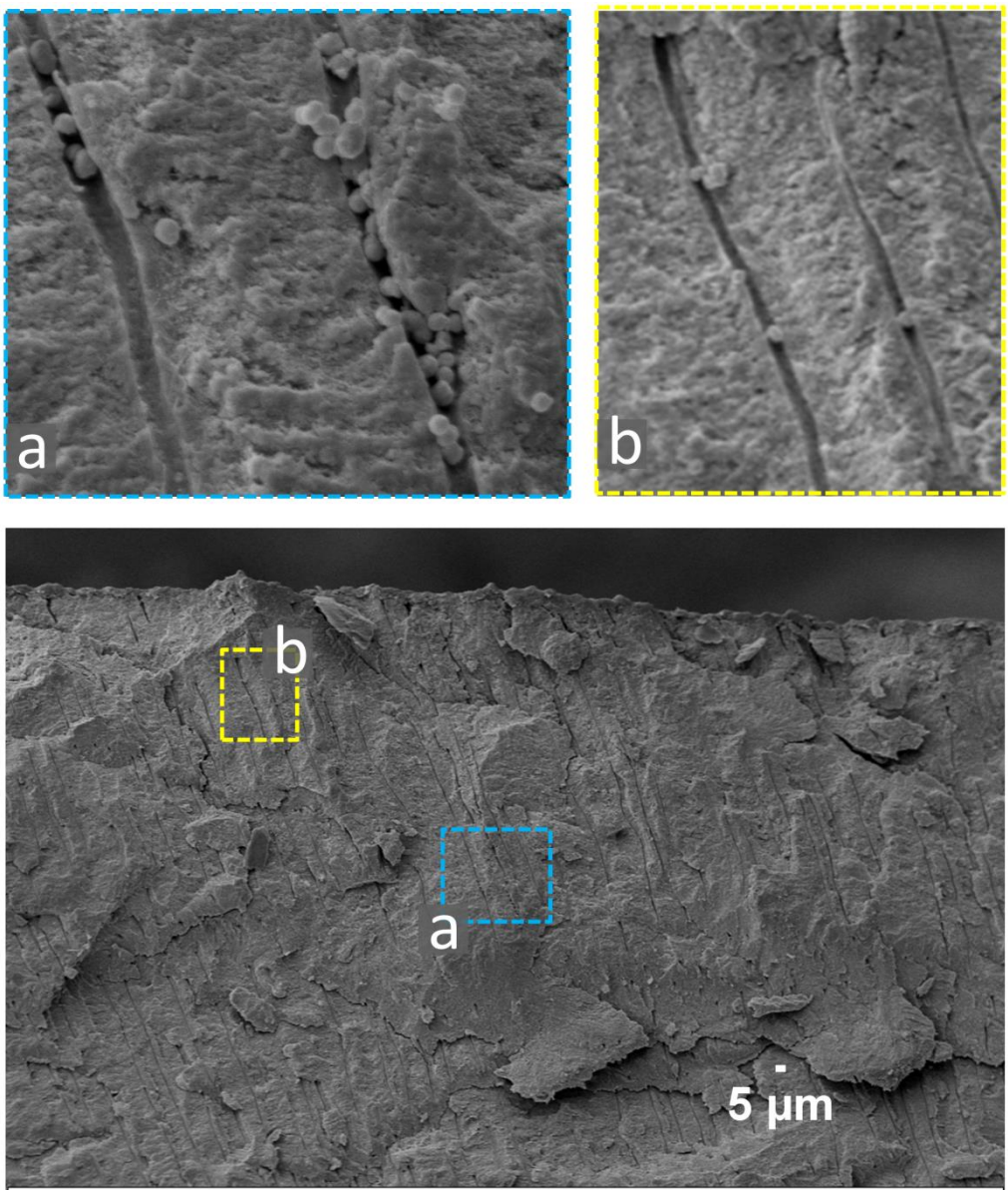

Figure 6.15 Cross section of a dentine specimen with particles in water with cavitation applied, and corresponding magnifications showing penetration of the particles into the dentinal tubules.

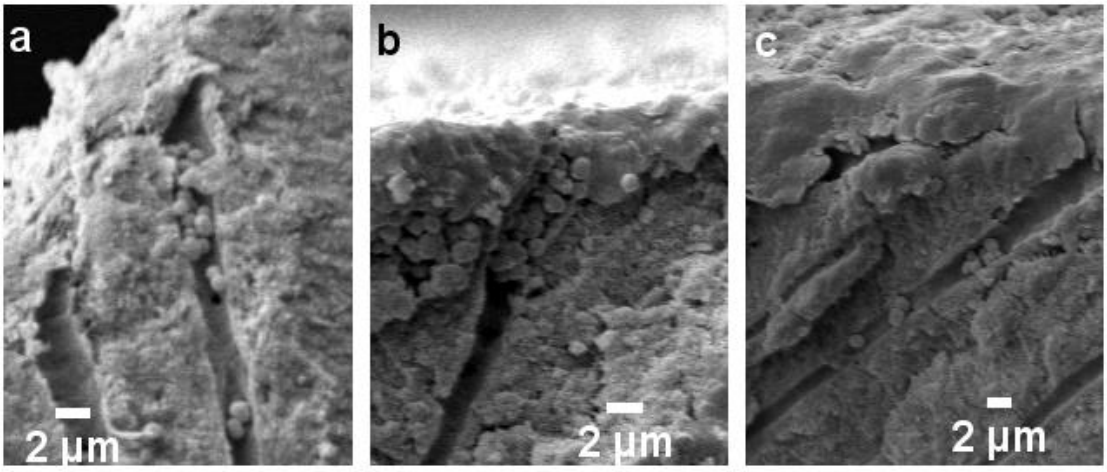

Figure 6.16 Cross section images of dentine specimens showing tubule occlusion near the opening of the tubules (a) particles in acetone, cavitation applied (b) particles in water, cavitation applied (c) particles in water, no cavitation applied

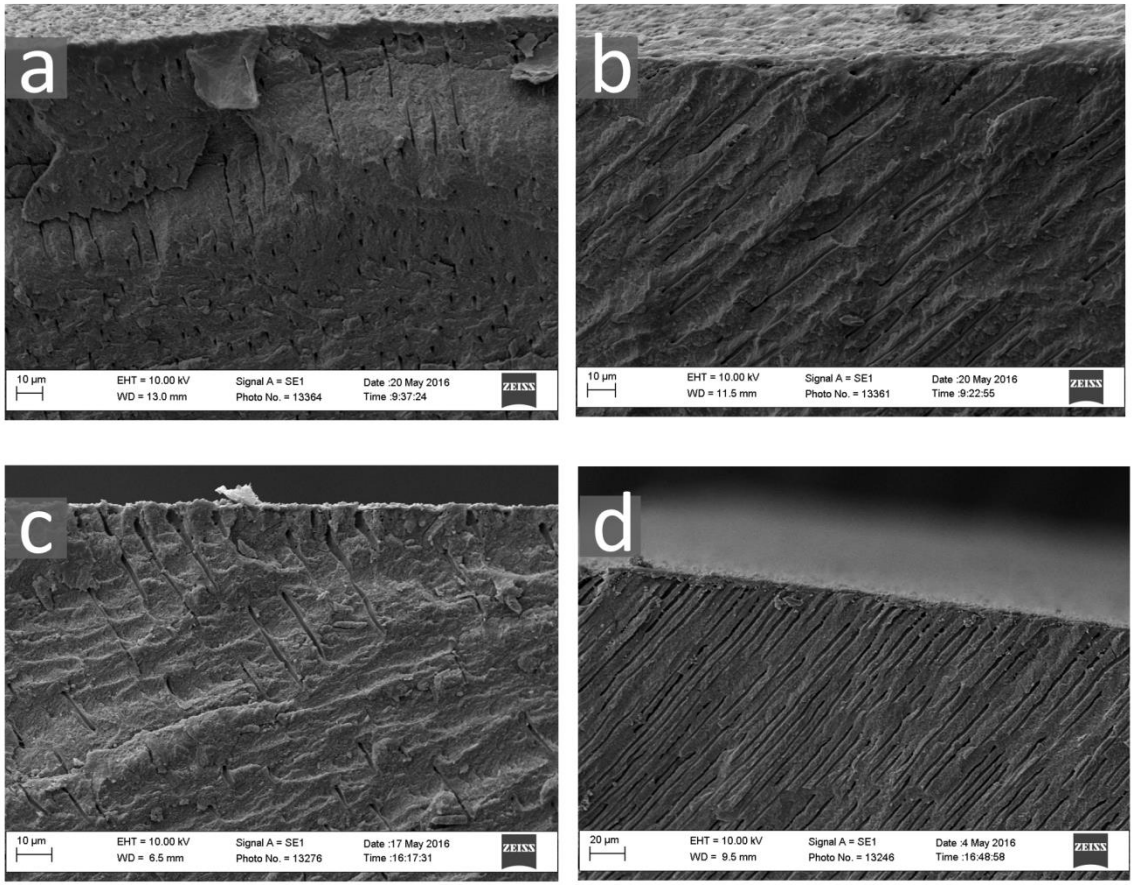

Figure 6.17 SEM images of cross sections of dentine after particle application. Few/no particles can be observed. (a) particles in acetone, no cavitation (b) particles in water, no cavitation (c) particles in acetone, cavitation applied (d) particles in water, cavitation applied.

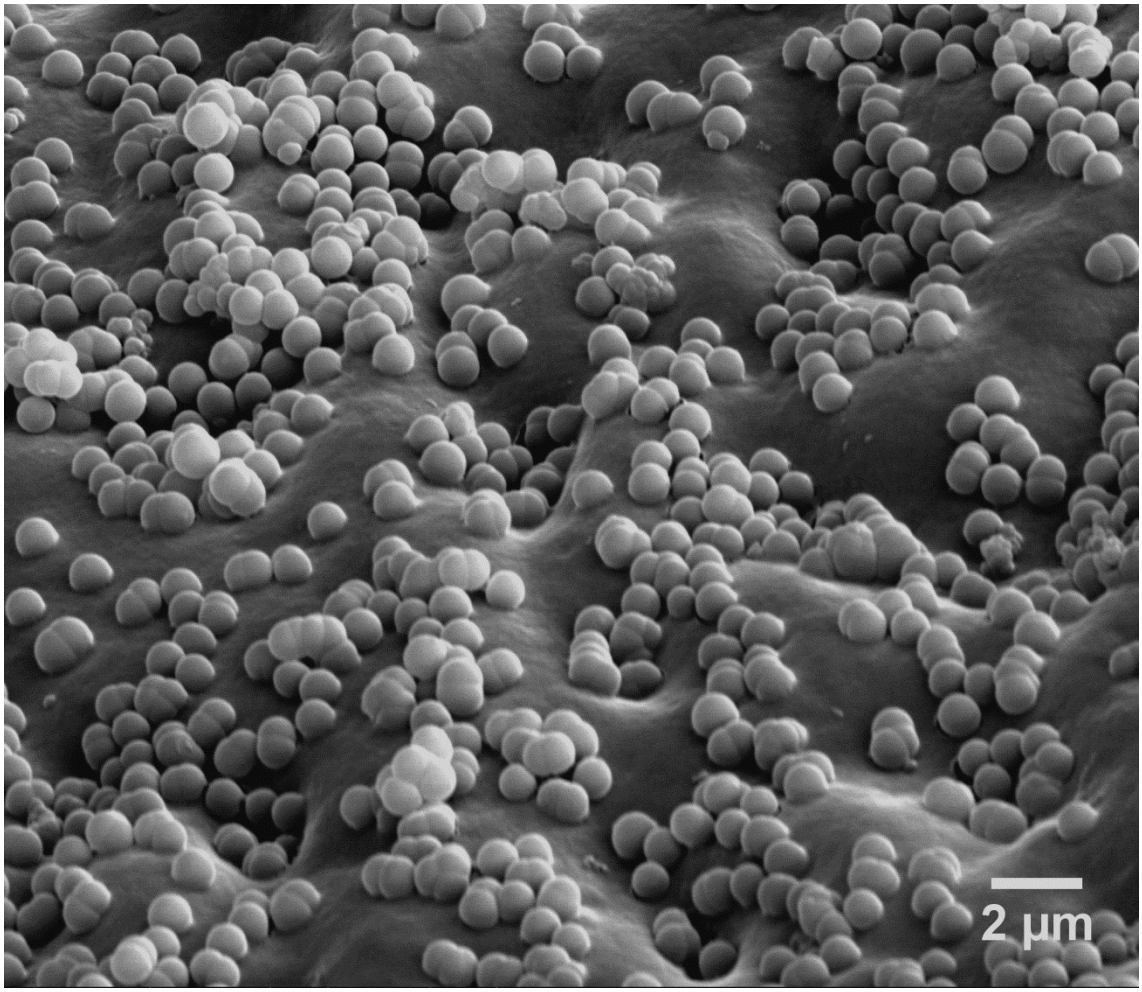

Figure 6.18 SEM image of the dentine surface at an angle of 52^0, showing ridges on the surface. Some of the silica particles are embedded into the dentine.

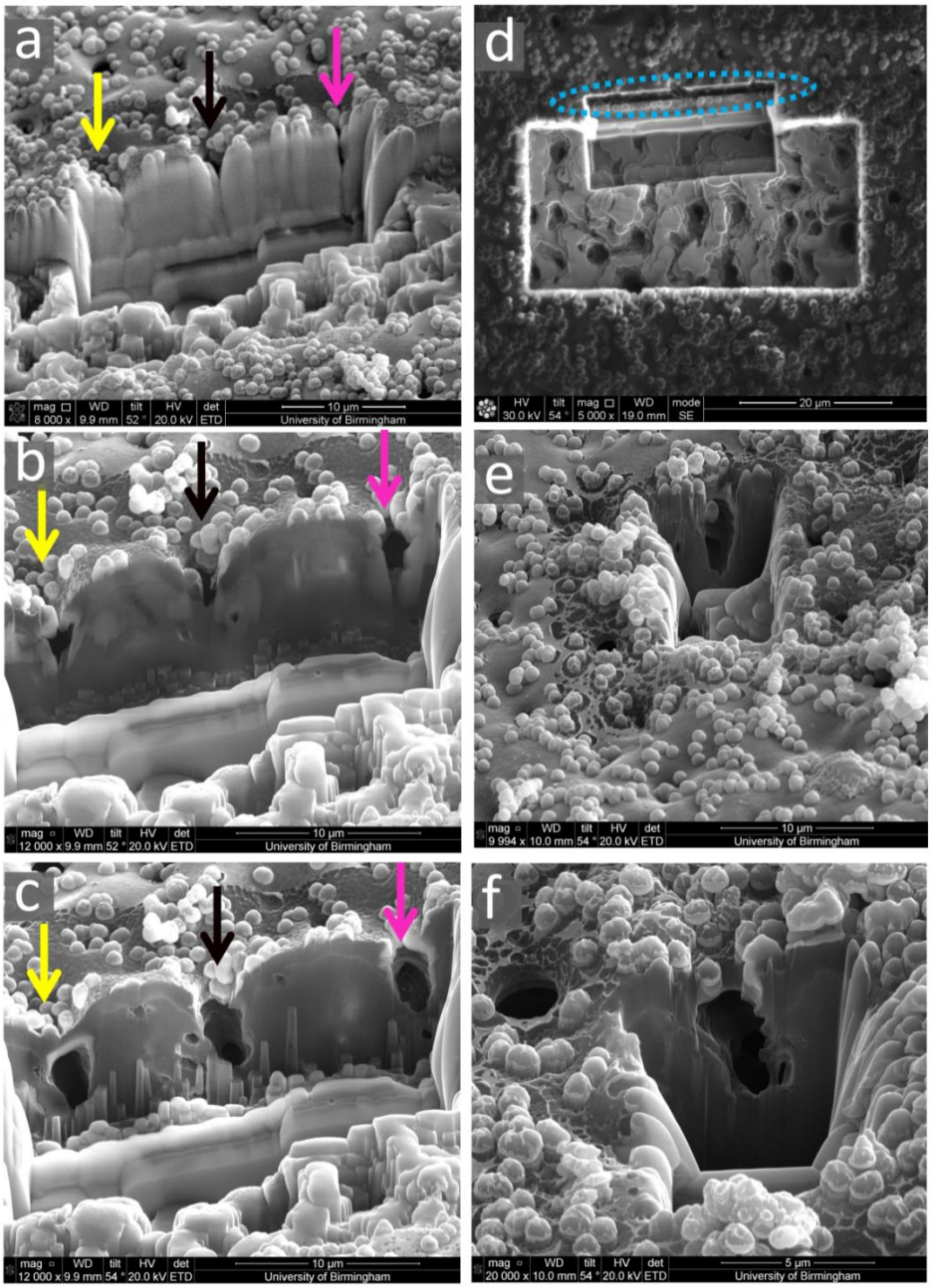

Figure 6.19 (a) (b) and (c): successive FIB-SEM images showing 3 tubules being milled by the FIB beam. The tubules are not occluded under the surface. (d) FIB image showing the trenches milled to acquire images a,b and c. The area shown in a, b and c is circled in blue. (e) and (f): SEM images of single tubules after being milled by the focussed ion beam.

6.4 Discussion

Dentine tubule obstruction using NPs & SMPs is widely researched as a novel method of delivering antimicrobial agents to eliminate bacteria that have entered tubules and also to stop pain from hypersensitivity. However there is no optimal method for rapidly delivering particles into the tubules. Therefore the aim of this study was to research the effect of cavitation from ultrasonic scalers and the effect of acetone on SMP application to dentine.

Particles were observed to occlude and also penetrate into the tubules. This happened for all settings, showing that infiltration can also occur when there is no cavitation. This may be due to the microstreaming fluid flow around the scaler at low power, or from gravitational forces. Keeping the specimens vertical during particle application can confirm this, along with a control where the ultrasonic scaler is not applied.

The depth that the particles had travelled increased by at least two-fold when cavitation was applied (Figure 6.12, Figure 6.13, Figure 6.14, Figure 6.15). This suggests that cavitation can push the SMPs further into the dentinal tubules. It confirms the previous in vitro macro study where Shrestha postulated that cavitation may push objects down a tube and hence in dentinal tubules. In this study the maximum penetration depth observed was 185 µm, whereas Shrestha et al. found particles at up to 1 mm inside the dentinal tubules (2009). This may be because they used an 8 mm diameter disc shaped ultrasound transducer, whereas we have used a clinically available ultrasonic scaler with a smaller area of cavitation (approximately 2 mm x 1mm).

There was no observable difference in the penetration depth when acetone was included in the particle solution, but there were a larger number of tubules which contained particles when acetone was used. Therefore this suggests that acetone can initially aid

in the particle delivery and then cavitation can increase penetration. Further work is needed to confirm these observations. The surface tension of acetone is lower than that of water, therefore more cavitation is expected to occur in acetone. However in this study there were no observable differences in the penetration distance of particles when the cavitation was applied in water or in the acetone solution.

The majority of the silica sub-micron particles had deposited on the surface of the dentine. Many dentine tubules were partially or completely occluded by the particles. Although complete occlusion would be ideal, partial occlusion may increase the potential to reduce pain because of the Hagen-Poiseuille law which shows that the flow rate of a fluid out of a tube of radius r is proportional to r^4. Doubling the tubule radius therefore causes a 16-fold increase in the fluid flow rate in the tubule (Dababneh et al, 1999), so partial occlusion of the tubule is likely to significantly reduce the pain experience of the patient.

Although many tubules were obstructed on the dentine surface, some tubules remained completely exposed. In addition, imaging the dentine cross-section after fracturing the samples showed that most tubules were not occluded with particles. The particles may be collecting around the entrance to the tubules due to the presence of electrostatic charges on the surface, or due to inter-particulate attractive forces (Figure 6.6). The different mineralisation levels between peritubular dentine and intertubular dentine are also likely to affect the particle penetration. Electrostatic charges may be due to the citric acid which is applied to remove the dentine smear layer. Citric acid removes the smear layer and consequently, ions on the dentine surface (e.g. Ca^{2+}, Na^{+}, K^{+}, Mg^{2+}), however, it may not enter into all of the dentinal tubules. By removing ions, citric acid may expose more biological material such as collagen, which may influence the

movement of the particles. Therefore, the ion concentration could be different on the surface dentine compared to the dentine inside the tubules, and the particles may be repelled by the charge inside the tubules. For future work, the ion distribution could be confirmed using SEM combined with energy dispersive x-ray spectroscopy (EDX). In addition, the surface interactions of the particles with the dentine could be altered by coating particles with an anionic material/liquid such as an anionic peptide. Other solvents and demineralising acids could also be investigated instead of acetone and citric acid. The acetone concentration may also be altered to investigate if this affects the particle delivery into the tubules.

The images of the dentine without any particles applied showed that the smear layer had not been completely removed from some tubules (Figure 6.3e). In some cases, the particles which have occluded the tubules appear to be sealed inside a solidified substance, which may be remnants of the smear layer (Figure 6.9b). This appears to be acting as a matrix holding the particles inside the tubules and may be a potential mechanism for retaining particles for prolonged tubule occlusion. Before-after studies using commercially available SEM finder grids to image the same area may be investigated to show whether these particles are retained either after brushing or washing the surface which simulates both tooth brushing and mouth rinsing.

In those cases, where cavitation was applied from the ultrasonic scaler, pits were observed in the dentine surface which had a similar diameter to the silica particles. This may be a result of the particles being accelerated towards the surface due to the cavitation and acoustic microstreaming forces occurring in the liquid. Their high velocity impact caused an indentation in the dentine. There was no observable difference in the pits observed between the acetone solution and the water solution,

suggesting that these solutions do not alter the particle velocity. Such pitting may offer an advantage in that the slurry of liquid and particles will impact on the surface removing debris. The indentations may also be seen as damage to the dentine surface and the resulting micro-roughening might be problematic as it could increase the ability of bacteria to attach the tooth. However the dentine in this study has been polished, whereas in vivo there would be more surface roughness. Therefore the indentations from the particles may not have an adverse effect clinically. The presence of these indentations also confirms that the cavitation can accelerate the particles toward the dentine surface, so it is likely they are also accelerated into the dentinal tubules. This correlates with the finding that there was deeper particle infiltration when cavitation was applied. It is unlikely that the indentations are a result of pitting due to microjet impact from the cavitation because the indentation diameter is similar to the sub-micron particle size, whereas cavitation pitting would be smaller and spread over a wider range of diameters (Jayaprakash et al, 2012).

Particles blocked the opening of dentinal tubules in some cases (Figure 6.16), although FIB SEM showed that often only a single layer of particles were occluding the tubule openings (Figure 6.19). This suggests that the particle obstruction at the surface is caused by the particles depositing in the depressions in the dentine surface.

Such findings open up different avenues of research investigations in the use of sub-micron sized particles on the dentine surface. To increase the particle infiltration frequency and depth, parameters such as the duration of the cavitation, the frequency and power of the ultrasonic scaler and the distance it is held from the dentine surface can be altered.

With FIB SEM the particles can be imaged in the position in which they were originally deposited, but it is difficult to view more than 20 µm inside the tubules due to instrument constraints. SEM imaging after cryo-fracturing the sample enabled viewing along the entire sample thickness, however this method also has limitations. As the samples were only fractured in one location on the sample, only that area was observed. It is possible and likely that particles infiltrated other tubules that could not be imaged. In addition, the sample preparation techniques such as fracturing and drying could have displaced the particles from their original deposition location inside the tubules. In the SEM images of the dentine fracture faces, particles were observed both in the tubules and next to the tubules in the cases where cavitation had been applied. Particles next to the tubules could have been deposited there (1) by being moved from inside the tubules when fracturing, (2) from the operator's gloves during sample preparation, or (3) from the surface of the dentine during fracturing. However as this was observed only when cavitation was applied and not in the other cases, the former explanation is the most likely. This implied that even more particles could have entered the tubules than observed by SEM, but were displaced. Another problem with the fracturing process was that the cut was not always vertical, so in many cases the entire path of the tubules through the dentine could not be seen (Figure 6.16b). To overcome these limitations, further work can be done using a non-destructive technique such as nanotomography (Zanette et al, 2015). Individual sub-micron and nanoparticles could also be imaged in higher resolution using synchrotron imaging, such as x-ray microscopy or holotomography (Elbaum et al, 2007).

Another use of the cavitation from the ultrasonic scaler may be in removing bacteria which have entered into the dentinal tubules. The penetration depth of the cavitation

into the tubules can be investigated and live-dead staining combined with confocal microscopy would help to show if the cavitation has an effect in removing and/or eliminating the bacteria inside the tubules. The scaler could then be used in a 2 step method where the tubules are first cleaned and then the particles are delivered. Optimal settings for cleaning and delivery can be determined using further work.

It was not possible to image fluorescently labelled silica SMPs because the samples were not perfectly horizontal and the shallow depth of focus of optical microscopes did not allow focussing of the dentine surface to take place (as can be seen in Figure 6.11). Claire et al. have successfully imaged the particles on dentine using confocal microscopy (2015), and their sample thickness was ~0.1 mm, whereas in this study the samples were 2mm thick. Therefore for confocal imaging, thinner samples may be more appropriate, although these would not show the maximum penetration depth of the particles.

For future work, high speed imaging and particle imaging velocimetry may be used to show the velocity of the particle flow in the microstreaming currents around the ultrasonic scaler tip, which would give better indications about which distances, powers and frequencies cause the maximum amount of particles to be directed towards the dentinal tubule openings. The penetration of particles was not quantitatively analysed in this study, therefore future work can focus on developing an imaging protocol which enables the penetration distance to be quantified. Finally, the sub-micron particles can be developed to add remineralising or antimicrobial agents.

6.5 Conclusion

The main goal of the current study was to determine whether cavitation from ultrasonic scalers can increase penetration of sub-micron particles into dentinal tubules. This preliminary study has confirmed that the cavitation from ultrasonic scalers may be used to direct sub-micron silica particles which have entered into dentinal tubules. One of the strengths of this investigation is the finding that sub-micron particles were shown to penetrate well over 100 μm into the dentinal tubules, suggesting that tubule occluding substances can be retained for a much longer time. One issue with the current study was that only a small number of dentinal tubules contained sub-micron particles. In addition, the optimal settings for increasing the depth and magnitude of infiltration are not yet clear. The work shows considerable promise although further work is necessary before such a technique may be advocated as a clinical application.

6.6 Acknowledgements

The author would like to thank Theresa Morris from the Centre for Electron Microscopy, University of Birmingham, for conducting the FIB SEM imaging in this study and to Dr David Lewis for assistance and Mark Goodwin for preparing the sub-micron particles used in this study.

7 . CONCLUSIONS

The research objectives were to analyse the cavitation patterns around dental ultrasonic scalers and to investigate the ability of cavitation from ultrasonic scalers to disrupt biofilm and to deliver sub-micron particles into dentine. Previous work studied the cavitation using sonochemiluminescence (Felver et al, 2009; Macedo et al, 2014b; Price et al, 2014; Walmsley et al, 2010; Walmsley et al, 2013). In the present study the cavitation around ultrasonic scaler tips was imaged using high speed cameras and quantitatively analysed. Parameters such as tip shape and power were changed to understand how they affected cavitation production. A range of frame rates were used to study different parts of the cavitation process such as the behaviour of multiple cavitation clouds and the dynamics of an individual bubble's growth and collapse. The first major finding was that cavitation can occur at the free end of ultrasonic scaler tips and its area increases with power and displacement amplitude, making it possible to use ultrasonic scalers to disrupt biofilm in a non-contact mode.

Cavitation bubble dynamics around ultrasonic scalers have been visualised and analysed to show the average sizes of microbubbles and their size and speed during various phases of their life cycle. The speed of individual bubbles reached up to 25 ms^{-1} with maximum radii ranging from 40-80 μm. This work contributes to the literature on

cavitation around ultrasonic scalers by demonstrating that it occurs at the free end of the tip and by developing image analysis protocols to enable quantification.

MicroCT procedures have been developed to quantify artificial biofilm removal in 3D after treatment using cavitation. Previous work used dual energy imaging to segment objects with different attenuation coefficients such as hard and soft tissue (Andrews et al, 2010; Clark et al, 2013). In the current work a similar technique was applied to investigate how biofilm disruption after instrumentation can be evaluated. This study showed that hydrogel on a tooth can be segmented from dual energy microCT images. The research has also shown that the thickness of the hydrogel removed at each point on a model tooth can be calculated using microCT. These findings have significant implications for the understanding of how biofilm is removed from 3D objects. The protocols can be used to test the effect of various periodontal therapy methods in 3D, and can aid in the development of more efficient instrumentation for biofilm removal.

A method was also developed to investigate biofilm disruption at a higher resolution. Biofilm grown on dental implant surfaces was imaged before and after instrumentation to evaluate the effectiveness of cavitation from ultrasonic scalers in biofilm disruption. Earlier studies attempted this but used low resolution light microscopy images and subjective image segmentation methods (Le Guéhennec et al, 2007; Murphy et al, 2015). This study establishes a quantitative framework for detecting biofilm removal using SEM, where individual bacteria in the biofilm and their interaction with the surface can be visualised. A segmentation method based on machine learning was applied to calculate the area removed after instrumentation more accurately than previous studies. These experiments also confirmed that cavitation from ultrasonic

scalers is effective at cleaning biofilm from dental implant surfaces, showing potential for this technique as a new method of dental implant debridement.

Finally, the use of cavitation from ultrasonic scalers to direct sub-micron particles into dentinal tubules was investigated. Recent research has focussed on the use of nanomaterials to treat dentinal hypersensitivity and dentinal caries (Besinis et al, 2015). The present study builds on the work of Shreshta et al. (2009), who showed that cavitation from a transducer caused nanoparticle penetration into dentinal tubules. The current study further demonstrates that cavitation from a clinical ultrasonic scaling instrument also results in penetration and therefore further work could result in this being used as a novel clinical method to direct sub-micron silica particles into dentinal tubules. An implication of this is the possibility that dentinal tubules could be occluded for a longer period of time, resulting in more effective treatment of hypersensitivity. In addition, this method could be used as a novel technique of delivering antimicrobials into dentinal tubules to treat dentinal caries, resulting in less damage to the tooth structure.

7.1 Clinical Relevance

Taken together, these results show that cavitation is able to remove biofilm and deliver particles into dentinal tubules without the scaler tip making contact with the surface. Limitations in this study were the time taken to remove biofilm (approximately 60 s) and the fact that the scaler tip was held very close to the surface (1 mm). These make it difficult for the instrument to be used in a non-contact mode clinically. However, the findings of this thesis could be used to develop a modified device which produces more cavitation that can be used as a more efficient and less damaging method of biofilm removal and also for delivering tubule-occluding agents. The high speed imaging and

analysis methods developed in this study can be used for further research on novel tip designs to determine the optimal design which maximises the cavitation around the ultrasonic scaler tip, and the biofilm quantification procedures established in this study can be used to test the effectiveness of the cavitation on various surfaces. Therefore the findings of this research will help to develop a method of ultrasonic biofilm removal which is effective on dental implants without causing damage, and also effective for biofilm removal subgingivally and from interproximal spaces. This will result in increased prevention of caries, periodontal and peri-implant diseases and also in more effective treatment of these conditions.

These findings have several practical implications. Firstly, they could be of interest to other researchers who can conduct future studies using the protocols developed. For example, the method of imaging and calculating biofilm removal after instrumentation from SEM images can be applied to many studies in biomaterials research which aim to examine cell growth and disruption. The high speed imaging protocols can be used to do further research on cavitation around ultrasonic scalers and to validate theoretical models. The microCT method of imaging hydrogel removal can be developed further to be of benefit to other researchers who are investigating the macroscale removal of biofilm from 3D objects. These findings could also be of interest to industrial manufacturers of ultrasonic scaling and endodontic instruments who are looking to develop their products further.

This work has been presented to clinicians including dental hygienists and periodontists who have expressed that it has been useful to them to visualise the cavitation from ultrasonic scalers and to confirm its presence around the free end of the tip, which is the most clinically relevant part. Although the cavitation currently occurring during clinical

use of the instrument is not sufficient to remove biofilm in a non-contact mode, it has been advocated as an additional form of disruption in addition to the vibrations from the tip. Until now however the cavitation had not been imaged and it was unclear exactly where it occurred, therefore the present study should prove to be particularly valuable to clinicians to help them to understand how they can best use the instrument to make use of the cavitational activity during periodontal therapy.

7.2 Future Work

As a result of this study, the following further research can be conducted:

- High speed imaging:
    - At higher frame rates (~6 million fps) to calculate the velocity of cavitation bubble micro-jets, which may be useful in determining the forces required to detach biofilm
    - At lower frame rates (~50 kfps) to image biofilm removal from tooth models and dental implants to further understand the forces behind ultrasonic biofilm removal
        - Imaging removal of complex multi-species biofilms
        - Imaging removal of hydrated biofilms
    - In this study the pitting caused by cavitation microjets was not specifically investigated, however future research could be done to determine which biofilm removal/tubule occlusion effects are due to microjets and which are due to shock waves emitted by cavitation bubbles. High speed imaging can be used to investigate this.
- Improving the imaging methods to visualise cavitation in the cooling water around the ultrasonic scaler to more accurately resemble the clinical situation

- Mathematical modelling combined with high speed imaging:
    - To validate theoretical predictions of bubble dynamics around ultrasonic scalers and to image cavitation around new tip designs
    - To investigate the damage to soft tissue from cavitation
- PIV to show the velocity and distribution of the microstreaming currents around the scaler tip to explain how biofilm removal and nanoparticle delivery into tubules is affected by the fluid flow and how it can be optimised
- Nanotomography imaging of nanoparticles inside dentinal tubules as a non-destructive method to evaluate tubule penetration distance,
- Improved image segmentation methods
    - Test different classifiers in the trainable Weka Segmentation plugin
    - Optimise the noise reduction and image acquisition settings for microCT imaging of artificial biofilm
- Development of an improved artificial biofilm model for imaging in microCT and investigation of staining techniques for imaging real biofilm in microCT

8. LIST OF REFERENCES

Afkhami, F., Pourhashemi, S. J., Sadegh, M., Salehi, Y. & Fard, M. J. K. (2015) Antibiofilm Efficacy of Silver Nanoparticles as a Vehicle for Calcium Hydroxide Medicament against Enterococcus Faecalis. *Journal of Dentistry*, 43(12): 1573-1579.

Agarwal, A., Jern Ng, W. & Liu, Y. (2014) Removal of Biofilms by Intermittent Low-Intensity Ultrasonication Triggered Bursting of Microbubbles. *Biofouling*, 30(3): 359-365.

Alcoforado, G. A., Rams, T. E., Feik, D. & Slots, J. (1991) Microbial Aspects of Failing Osseointegrated Dental Implants in Humans. *Journal de Parodontologie*, 10(1): 11-18.

Andrews, J. C., Almeida, E., van der Meulen, M. C. H., Alwood, J. S., Lee, C., Liu, Y., Chen, J., Meirer, F., Feser, M., Gelb, J., Rudati, J., Tkachuk, A., Yun, W. & Pianetta, P. (2010) Nanoscale X-Ray Microscopic Imaging of Mammalian Mineralized Tissue. *Microscopy and Microanalysis*, 16(03): 327-336.

Arganda-Carreras, I., Cardona, A., Kaynig, V. & Schindelin, J. (2013, Accessed 07.09.2016) Trainable Weka Segmentation. *http://fiji.sc/Trainable_Weka_Segmentation*.

Arganda-Carreras, I., Sorzano, C. O. S., Marabini, R., Carazo, J. M., Ortiz-De-Solorzano, C. & Kybic, J. (2006) Consistent and Elastic Registration of Histological Sections Using Vector-Spline Regularization, *Computer Vision Approaches to Medical Image Analysis* Springer Berlin Heidelberg, 85-95.

Asegehegn, T. W., Schreiber, M. & Krautz, H. J. (2011) Investigation of Bubble Behavior in Fluidized Beds with and without Immersed Horizontal Tubes Using a Digital Image Analysis Technique. *Powder Technology*, 210(3): 248-260.

Azim, A. A., Aksel, H., Zhuang, T., Mashtare, T., Babu, J. P. & Huang, G. T. J. (2016) Efficacy of 4 Irrigation Protocols in Killing Bacteria Colonized in Dentinal Tubules Examined by a Novel Confocal Laser Scanning Microscope Analysis. *Journal of Endodontics*, 42(6): 928-934.

Baek, S.-H., Shon, W.-J., Bae, K.-S., Kum, K.-Y., Lee, W.-C. & Park, Y.-S. (2012) Evaluation of the Safety and Efficiency of Novel Metallic Ultrasonic Scaler Tip on Titanium Surfaces. *Clinical Oral Implants Research*, 23(11): 1269-1274.

Barrett, J. F. & Keat, N. (2004) Artifacts in Ct: Recognition and Avoidance 1. *Radiographics*, 24(6): 1679-1691.

Besinis, A., De Peralta, T., Tredwin, C. J. & Handy, R. D. (2015) Review of Nanomaterials in Dentistry: Interactions with the Oral Microenvironment, Clinical Applications, Hazards, and Benefits. *ACS Nano*, 9(3): 2255-2289.

Besinis, A., van Noort, R. & Martin, N. (2012) Infiltration of Demineralized Dentin with Silica and Hydroxyapatite Nanoparticles. *Dental Materials*, 28(9): 1012-1023.

Besinis, A., van Noort, R. & Martin, N. (2014) Remineralization Potential of Fully Demineralized Dentin Infiltrated with Silica and Hydroxyapatite Nanoparticles. *Dental Materials*, 30(3): 249-262.

Besinis, A., van Noort, R. & Martin, N. (2016) The Use of Acetone to Enhance the Infiltration of Ha Nanoparticles into a Demineralized Dentin Collagen Matrix. *Dental Materials*, 32(3): 385-393.

Beyenal, H., Donovan, C., Lewandowski, Z. & Harkin, G. (2004) Three-Dimensional Biofilm Structure Quantification. *Journal of Microbiological Methods*, 59(3): 395-413.

Bjarnsholt, T. (2013) The Role of Bacterial Biofilms in Chronic Infections. *APMIS*, 121(s136): 1–58.

Blake, J. R. & Gibson, D. C. (1987) Cavitation Bubbles near Boundaries. *Annual Review of Fluid Mechanics*, 19(1): 99-123.

Blake, J. R., Keen, G. S., Tong, R. P. & Wilson, M. (1999) Acoustic Cavitation: The Fluid Dynamics of Non–Spherical Bubbles. *Philosophical Transactions of the Royal Society of London A: Mathematical, Physical and Engineering Sciences*, 357(1751): 251-267.

Blanken, J., De Moor, R. J. G., Meire, M. & Verdaasdonk, R. (2009) Laser Induced Explosive Vapor and Cavitation Resulting in Effective Irrigation of the Root Canal. Part 1: A Visualization Study. *Lasers in Surgery and Medicine*, 41(7): 514-519.

Boutsioukis, C., Verhaagen, B., Versluis, M., Kastrinakis, E. & Van Der Sluis, L. W. M. (2010) Irrigant Flow in the Root Canal: Experimental Validation of an Unsteady Computational Fluid Dynamics Model Using High-Speed Imaging. *International Endodontic Journal*, 43(5): 393-403.

Brännström, M. (1986) The Hydrodynamic Theory of Dentinal Pain: Sensation in Preparations, Caries, and the Dentinal Crack Syndrome. *Journal of Endodontics*, 12(10): 453-457.

Brennen, C., Reisman, G. & Wang, Y.-C. (1997) Shock Waves in Cloud Cavitation.

Brennen, C. E. (2013) *Cavitation and Bubble Dynamics* Cambridge University Press.

Busciglio, A., Vella, G., Micale, G. & Rizzuti, L. (2008) Analysis of the Bubbling Behaviour of 2d Gas Solid Fluidized Beds: Part I. Digital Image Analysis Technique. *Chemical Engineering Journal*, 140(1): 398-413.

Chahine, G. L., Kapahi, A., Choi, J.-K. & Hsiao, C.-T. (2016) Modeling of Surface Cleaning by Cavitation Bubble Dynamics and Collapse. *Ultrasonics Sonochemistry*, 29: 528-549.

Chan, T. F., Esedoglu, S. & Nikolova, M. (2006) Algorithms for Finding Global Minimizers of Image Segmentation and Denoising Models. *Siam Journal on Applied Mathematics*, 66(5): 1632-1648.

Chen, H., Li, X., Wan, M. & Wang, S. (2007) High-Speed Observation of Cavitation Bubble Cloud Structures in the Focal Region of a 1.2 mhz High-Intensity Focused Ultrasound Transducer. *Ultrasonics Sonochemistry*, 14: 291-297.

Chenouard, N., Smal, I., De Chaumont, F., Maška, M., Sbalzarini, I. F., Gong, Y., Cardinale, J., Carthel, C., Coraluppi, S. & Winter, M. (2014) Objective Comparison of Particle Tracking Methods. *Nature Methods*, 11(3): 281.

Chiang, Y.-C., Lin, H.-P., Chang, H.-H., Cheng, Y.-W., Tang, H.-Y., Yen, W.-C., Lin, P.-Y., Chang, K.-W. & Lin, C.-P. (2014) A Mesoporous Silica Biomaterial for Dental Biomimetic Crystallization. *ACS Nano*, 8(12): 12502-12513.

Claire, S., Walmsley, A. D., Glinton, S., Floyd, H., Sammons, R. & Pikramenou, Z. (2015) The Deposition and Imaging of Silica Sub-Micron Particles in Dentine. *Journal of Dentistry*, 43(10): 1242-1248.

Clark, D. P., Ghaghada, K., Moding, E. J., Kirsch, D. G. & Badea, C. T. (2013) In Vivo Characterization of Tumor Vasculature Using Iodine and Gold Nanoparticles and Dual Energy Micro-Ct. *Physics in Medicine and Biology*, 58(6): 1683.

Clegg, M. S., Vertucci, F. J., Walker, C., Belanger, M. & Britto, L. R. (2006) The Effect of Exposure to Irrigant Solutions on Apical Dentin Biofilms in Vitro. *Journal of Endodontics*, 32(5): 434-437.

Collins, W. J. N. & Walsh, T. F. (1992) *A Handbook for Dental Hygienists* John Wright.

Costerton, J. W., Cheng, K., Geesey, G. G., Ladd, T. I., Nickel, J. C., Dasgupta, M. & Marrie, T. J. (1987) Bacterial Biofilms in Nature and Disease. *Annual Reviews in Microbiology*, 41(1): 435-464.

Costerton, J. W., Geesey, G. G. & Cheng, K. J. (1978). *Scientific American*, 238(1): 86-95.

Costerton, J. W., Stewart, P. S. & Greenberg, E. P. (1999) Bacterial Biofilms: A Common Cause of Persistent Infections. *Science*, 284(5418): 1318-1322.

Cruz, P. C., Andrade, I. M. d., Peracini, A., Souza-Gugelmin, M. C. M. d., Silva-Lovato, C. H., Souza, R. F. d. & Paranhos, H. d. F. O. (2011) The Effectiveness of Chemical Denture Cleansers and Ultrasonic Device in Biofilm Removal from Complete Dentures. *Journal of Applied Oral Science*, 19(6): 668-673.

Dababneh, R. H., Khouri, A. T. & Addy, M. (1999) Dentine Hypersensitivity-an Enigma? A Review of Terminology, Epidemiology, Mechanisms, Aetiology and Management. *British Dental Journal*, 187(11): 606-611.

Davit, Y., Iltis, G., Debenest, G., Veran-Tissoires, S., Wildenschild, D., Gerino, M. & Quintard, M. (2011) Imaging Biofilm in Porous Media Using X-Ray Computed Microtomography. *Journal of Microscopy*, 242(1): 15–25.

Di Bari, S. & Robinson, A. J. (2013) Experimental Study of Gas Injected Bubble Growth from Submerged Orifices. *Experimental Thermal and Fluid Science*, 44: 124-137.

Doinikov, A. A. (2005) Bjerknes Forces and Translational Bubble Dynamics. *Bubble and Particle Dynamics in Acoustic Fields: Modern Trends and Applications*: 95-143.

Donlan, R. M. (2001) Biofilm Formation: A Clinically Relevant Microbiological Process. *Clinical Infectious Diseases*, 33(8): 1387-1392.

Dougherty, R. & Kunzelmann, K.-H. (2007) Computing Local Thickness of 3d Structures with Imagej. *Microscopy and Microanalysis*, 13(S02): 1678-1679.

Duhar, G. & Colin, C. (2006) Dynamics of Bubble Growth and Detachment in a Viscous Shear Flow. *Physics of Fluids (1994-present)*, 18(7): 077101.

Elbaum, R., Tal, E., Perets, A., Oron, D., Ziskind, D., Silberberg, Y. & Wagner, H. (2007) Dentin Micro-Architecture Using Harmonic Generation Microscopy. *Journal of Dentistry*, 35(2): 150-155.

Erriu, M., Blus, C., Szmukler-Moncler, S., Buogo, S., Levi, R., Barbato, G., Madonnaripa, D., Denotti, G., Piras, V. & Orrù, G. (2014) Microbial Biofilm Modulation by Ultrasound: Current Concepts and Controversies. *Ultrasonics Sonochemistry*, 21: 15-22.

Fejerskov, O. & Kidd, E. (2009) *Dental Caries: The Disease and Its Clinical Management* John Wiley & Sons.

Felver, B., King, D. C., Lea, S. C., Price, G. J. & Damien Walmsley, A. (2009) Cavitation Occurrence around Ultrasonic Dental Scalers. *Ultrasonics Sonochemistry*, 16: 692-697.

Felver, B., King, D. C., Lea, S. C., Price, G. J. & Walmsley, A. D. (2008) Scanning Laser Vibrometry and Luminol Photomicrography to Map Cavitational Activity around Ultrasonic Scalers, *Eighth International Conference on Vibration Measurements by Laser Techniques: Advances and Applications*. 2008. International Society for Optics and Photonics.

Fox, S. C., Moriarty, J. D. & Kusy, R. P. (1990) The Effects of Scaling a Titanium Implant Surface with Metal and Plastic Instruments: An in Vitro Study. *Journal of Periodontology*, 61(8): 485-490.

Fricke, K., Koban, I., Tresp, H., Jablonowski, L., Schröder, K., Kramer, A., Weltmann, K.-D., von Woedtke, T. & Kocher, T. (2012) Atmospheric Pressure Plasma: A High-Performance Tool for the Efficient Removal of Biofilms. *PloS One*, 7(8): e42539.

Gaitan, D. F., Crum, L. A., Church, C. C. & Roy, R. A. (1992) Sonoluminescence and Bubble Dynamics for a Single, Stable, Cavitation Bubble. *The Journal of the Acoustical Society of America*, 91(6): 3166-3183.

Garbin, V., Cojoc, D., Ferrari, E., Di Fabrizio, E., Overvelde, M., Van Der Meer, S., De Jong, N., Lohse, D. & Versluis, M. (2007) Changes in Microbubble Dynamics near a Boundary Revealed by Combined Optical Micromanipulation and High-Speed Imaging. *Applied Physics Letters*, 90(11): 114103.

Gjersing, E. L., Codd, S. L., Seymour, J. D. & Stewart, P. S. (2005) Magnetic Resonance Microscopy Analysis of Advective Transport in a Biofilm Reactor. *Biotechnology and Bioengineering*, 89(7): 822–834.

Gnanaskandan, A. & Mahesh, K. (2016) Large Eddy Simulation of the Transition from Sheet to Cloud Cavitation over a Wedge. *International Journal of Multiphase Flow*, 83: 86-102.

Goldman, L. W. (2007) Principles of Ct: Radiation Dose and Image Quality. *Journal of Nuclear Medicine Technology*, 35(4): 213-225.

Gustumhaugen, E., Lönn-Stensrud, J., Scheie, A. A., Lyngstadaas, S. P., Ekfeldt, A. & Taxt-Lamolle, S. (2014) Effect of Chemical and Mechanical Debridement Techniques on Bacterial Re-Growth on Rough Titanium Surfaces: An in Vitro Study. *Clinical Oral Implants Research*, 25(6): 707-713.

Hadi, R., Vickery, K., Deva, A. & Charlton, T. (2010) Biofilm Removal by Medical Device Cleaners: Comparison of Two Bioreactor Detection Assays. *Journal of Hospital Infection*, 74(2): 160-167.

Hägi, T. T., Klemensberger, S., Bereiter, R., Nietzsche, S., Cosgarea, R., Flury, S., Lussi, A., Sculean, A. & Eick, S. (2015) A Biofilm Pocket Model to Evaluate Different

Non-Surgical Periodontal Treatment Modalities in Terms of Biofilm Removal and Reformation, Surface Alterations and Attachment of Periodontal Ligament Fibroblasts. *PloS One*, 10(6): e0131056.

Haisch, C. & Niessner, R. (2007) Visualisation of Transient Processes in Biofilms by Optical Coherence Tomography. *Water Research*, 41(11): 2467-2472.

Hayat, M. A. (1974) *Principles and Techniques of Scanning Electron Microscopy. Biological Applications. Volume 1* Van Nostrand Reinhold Company.

Heidrich, M., Kühnel, M. P., Kellner, M., Lorbeer, R.-A., Lange, T., Winkel, A., Stiesch, M., Meyer, H. & Heisterkamp, A. (2011) 3d Imaging of Biofilms on Implants by Detection of Scattered Light with a Scanning Laser Optical Tomograph. *Biomedical Optics Express*, 2(11): 2982-2994.

Howlin, R. P., Fabbri, S., Offin, D. G., Symonds, N., Kiang, K. S., Knee, R. J., Yoganantham, D. C., Webb, J. S., Birkin, P. R. & Leighton, T. G. (2015) Removal of Dental Biofilms with an Ultrasonically Activated Water Stream. *Journal of Dental Research*: 0022034515589284.

Iltis, G. C. (2013) Visualization and Characterization of Biofilm Spatial Distribution in Porous Media Using X-Ray Computed Microtomography.

Iltis, G. C., Armstrong, R. T., Jansik, D. P., Wood, B. D. & Wildenschild, D. (2011) Imaging Biofilm Architecture within Porous Media Using Synchrotron-Based X-Ray Computed Microtomography. *Water Resources Research*, 47(2): W02601.

Inaba, T., Ichihara, T., Yawata, Y., Toyofuku, M., Uchiyama, H. & Nomura, N. (2013) Three-Dimensional Visualization of Mixed Species Biofilm Formation Together with Its Substratum. *Microbiology and Immunology*.

Jayaprakash, A., Choi, J.-K., Chahine, G. L., Martin, F., Donnelly, M., Franc, J.-P. & Karimi, A. (2012) Scaling Study of Cavitation Pitting from Cavitating Jets and Ultrasonic Horns. *Wear*, 296(1): 619-629.

Jiang, L.-M., Verhaagen, B., Versluis, M. & van der Sluis, L. W. (2010) Evaluation of a Sonic Device Designed to Activate Irrigant in the Root Canal. *Journal of Endodontics*, 36(1): 143-146.

Jin, Y. & Yip, H.-K. (2002) Supragingival Calculus: Formation and Control. *Critical Reviews in Oral Biology & Medicine*, 13: 426-441.

John, G., Becker, J. & Schwarz, F. (2014) Rotating Titanium Brush for Plaque Removal from Rough Titanium Surfaces–an in Vitro Study. *Clinical Oral Implants Research*, 25(7): 838-842.

Jones, R., Aparicio, C., Chityala, R., Chen, R., Fok, A. & Rudney, J. (2012) Assessing Ex Vivo Dental Biofilms and in Vivo Composite Restorations Using Cross-Polarization Optical Coherence Tomography, *International Society for Optics and Photonics*. 2012. SPIE BiOS.

Kawashima, H., Sato, S., Kishida, M., Yagi, H., Matsumoto, K. & Ito, K. (2007) Treatment of Titanium Dental Implants with Three Piezoelectric Ultrasonic Scalers: An in Vivo Study. *Journal of Periodontology*, 78(9): 1689-1694.

Kaynig, V., Fuchs, T. & Buhmann, J. M. (2010) Neuron Geometry Extraction by Perceptual Grouping in Sstem Images 2010. IEEE.

Khambay, B. S. & Walmsley, A. D. (1999) Acoustic Microstreaming: Detection and Measurement around Ultrasonic Scalers. *Journal of Periodontology*, 70(6): 626-636.

Kirk, S. E., Skepper, J. N. & Donald, A. M. (2009) Application of Environmental Scanning Electron Microscopy to Determine Biological Surface Structure. *Journal of Microscopy*, 233(2): 205-224.

Kite, P., Eastwood, K., Sugden, S. & Percival, S. L. (2004) Use of in Vivo-Generated Biofilms from Hemodialysis Catheters to Test the Efficacy of a Novel Antimicrobial Catheter Lock for Biofilm Eradication in Vitro. *Journal of Clinical Microbiology*, 42(7): 3073-3076.

Koburger, S., Bannerman, A., Grover, L. M., Müller, F. A., Bowen, J. & Paxton, J. Z. (2013) A Novel Method for Monitoring Mineralisation in Hydrogels at the Engineered Hard–Soft Tissue Interface. *Biomaterials Science*, 2(1): 41-51.

Koh, M., Park, J.-B., Jang, Y.-J. & Ko, Y. (2013) The Effect of Pretreating Resorbable Blast Media Titanium Discs with an Ultrasonic Scaler or Toothbrush on the Bacterial Removal Efficiency of Brushing. *Journal of Periodontal and Implant Science*, 43(6): 301-307.

Kondo, Y., Takubo, K., Tominaga, H., Hirose, R., Tokuoka, N., Kawaguchi, Y., Takaie, Y. & Ozaki, A. Development of "Hypervision Hpv-X" High-Speed Video Camera. *Shimadzu Review*, 69: 285-291.

Kremkau, F. W. (2001) *Diagnostic Ultrasound: Principles and Instruments* WB Saunders Company.

Laird, W. R. E. & Walmsley, A. D. (1991) Ultrasound in Dentistry. Part 1—Biophysical Interactions. *Journal of Dentistry*, 19(1): 14–17.

Lang, N. P. & Lindhe, J. (2015) *Clinical Periodontology and Implant Dentistry, 2 Volume Set* John Wiley & Sons.

Lauterborn, W., Kurz, T., Geisler, R., Schanz, D. & Lindau, O. (2007) Acoustic Cavitation, Bubble Dynamics and Sonoluminescence. *Ultrasonics Sonochemistry*, 14: 484-491.

Le Guéhennec, L., Soueidan, A., Layrolle, P. & Amouriq, Y. (2007) Surface Treatments of Titanium Dental Implants for Rapid Osseointegration. *Dental Materials*, 23(7): 844-854.

Lea, S. C., Price, G. J. & Walmsley, A. D. (2005) A Study to Determine Whether Cavitation Occurs around Dental Ultrasonic Scaling Instruments. *Ultrasonics Sonochemistry*, 12: 233–236.

Lea, S. C. & Walmsley, A. D. (2009) Mechano-Physical and Biophysical Properties of Power-Driven Scalers: Driving the Future of Powered Instrument Design and Evaluation. *Periodontology 2000*, 51(1): 63-78.

Leighton, T. G., Walton, A. J. & Pickworth, M. J. W. (1990) Primary Bjerknes Forces. *European Journal of Physics*, 11(1): 47.

Lewis, D. J., Dore, V., Goodwin, M. J., Savage, A. C., Nash, G. B., Angeli, P. & Pikramenou, Z. (2012) Luminescent Ruthenium (Ii) Tris-Bipyridyl Complex Caged in Nanoscale Silica for Particle Velocimetry Studies in Microchannels. *Measurement Science and Technology*, 23(8): 084004.

Li, J., Hirota, K., Goto, T., Yumoto, H., Miyake, Y. & Ichikawa, T. (2012) Biofilm Formation of Candida Albicans on Implant Overdenture Materials and Its Removal. *Journal of Dentistry*, 40(8): 686-692.

Lim, K. Y., Quinto-Su, P. A., Klaseboer, E., Khoo, B. C., Venugopalan, V. & Ohl, C.-D. (2010) Nonspherical Laser-Induced Cavitation Bubbles. *Physical Review E*, 81(1): 016308.

Lin, J., Shen, Y. & Haapasalo, M. (2013) A Comparative Study of Biofilm Removal with Hand, Rotary Nickel-Titanium, and Self-Adjusting File Instrumentation Using a Novel in Vitro Biofilm Model. *Journal of Endodontics*, 39(5): 658-663.

Louropoulou, A., Slot, D. E. & Van der Weijden, F. (2014) The Effects of Mechanical Instruments on Contaminated Titanium Dental Implant Surfaces: A Systematic Review. *Clinical Oral Implants Research*, 25(10): 1149-1160.

Love, R. M. & Jenkinson, H. F. (2002) Invasion of Dentinal Tubules by Oral Bacteria. *Critical Reviews in Oral Biology & Medicine*, 13(2): 171-183.

Macaskie, L. E., Yong, P., Paterson-Beedle, M., Thackray, A. C., Marquis, P. M., Sammons, R. L., Nott, K. P. & Hall, L. D. (2005) A Novel Non Line-of-Sight Method for Coating Hydroxyapatite onto the Surfaces of Support Materials by Biomineralization. *Journal of Biotechnology*, 118(2): 187-200.

Macedo, R. G., Robinson, J. P., Verhaagen, B., Walmsley, A. D., Versluis, M., Cooper, P. R. & van der Sluis, L. W. M. (2014a) A Novel Methodology Providing Insights into Removal of Biofilm-Mimicking Hydrogel from Lateral Morphological Features of the Root Canal During Irrigation Procedures. *International Endodontic Journal*, 47(11): 1040-1051.

Macedo, R. G., Verhaagen, B., Fernandez Rivas, D., Gardeniers, J. G. E., van der Sluis, L. W. M., Wesselink, P. R. & Versluis, M. (2014b) Sonochemical and High-Speed Optical Characterization of Cavitation Generated by an Ultrasonically Oscillating Dental File in Root Canal Models. *Ultrasonics Sonochemistry*, 21: 324-335.

Mann, M., Parmar, D., Walmsley, A. D. & Lea, S. C. (2012) Effect of Plastic-Covered Ultrasonic Scalers on Titanium Implant Surfaces. *Clinical Oral Implants Research*, 23(1): 76-82.

Manz, B., Volke, F., Goll, D. & Horn, H. (2003) Measuring Local Flow Velocities and Biofilm Structure in Biofilm Systems with Magnetic Resonance Imaging (Mri). *Biotechnology and Bioengineering*, 84(4): 424-432.

Marsh, P. D., Martin, M. V., Lewis, M. A. O. & Williams, D. (2009) *Oral Microbiology* Elsevier Health Sciences.

Matsumoto, H., Yoshimine, Y. & Akamine, A. (2011) Visualization of Irrigant Flow and Cavitation Induced by Er: Yag Laser within a Root Canal Model. *Journal of Endodontics*, 37(6): 839-843.

Matsumoto, Y. & Yoshizawa, S. (2005) Behaviour of a Bubble Cluster in an Ultrasound Field. *International Journal for Numerical Methods in Fluids*, 47(6-7): 591-601.

Maurus, R., Ilchenko, V. & Sattelmayer, T. (2004) Automated High-Speed Video Analysis of the Bubble Dynamics in Subcooled Flow Boiling. *International Journal of Heat and Fluid Flow*, 25(2): 149-158.

Meijering, E., Dzyubachyk, O. & Smal, I. (2012) Methods for Cell and Particle Tracking. *Methods in Enzymology*, 504(9): 183-200.

Meyer, H., Antonopoulos, G., Heidrich, M., Lorbeer, R. A., Kellner, M., Winkel, A., Stiesch, M., Kühnel, M. P., Ochs, M. & Ripken, T. (2013) Scanning Laser Optical Tomography: A Highly Efficient Volumetric Imaging Technique for Mesoscopic Specimens, *European Conference on Biomedical Optics*. 2013. Optical Society of America.

Mitragotri, S. (2005) Healing Sound: The Use of Ultrasound in Drug Delivery and Other Therapeutic Applications. *Nature Reviews Drug Discovery*, 4(3): 255-260.

Molina, B., Glickman, G., Vandrangi, P. & Khakpour, M. (2015) Evaluation of Root Canal Debridement of Human Molars Using the Gentlewave System. *Journal of Endodontics*, 41(10): 1701-1705.

Monroe, D. (2007) Looking for Chinks in the Armor of Bacterial Biofilms. *PLoS Biology*, 5(11): e307.

Mueller, L. N., De Brouwer, J. F. C., Almeida, J. S., Stal, L. J. & Xavier, J. B. (2006) Analysis of a Marine Phototrophic Biofilm by Confocal Laser Scanning Microscopy Using the New Image Quantification Software Phlip. *BMC Ecology*, 6(1): 1.

Murphy, J., Ali, M. J. & Psaltis, A. J. (2015) Biofilm Quantification on Nasolacrimal Silastic Stents after Dacryocystorhinostomy. *Ophthalmic Plastic and Reconstructive Surgery*, 31(5): 396-400.

Nance, W. C., Dowd, S. E., Samarian, D., Chludzinski, J., Delli, J., Battista, J. & Rickard, A. H. (2013) A High-Throughput Microfluidic Dental Plaque Biofilm System to Visualize and Quantify the Effect of Antimicrobials. *Journal of Antimicrobial Chemotherapy*, 68(11): 2550-2560.

Neu, T. R. & Lawrence, J. R. (2015) Innovative Techniques, Sensors, and Approaches for Imaging Biofilms at Different Scales. *Trends in Microbiology*, 23(4): 233-242.

Neu, T. R., Manz, B., Volke, F., Dynes, J. J., Hitchcock, A. P. & Lawrence, J. R. (2010) Advanced Imaging Techniques for Assessment of Structure, Composition and Function in Biofilm Systems. *FEMS Microbiology Ecology*, 72(1): 1–21.

Oberdörster, G. (2000) Pulmonary Effects of Inhaled Ultrafine Particles. *International Archives of Occupational and Environmental Health*, 74(1): 1-8.

Ohl, S. W., Shrestha, A., Khoo, B. C. & Kishen, A. (2010) Characterizing Bubble Dynamics Created by High-Intensity Focused Ultrasound for the Delivery of Antibacterial Nanoparticles into a Dental Hard Tissue. *Proceedings of the Institution of Mechanical Engineers, Part H: Journal of Engineering in Medicine*, 224(11): 1285-1296.

Park, J.-B., Jang, Y. J., Choi, B.-K., Kim, K.-K. & Ko, Y. (2013) Treatment with Various Ultrasonic Scaler Tips Affects Efficiency of Brushing of Sla Titanium Discs:. *Journal of Craniofacial Surgery*, 24(2): e119-e123.

Pecheva, E., Sammons, R. & Walmsley, A. (2016) The Performance Characteristics of a Piezoelectric Ultrasonic Dental Scaler. *Medical Engineering and Physics*, 38(2): 199-203.

Peeters, H. H., De Moor, R. J. & Suharto, D. (2015) Visualization of Removal of Trapped Air from the Apical Region in Simulated Root Canals by Laser-Activated Irrigation Using an Er, Cr: Ysgg Laser. *Lasers in Medical Science*, 30(6): 1683-1688.

Peeters, H. H., Iskandar, B., Suardita, K. & Suharto, D. (2014) Visualization of Removal of Trapped Air from the Apical Region of the Straight Root Canal Models Generating 2-Phase Intermittent Counter Flow During Ultrasonically Activated Irrigation. *Journal of Endodontics*, 40(6): 857-861.

Philipp, A. & Lauterborn, W. (1998) Cavitation Erosion by Single Laser-Produced Bubbles. *Journal of Fluid Mechanics*, 361: 75-116.

Pishchalnikov, Y. A., Sapozhnikov, O. A., Bailey, M. R., Williams, J. C., Cleveland, R. O., Colonius, T., Crum, L. A., Evan, A. P. & McAteer, J. A. (2003) Cavitation Bubble Cluster Activity in the Breakage of Kidney Stones by Lithotripter Shockwaves. *Journal of Endourology*, 17(7): 435-446.

Plesset, M. S. & Prosperetti, A. (1977) Bubble Dynamics and Cavitation. *Annual Review of Fluid Mechanics*, 9(1): 145–185.

Powers, J. M. & Wataha, J. C. (2014) *Dental Materials-: Properties and Manipulation* Elsevier Health Sciences.

Price, G. J., Tiong, T. J. & King, D. C. (2014) Sonochemical Characterisation of Ultrasonic Dental Descalers. *Ultrasonics Sonochemistry*, 21: 2052-2060.

Qian, Z., Stoodley, P. & Pitt, W. G. (1996) Effect of Low-Intensity Ultrasound Upon Biofilm Structure from Confocal Scanning Laser Microscopy Observation. *Biomaterials*, 17(20): 1975-1980.

Ramage, G., Martínez, J. P. & López-Ribot, J. L. (2006) Candida Biofilms on Implanted Biomaterials: A Clinically Significant Problem. *FEMS Yeast Research*, 6(7): 979-986.

Reisman, G., Wang, Y.-C. & Brennen, C. (1998) Observations of Shock Waves in Cloud Cavitation. *Journal of Fluid Mechanics*, 355: 255-283.

Riederer, S. J. & Mistretta, C. (1977) Selective Iodine Imaging Using K-Edge Energies in Computerized X-Ray Tomography. *Medical Physics*, 4(6): 474-481.

Rimondini, L., Fare, S., Brambilla, E. & Felloni, A. (1997) The Effect of Surface Roughness on Early in Vivo Plaque Colonization on Titanium. *Journal of Periodontology*, 68(6): 556-562.

Rivas, D. F., Verhaagen, B., Seddon, J. R. T., Zijlstra, A. G., Jiang, L.-M., van der Sluis, L. W. M., Versluis, M., Lohse, D. & Gardeniers, H. J. G. E. (2012) Localized Removal of Layers of Metal, Polymer, or Biomaterial by Ultrasound Cavitation Bubbles. *Biomicrofluidics*, 6(3): 034114.

Rmaile, A., Carugo, D., Capretto, L., Aspiras, M., De Jager, M., Ward, M. & Stoodley, P. (2014) Removal of Interproximal Dental Biofilms by High-Velocity Water Microdrops. *Journal of Dental Research*, 93: 68-73.

Roberts-Harry, E. A. & Clerehugh, V. (2000) Subgingival Calculus: Where Are We Now? A Comparative Review. *Journal of Dentistry*, 28(2): 93-102.

Robinson, J. P. (2014) *Imaging of Root Canal Preparation* University of Birmingham.

Rosen, P., Clem, D., Cochran, D., Froum, S., McAllister, B. & Renvert, S. (2013) Peri-Implant Mucositis and Peri-Implantitis: A Current Understanding of Their Diagnoses and Clinical Implications. *Journal of Periodontology*, 84(4): 436-443.

Salles, A. E. S., Macedo, L. D., Fernandes, R. A. G., Silva-Lovato, C. H. & Paranhos, H. d. F. O. (2007) Comparative Analysis of Biofilm Levels in Complete Upper and Lower Dentures after Brushing Associated with Specific Denture Paste and Neutral Soap. *Gerodontology*, 24(4): 217-223.

Samiei, M., Farjami, A., Dizaj, S. M. & Lotfipour, F. (2016) Nanoparticles for Antimicrobial Purposes in Endodontics: A Systematic Review of in Vitro Studies. *Materials Science and Engineering: C*, 58: 1269-1278.

Sammons, R., Wang, A., Thackray, A., Yong, P., Kuboki, Y., Ametani, A. & Macaskie, L. (2010) Bacterial Calcification: Friend or Foe? *Nano Biomedicine*, 2(2): 71-80.

Santini, M., Guilizzoni, M., Lorenzi, M., Atanassov, P., Marsili, E., Fest-Santini, S., Cristiani, P. & Santoro, C. (2015) Three-Dimensional X-Ray Microcomputed Tomography of Carbonates and Biofilm on Operated Cathode in Single Chamber Microbial Fuel Cell. *Biointerphases*, 10(3): 031009.

Schindelin, J., Arganda-Carreras, I., Frise, E., Kaynig, V., Longair, M., Pietzsch, T., Preibisch, S., Rueden, C., Saalfeld, S., Schmid, B., Tinevez, J.-Y., White, D. J., Hartenstein, V., Eliceiri, K., Tomancak, P. & Cardona, A. (2012) Fiji: An Open-Source Platform for Biological-Image Analysis. *Nature Methods*, 9(7): 676-682.

Schwarz, F., Papanicolau, P., Rothamel, D., Beck, B., Herten, M. & Becker, J. (2006) Influence of Plaque Biofilm Removal on Reestablishment of the Biocompatibility of Contaminated Titanium Surfaces. *Journal of Biomedical Materials Research Part A*, 77(3): 437-444.

Sedgley, C., Applegate, B., Nagel, A. & Hall, D. (2004) Real-Time Imaging and Quantification of Bioluminescent Bacteria in Root Canals in Vitro. *Journal of Endodontics*, 30(12): 893-898.

Sensen, C. W. & Hallgrimsson, B. (2008) *Advanced Imaging in Biology and Medicine: Technology, Software Environments, Applications* Springer Science & Business Media.

Seymour, J. D., Codd, S. L., Gjersing, E. L. & Stewart, P. S. (2004) Magnetic Resonance Microscopy of Biofilm Structure and Impact on Transport in a Capillary Bioreactor. *Journal of Magnetic Resonance*, 167(2): 322-327.

Shemesh, H., Goertz, D. E., van der Sluis, L. W. M., de Jong, N., Wu, M. K. & Wesselink, P. R. (2007) High Frequency Ultrasound Imaging of a Single-Species Biofilm. *Journal of Dentistry*, 35(8): 673-678.

Shpak, O., Stricker, L., Versluis, M. & Lohse, D. (2013) The Role of Gas in Ultrasonically Driven Vapor Bubble Growth. *Physics in Medicine and Biology*, 58(8): 2523.

Shrestha, A., Fong, S.-W., Khoo, B.-C. & Kishen, A. (2009) Delivery of Antibacterial Nanoparticles into Dentinal Tubules Using High-Intensity Focused Ultrasound. *Journal of Endodontics*, 35(7): 1028-1033.

Stadtländer, C. (2007) Scanning Electron Microscopy and Transmission Electron Microscopy of Mollicutes: Challenges and Opportunities. *Modern Research and Educational Topics in Microscopy*, 1: 122-131.

Stock, S. R. (2008) *Microcomputed Tomography: Methodology and Applications* Crc Press.

Stoodley, P., Sauer, K., Davies, D. G. & Costerton, J. W. (2002) Biofilms as Complex Differentiated Communities. *Annual Reviews in Microbiology*, 56(1): 187-209.

Suslick, K. S. & Flannigan, D. J. (2008) Inside a Collapsing Bubble: Sonoluminescence and the Conditions During Cavitation. *Annual Review of Physical Chemistry*, 59: 659–683.

Szabo, T. L. (2004) *Diagnostic Ultrasound Imaging: Inside Out* Academic Press.

Tawakoli, P. N., Sauer, B., Becker, K., Buchalla, W. & Attin, T. (2015) Interproximal Biofilm Removal by Intervallic Use of a Sonic Toothbrush Compared to an Oral Irrigation System. *BMC Oral Health*, 15(1): 91.

Tho, P., Manasseh, R. & Ooi, A. (2007) Cavitation Microstreaming Patterns in Single and Multiple Bubble Systems. *Journal of Fluid Mechanics*, 576: 191–233.

Thomas, M., Marshall, M. J., Miller, E. A., Kuprat, A. P., Kleese-van Dam, K. & Carson, J. P. (2014) 3d Imaging of Microbial Biofilms: Integration of Synchrotron Imaging and an Interactive Visualization Interface, *2014 36th Annual International Conference of the IEEE Engineering in Medicine and Biology Society*. IEEE.

Thoroddsen, S. T., Etoh, T. G. & Takehara, K. (2008) High-Speed Imaging of Drops and Bubbles. *Annual Review of Fluid Mechanics*, 40: 257-285.

Tian, L., Peng, C., Shi, Y., Guo, X., Zhong, B., Qi, J., Wang, G., Cai, Q. & Cui, F. (2014) Effect of Mesoporous Silica Nanoparticles on Dentinal Tubule Occlusion: An in Vitro Study Using Sem and Image Analysis. *Dental Materials Journal*, 33(1): 125-132.

Tomita, Y., Robinson, P., Tong, R. & Blake, J. (2002) Growth and Collapse of Cavitation Bubbles near a Curved Rigid Boundary. *Journal of Fluid Mechanics*, 466: 259-283.

Tuziuti, T., Hatanaka, S.-i., Yasui, K., Kozuka, T. & Mitome, H. (2002) Effect of Ambient-Pressure Reduction on Multibubble Sonochemiluminescence. *The Journal of Chemical Physics*, 116(14): 6221-6227.

Vaidya, K., Hatfield, K., Helguera, M. & Pichichero, M. (2011) High Frequency Ultrasound Imaging and Characterization of Biofilms, *International Ultrasonics Symposium*. IEEE.

van Wijngaarden, L. (2016) Mechanics of Collapsing Cavitation Bubbles. *Ultrasonics Sonochemistry*, 29: 524-527.

Verhaagen, B., Boutsioukis, C., Heijnen, G. L., Van der Sluis, L. W. M. & Versluis, M. (2012) Role of the Confinement of a Root Canal on Jet Impingement During Endodontic Irrigation. *Experiments in Fluids*, 53(6): 1841-1853.

Verhaagen, B. & Rivas, D. F. (2016) Measuring Cavitation and Its Cleaning Effect. *Ultrasonics Sonochemistry*, 29: 619-628.

Versluis, M. (2013) High-Speed Imaging in Fluids. *Experiments in Fluids*, 54(2): 1-35.

Vickery, K., Pajkos, A. & Cossart, Y. (2004) Removal of Biofilm from Endoscopes: Evaluation of Detergent Efficiency. *American Journal of Infection Control*, 32(3): 170-176.

Walmsley, A. D. (1988) Applications of Ultrasound in Dentistry. *Ultrasound in Medicine & Biology*, 14(1): 7-14.

Walmsley, A. D., Felver, B., Lea, S. C., Lumley, P. J., King, D. C. & Price, G. J. (2010) Identifying Cavitation around Dental Ultrasonic Instruments, *39th International Congress on Noise Control Engineering*. 2010. INTER-NOISE.

Walmsley, A. D., Laird, W. R. E. & Lumley, P. J. (1992) Ultrasound in Dentistry. Part 2—Periodontology and Endodontics. *Journal of Dentistry*, 20(1): 11–17.

Walmsley, A. D., Lea, S. C., Felver, B., King, D. C. & Price, G. J. (2013) Mapping Cavitation Activity around Dental Ultrasonic Tips. *Clinical Oral Investigations*, 17(4): 1227-1234.

Walmsley, A. D., Lea, S. C., Landini, G. & Moses, A. J. (2008) Advances in Power Driven Pocket/Root Instrumentation. *Journal of Clinical Periodontology*, 35(s8): 22-28.

Walmsley, A. D., Walsh, T. F., Lard, W. R. E. & Williams, A. R. (1990) Effects of Cavitational Activity on the Root Surface of Teeth During Ultrasonic Scaling. *Journal of Clinical Periodontology*, 17(5): 306–312.

Wang, C. & Cheng, J. (2013) Cavitation Microstreaming Generated by a Bubble Pair in an Ultrasound Field. *The Journal of the Acoustical Society of America*, 134(2): 1675-1682.

Wang, J., Chen, W., Jiang, Y. & Liang, J. (2013) Imaging of Extraradicular Biofilm Using Combined Scanning Electron Microscopy and Stereomicroscopy. *Microscopy Research and Technique*, 76(9): 979–983.

White, D. J. (1997) Dental Calculus: Recent Insights into Occurrence, Formation, Prevention, Removal and Oral Health Effects of Supragingival and Subgingival Deposits. *European Journal of Oral Sciences*, 105(5): 508-522.

Whittaker, C., Ridgway, H. & Olson, B. H. (1984) Evaluation of Cleaning Strategies for Removal of Biofilms from Reverse-Osmosis Membranes. *Applied and Environmental Microbiology*, 48(2): 395-403.

Wu, T. Y., Guo, N., Teh, C. Y. & Hay, J. X. W. (2013) Theory and Fundamentals of Ultrasound, *Advances in Ultrasound Technology for Environmental Remediation* Springer, 5-12.

Wu, Y. T., Zhu, H., Willcox, M. & Stapleton, F. (2011) The Effectiveness of Various Cleaning Regimens and Current Guidelines in Contact Lens Case Biofilm Removal. *Investigative Opthalmology & Visual Science*, 52(8): 5287.

Xavier, J. B., White, D. C. & Almeida, J. S. (2003) Automated Biofilm Morphology Quantification from Confocal Laser Scanning Microscopy Imaging. *Water Science & Technology*, 47(5): 31-37.

Xi, C., Marks, D., Schlachter, S., Luo, W. & Boppart, S. A. (2006) High-Resolution Three-Dimensional Imaging of Biofilm Development Using Optical Coherence Tomography. *Journal of Biomedical Optics*, 11(3): 034001-034001-034006.

Yang, X., Beyenal, H., Harkin, G. & Lewandowski, Z. (2000) Quantifying Biofilm Structure Using Image Analysis. *Journal of Microbiological Methods*, 39(2): 109-119.

Young, F. R. (1999) *Cavitation* World Scientific.

Yu, F. (2015) *Corrosion of Titanium for Biomedical Applications* University of Birmingham, 2015.

Zanette, I., Enders, B., Dierolf, M., Thibault, P., Gradl, R., Diaz, A., Guizar-Sicairos, M., Menzel, A., Pfeiffer, F. & Zaslansky, P. (2015) Ptychographic X-Ray Nanotomography Quantifies Mineral Distributions in Human Dentine. *Scientific Reports*, 5: 9210.

Zhang, Y. & Hu, Z. (2013) Combined Treatment of Pseudomonas Aeruginosa Biofilms with Bacteriophages and Chlorine. *Biotechnology and Bioengineering*, 110(1): 286-295.

Zijnge, V., van Leeuwen, M. B. M., Degener, J. E., Abbas, F., Thurnheer, T., Gmür, R. & M. Harmsen, H. J. (2010) Oral Biofilm Architecture on Natural Teeth. *PloS One*, 5(2): e9321.

LIST OF ACHIEVEMENTS

Journal Publications

- Vyas, N. , Pecheva, E. , Dehghani, H. , Sammons, R. L. , Wang, Q. X. , Leppinen, D. M. & Walmsley, A. D. (2016a) High Speed Imaging of Cavitation around Dental Ultrasonic Scaler Tips. *PloS one*, 11(3): e0149804.

- Vyas, N. , Sammons, R. L. , Addison, O. , Dehghani, H. & Walmsley, A. D. (2016b) A Quantitative Method to Measure Biofilm Removal Efficiency From Complex Biomaterial Surfaces using SEM and Image Analysis. *Scientific Reports*, 6: 32694

- Vyas, N. , Sammons, R. L. , Pikramenou, Z. , Palin, W. M. , Dehghani, H. , Walmsley, A. D. (2017) "Penetration of Sub-Micron Particles into Dentinal Tubules using Ultrasonic Cavitation" *Journal of Dentistry*, 56, pp.112-120

Journal Publications in Preparation

- Vyas, N. , Dehghani, H. , Sammons, R. L. , Wang, Q. X. , Leppinen, D. M. and Walmsley, A. D. , "Imaging and Analysis of Individual Cavitation Microbubbles around Dental Ultrasonic Scalers" (Submitted to Ultrasonics)

Conference Presentations (Oral)

- International Association of Dental Research (IADR), Seoul, Oral, June 2016
    - Vyas N, Sammons RL, Dehghani H, Pikramenou Z, Walmsley AD. Penetration of Sub-Micron Particles into Dentinal Tubules using Ultrasonic Cavitation
- British Society of Oral and Dental Research, (BSODR), Cardiff, Oral, Sept 2015
    - Vyas N, Sammons RL, Addison O, Dehghani H, Walmsley AD. The Efficiency of Ultrasonic Cavitation in Removing Bacteria From Titanium Surfaces *in vitro*.
      In: Proceedings of The British Society for Oral and Dental Research Conference, September14th -16th 2015, Cardiff, UK
- Interdisciplinary inter-DTC conference, Oxford, Oral, June 2014
    - Vyas N, Pecheva E, Dehghani H, Grover L, Sammons RL, Walmsley AD. Visualizing Synthetic Dental Biofilm on Teeth Using Micro Computed Tomography.
- Bruker MicroCT users meeting, Ostend, Oral, May 2014
    - Vyas N, Pecheva E, Dehghani H, Grover L, Sammons RL, Walmsley AD. Visualizing Synthetic Dental Biofilm on Teeth Using Micro Computed Tomography. In: Bruker MicroCT User Meeting, May 5th-8th 2014, Ostend, Belgium

Conference Presentations (Poster)

- Midlands Academy of Medical Sciences Research Festival, Leicester, April 2016
    - Vyas N, Sammons RL, Dehghani H, Walmsley AD. Imaging Cavitation around Dental Ultrasonic Scalers and Investigating its Effectiveness in Biofilm Removal
- European Federation of Periodontology (EuroPerio), London, Poster Discussion, June 2015
    - Vyas N, Sammons RL, Pecheva E, Dehghani H, Walmsley AD. High Speed Imaging of Cavitation around Ultrasonic Scaler Tips. Poster Discussion.
      J Clin Periodontol, 42: 31–63.doi:10.1111/jcpe. 12398 (2015)
- Research Poster Conference, Birmingham. Poster, May 2015
    - Vyas N, Dehghani H, Sammons RL, Walmsley AD. Can Bubbles Clean Teeth?
- BEAR PGR Conference, Birmingham, Poster, Sept 2014
    - Vyas N, Pecheva E, Dehghani H, Grover L, Sammons RL, Walmsley AD. Visualizing synthetic dental biofilm on teeth using micro computed tomography.
- European Society of Biomaterials (ESB), Liverpool, Poster, Sept 2014

  - Pecheva E, Vyas N, Sammons RL, Walmsley AD. Imaging of Biofilm Removal on Titanium and Glass by Dental Instruments.

- Biofilms 6, Vienna, May 2014
  - Vyas N, Pecheva E, Dehghani H, Grover L, Sammons RL, Walmsley AD. Visualizing synthetic dental biofilm on teeth using micro computed tomography

Awards

- 2nd place in EPSRC Photo Competition, Weird and Wonderful category, 2015
  - SEM image of silica particles on dentine:

    http://www.birmingham.ac.uk/university/colleges/eps/news/college/2016/3/doctoral-students-awarded-top-prizes-in-epsrc-photo-competition.aspx

- Judges Choice Award, University of Birmingham Three Minute Thesis Competition, 2015
  - A competition where PhD students effectively explain their research in 3 minutes to a non-specialist audience. Video: https://goo.gl/7d9Gak

- 2nd Prize, University of Birmingham Storytelling Researcher Competition, 2015
  - A university-wide public engagement competition, with prize presentation by Professor Alice Roberts. Video: https://goo.gl/uH7cg1

- High Speed video shortlisted in the Royal Microscopical Society's Scientific Imaging Competition, 2015

  - Video was showcased throughout the 2015 Microscience Microscopy congress. Video: https://vimeo.com/131416276

- Conference Presentation Prize, ID^2 Conference, Oxford, 2014

- Poster Presentation Prize, BEAR PGR Computer Science Conference, Birmingham, 2014

PUBLICATIONS